

UNCLASSIFIED

AD NUMBER
AD487365
NEW LIMITATION CHANGE
TO Approved for public release, distribution unlimited
FROM Distribution authorized to U.S. Gov't. agencies and their contractors; Administrative/Operational Use; JUN 1965. Other requests shall be referred to US Army Missile Command, NIKE-X Project Office, Redstone Arsenal, AL 35898.
AUTHORITY
US Army Missile Command ltr dtd 22 Nov 1971

THIS PAGE IS UNCLASSIFIED

AD No. 487365
DDC FILE COPY

THE DETERMINATION OF HYPERSONIC DRAG
COEFFICIENTS FOR CONES AND SPHERES



Prepared by

- R. Grabow
- C. Pannabecker
- A. Plate
- R. Rice

RESEARCH AND ADVANCED DEVELOPMENT DIVISION
AVCO CORPORATION
Wilmington, Massachusetts

Technical Memorandum

RAD TM-65-32 ✓
Contract DA-01-021-AMC-90012(Y) ✓

Bea

26 June 1965

DDC
AUG 19 1966
dy

Prepared for

US ARMY MATERIEL COMMAND
NIKE-X PROJECT OFFICE
REDSTONE ARSENAL, ALABAMA

2

12

1200
1200

1200

2

**Best
Available
Copy**

⑥ THE DETERMINATION OF HYPERSONIC DRAG
COEFFICIENTS FOR CONES AND SPHERES

- ⑩ R. Grabow
- C. Pannabecker
- A. Plate
- R. Rice

RESEARCH AND ADVANCED DEVELOPMENT DIVISION 302 850
AVCO CORPORATION
Wilmington, Massachusetts

⑨ Technical Memo

⑮ ~~DA-01-021-AMC-90012(Y)~~

⑭ RAD-TM-65-32

⑪ 26 June 1965, ⑫ 114p.

APPROVED

Alan D. Saporith
Alan D. Saporith
Project Engineer

P. L. Sutcliffe
P. L. Sutcliffe, Director
Advanced Systems and
Penetration Aids

Prepared for

US ARMY MATERIEL COMMAND
NIKE-X PROJECT OFFICE
REDSTONE ARSENAL, ALABAMA

mt

i

ize

ABSTRACT

Analytical expressions have been developed for determining drag coefficients for cones and spheres. The ranges of variables considered are:

Cone half angle	8 to 15 degrees
Cone length	1 to 12 feet
Cone bluntness ratio	0 to 0.3
Sphere diameter	3.75 to 12 inches
Wall temperature	1000 to 3000 ^o Rankine
Free-stream Mach number	5 to 25
Altitude or approximate	0 to 200,000 feet
Free-stream Reynolds number	10 ⁴ to 10 ¹⁰
Angle of attack	0 to 20 ^o

An error analysis is presented in which the resulting drag equations are compared to wind tunnel and ballistic range data, and some limited flight test data.

Also presented are the results of an investigation aimed at determining the altitude range where a conical or spherical re-entry vehicle will undergo boundary layer transition.

This report contains essentially the same technical information as RAD TR 65-16 (SECRET) which was prepared by the same authors. However, the classified portions of this TR have been deleted in order to permit a more general distribution of useful data.

ACKNOWLEDGEMENTS

The authors wish to acknowledge the technical contributions made to this report by Messrs. R. Kohrs and M. Mitnick, and Miss D. Wells, of the Aerodynamics Section (S210).

Credit is also due to Mr. J. Gottesfeld of the Mathematics Department (E240) for programming the equations, and to Messrs. E. E. H. Schurmann, R. Tolosko, and P. F. Fote for their constructive suggestions and criticisms.

CONTENTS

I	Introduction	1
II.	Cone Pressure Drag	3
	A. Sharp Cone Forebody Pressure Drag, $\alpha = 0$	3
	B. Blunt Cone Forebody Drag, $\alpha = 0$	3
	C. Correlation of $\alpha = 0$ Solutions	4
	D. Angle of Attack	9
	E. Base Pressure Drag	19
III.	Cone Skin-Friction Drag	23
	A. Sharp Cone, Laminar Flow, $\alpha = 0$	23
	B. Sharp Cone Turbulent Flow, $\alpha = 0$	26
	C. Bluntness Effects	28
	D. Angle of Attack Effects	35
	E. Mass Addition Effects	36
IV.	Cone Induced Drag	39
	A. Induced Pressure Drag, Sharp Cone, $\alpha = 0$	40
	B. Pressure Induced Skin-Friction Drag, Sharp Cone $\alpha = 0$..	43
	C. Traverse Curvature Induced Skin-Friction Drag, Sharp Cone, $\alpha = 0$	45
	D. Bluntness Effects	46
	E. Angle of Attack Effects	52
	F. Mass Addition Effects	53
V.	Error Analysis	54
	A. Accuracy Limits	54
	B. Data Sources	54
	C. Typical Drag Coefficient Data	54
	E. Error Evaluation Based on Ground Test Data	60
	F. Applications to Flight Conditions	79
VI.	Boundary Layer Transition on Cones	82
	A. Discussion of Transition Criterion	82
	B. Employment of Criterion	84
	C. Correlation of Results	89

CONTENTS (Concl'd)

VII.	Sphere Drag and Transition	97
	A. Drag Coefficient	97
	B. Boundary Layer Transition	97
VIII.	Conclusions	103
IX.	References	105

ILLUSTRATIONS

Figure 1	Digital Curve - Fit Comparison with Basic Data; Forebody Drag Variation with Cone Angle and Bluntness Ratio - $M_\infty = 5.0$	5
2	Digital Curve - Fit Comparison with Basic Data; Forebody Drag Variation with Cone Angle and Bluntness Ratio - $M_\infty = 10.0$	6
3	Digital Curve - Fit Comparison with Basic Data; Forebody Drag Variation with Cone Angle and Bluntness Ratio - $M_\infty = 17.0$	7
4	Digital Curve - Fit Comparison with Basic Data; Forebody Drag Variation with Cone Angle and Bluntness Ratio - $M_\infty = 25.0$	8
5	Newtonian Pressure Drag Coefficient, 0° Angle of Attack	11
6	Newtonian Pressure Drag Coefficient, 10° Angle of Attack	12
7	Newtonian Pressure Drag Coefficient, 20° Angle of Attack	13
8	Newtonian Pressure Drag Ratio ($C_{D_a} / C_{D_{a=0}}$)	14
9	Pressure Coefficient Versus Meridian Angle	15
10	Pressure Coefficient Versus Meridian Angle	18
11	Accuracy of Procedure for Calculating Surface-Pressure Coefficient on Cone Correlated by Means of Hypersonic Similarity Parameter	20
12	Reference Base - Drag Coefficient $(C_{D_B})_{REF}$ for $\theta = 0$	22
13	Skin Friction Drag Coefficient, Sharp Cone, Laminar Flow	27
14	Skin Friction Drag Coefficient, Sharp Cone, Turbulent Flow	29

ILLUSTRATIONS (Cont'd)

Figure 15	Analytical Model for Blunt Body.....	31
16	Blunt Cone Skin Friction Drag Ratio, Laminar Flow	32
17	Blunt Cone Skin Friction Drag Ratio, Turbulent Flow.....	34
18	Skin - Friction Blowing Correction, LT_q , OTWR and Teflon Heat Shields	38
19	Body Geometry Notation.....	42
20	Induced Pressure Drag, 8° Sharp Cone, Laminar Flow ...	47
21	Induced Pressure Drag, 15° Sharp Cone, Laminar Flow ..	48
22	Induced Skin Friction Drag, 8° Sharp Cone, Laminar Flow	49
23	Induced Skin Friction Drag, 15° Sharp Cone, Laminar Flow	50
24	Drag Coefficient as a Function of Angle of Attack	55
25	Drag Coefficient as a Function of Angle of Attack	56
26	Drag Coefficient as a Function of Angle of Attack	57
27	Effect of Reynolds Number on Drag Coefficient	58
28	Drag Coefficient Ratio as a Function of Mach Number.....	59
29	Drag Coefficient Ratio as a Function of Cone Angle.....	61
30	Altitude as a Function of Reynolds Number for Various Mach Numbers -- Body Length 1 Foot	62
31	Drag Coefficient Ratio as a Function of Equivalent Minimum Altitude	63
32	Total Drag Coefficient	80
33	Transition Reynolds Number Versus Local Mach Number	83

ILLUSTRATIONS (Concl'd)

Figure 34	Reynolds Number Variation, 8° Blunt Cone.....	86
35	Reynolds Number Variation, 10° Blunt Cone.....	87
36	Reynolds Number Variation, 15° Blunt Cone.....	88
37	Altitude of Initial Transition for Varying Cone Angles....	90
38	Altitude of Initial Transition for Varying Cone Angles....	91
39	Altitude of Initial Transition for Varying Cone Angles....	92
40	Altitude of Initial Transition for Varying Cone Angles....	93
41	Velocity Effect on Transition Altitude.....	95
42	Sphere Drag Coefficient as a Function of Mach Number ..	98
43	Sphere Drag Coefficient as a Function of Reynolds Number	99
44	Altitude of Initial Transition for Spheres	101

TABLES

Table I	Coefficients for $(C_{D\alpha} / C_{D_{\alpha=0}})$ Curve - Fit Solution	15
II	Tabulated Data Drag and Ratios	64

NOMENCLATURE

C	Form at Chapman-Rubesin viscosity coefficient (also pressure coefficient)
C_p	Specific heat of constant pressure
C_{f_a}	Local skin-friction coefficient based on free stream conditions
C_{D_f}	Skin-friction drag coefficient (no interaction)
C_{D_B}	Base pressure drag coefficient
C_{D_p}	Forebody, pressure drag coefficient (no interaction)
C_{D_i}	Induced drag coefficient
d_∞	Wall temperature parameter
$F_1(K)$	Induced pressure gradient parameter
h	Enthalpy
H_T	Total heat absorbed by body
K, K', K''	Induced drag functions
L	Slant length of sharp cone
\dot{m}	Mass injection rate
M	Mach number
Pr	Prandtl number
p	Pressure
q^*	Effective heat of ablation
q	Dynamic pressure
r	Body radius of curvature (also recovery factor)
R_B	Base radius
R_N	Nose radius

$R_{\infty x}$	Reynolds number based on free stream conditions
Re_x	Reynolds number based on local conditions at boundary layer edge
T	Temperature
u	Velocity in streamwise direction
v	Velocity normal to the wall
x	Coordinate along sharp cone surface
δ^*	Boundary layer displacement thickness
\bar{X}	Viscous interaction parameter
Δ	Denotes induced values
α	Angle of attack
η	Transpiration factor
θ	Cone angle (semi-vertex angle)
θ_s	Shock angle
γ	Ratio of specific heats
ρ	Density
μ	Viscosity coefficient
ϕ	Meridian Angle
<u>Subscripts</u>	
c	Conical flow
e	Edge of boundary layer conditions
w	wall conditions
s	stagnation conditions
p	pressure induced
$t.c.$	transverse-curvature induced

Subscripts (Cont'd)

- free stream conditions
- o no blowing

Superscripts

- Reference enthalpy conditions
- Averaged values for angle of attack properties

I. INTRODUCTION

This investigation is part of the Nike-X discrimination studies which are aimed at developing a quantitative evaluation of the observable characteristics of a re-entry vehicle and/or decoy.

The drag coefficient of a vehicle is a major discriminant because it is the most significant parameter affecting the vehicle's velocity-altitude signature.

The primary purpose of this investigation is to develop analytical expressions for evaluating the total drag coefficient of spheres and cones. The accuracy of these equations is to be determined by comparing the results with wind-tunnel, ballistic range, and flight test data. Since the drag equations presented in this report are to be used in discrimination studies, it is necessary that the independent variables consist only of free-stream properties, body geometry, and surface material. Consequently, all the viscous calculations which normally involve flow properties at the edge of the boundary layer have to be modified in order to transform to free-stream conditions. This requirement generally leads to the employment of correlated conical shock relations, perfect gas laws, and curve-fitting techniques. For the inviscid calculations it was also necessary to develop curve-fits which represent the results of rigorous solutions in terms of the desired parameters.

In the employment of these simplifying techniques, it was necessary to maintain an accuracy requirement that is within the range specified for this investigation; i. e., 10% accuracy from sea level to 100,000 ft, and then a linear variation up to 30% accuracy at 200,000 ft. This accuracy requirement is based on the following ranges of variables:

Cone half angle	8 to 15 degrees
Cone length	1 to 12 feet
Cone bluntness ratio	0 to 0.3
Sphere diameter	3.75 to 12 inches
Wall temperature	1000 to 3000 ^o Rankine
Free-stream Mach number	5 to 25
Altitude or approximate	0 to 200,000 feet
Free-stream Reynolds number	10 ⁴ to 10 ¹⁰
Angle of attack	0 to 20 degrees at 200,000 feet 0 to 0 below 150,000 feet

The accuracy requirement is also based on a vehicle that is not ablating or experiencing mass injection into the boundary layer. Since most re-entry vehicles will have some type of thermal protection which does ablate, the accuracy requirement will not be met if mass addition effects are not included. Although the contractual requirements for this investigation did not include mass addition (blowing), an approximate method for determining the reduction in skin friction drag due to blowing is provided. This approximate method should result in a total drag coefficient that is within the specified accuracy range.

Also included is a discussion of more rigorous methods of analysis which may be employed to determine the effects of blowing on skin-friction drag and induced drag.

For the case of pure spheres, the total drag coefficient is obtained solely from an empirical correlation of experimental data. For the case of cones, each individual drag contribution is separately determined by either pure theoretical techniques or semi-empirical methods. The individual components are: (1) forebody pressure drag (CD_p) - the drag due to direct pressure forces, (2) base pressure drag (CD_B) - the drag due to a pressure in the base region which is less than ambient, (3) skin-friction drag (CD_f) - the drag due to viscous shear forces, laminar and turbulent, and (4) induced drag (CD_i) - the increased pressure and skin-friction drag due to a thick boundary layer (considered for laminar flow only) which interacts with the inviscid flow.

The transition from laminar to turbulent flow has been investigated, and predictions are made for determining the altitude range where this phenomena occurs. For the case of cones, the results of various flight tests have been employed to produce a transition criterion.

II. CONE PRESSURE DRAG

A. Sharp Cone Forebody Pressure Drag, $\alpha = 0$

The forebody pressure drag coefficient is defined by the relation,

$$C_{D_p} = \frac{2\pi}{q_{\infty} A_B} \int_0^{R_B} (p_c - p_{\infty}) r dr$$

For a sharp cone at $\alpha = 0$, the pressure (p_c) is constant over the entire body, and the forebody drag is then only a function of the pressure ratio (p_c/p_{∞}) across the conical shock. Solutions for this pressure ratio as a function of Mach number and cone angle have been tabulated by Kopal (reference 1) for a ratio of specific heats, $\gamma = 1.405$. These results have been employed directly in the drag equation in order to obtain the forebody drag on a sharp cone.

The results have also been compared to exact conical flow solutions employed at Avco RAD for the case of a real gas (Program 1427) (reference 2), and there was excellent agreement.

B. Blunt Cone Forebody Drag, $\alpha = 0$

For a blunt cone at $\alpha = 0$, the pressure (p_c) in the forebody drag equation is not constant with respect to axial distance (x). However, at a given value of x , the pressure is constant in the transverse direction when $\alpha = 0$. Therefore, to solve the forebody drag equation, the axial pressure distribution $p_c = p_c(x)$ must first be determined, and then the equation can be integrated directly.

The pressure distribution on a blunt body is most accurately determined by the method of characteristics, which is explained in reference 3 and numerous other texts. The numerical solution of this method may be obtained from digital computer programs developed by Avco RAD. To provide the initial data for the method of characteristics (employed in the supersonic region), a solution for the transonic flow region around the blunt nose is first employed (Program 1447) (reference 4). The initial data is then used in the axi-symmetric flow method of characteristics solution (Program 596) (reference 3).

For this present investigation of blunt cones, method of characteristics solutions comparable to those obtained from the digital computer programs mentioned above were employed.

These solutions were originally documented by Chuskin and Schulishnina in the form of tables; their results were translated, edited, and re-documented at Avco RAD (reference 5). These solutions were obtained by the method of characteristics, employing the blunt body solution of Belotserkovskii (reference 6) for the initial data.

The reasons for selecting to employ these solutions in this investigation are: 1) the results are essentially the same as obtained by the Avco RAD methods, 2) the pressure distributions have already been integrated to yield the forebody drag coefficient, and 3) it would take considerable computer time to re-run all the solutions investigated in reference 6.

C. Correlation of $\alpha = 0$ Solutions

The results of the sharp and blunt body solutions at $\alpha = 0$ have been correlated as a function of M_∞ , θ , and R_N/R_B , (reference 7). The analysis consisted of curve-fitting the solutions in the form,

$$C_{D_p} = C \sin^N \theta + \frac{K}{r^A} \left(\frac{R_N}{R_B} \right)^B$$

which is similar to the form of the Newtonian drag equation. The quantities C, N, K, A, and B represent the variations from Newtonian theory due to Mach number effects. Employing polynomial curve-fitting techniques, we obtain,

$$C = 1.944 + 1.872 M_\infty^{-1} - 17.00 M_\infty^{-2} + 38.194 M_\infty^{-3}$$

$$N = 1.931 + 0.8635 M_\infty^{-1} - 8.063 M_\infty^{-2} + 12.205 M_\infty^{-3}$$

$$K = 11.433 + 34.96 M_\infty^{-1} - 921.5 M_\infty^{-2} + 2607.3 M_\infty^{-3}$$

$$A = 0.5359 + 0.09964 M_\infty^{-1} + 10.769 M_\infty^{-2} - 104.21 M_\infty^{-3} + 209.43 M_\infty^{-4}$$

$$B = 3.296 + 2.997 M_\infty^{-1} - 74.378 M_\infty^{-2} + 154.67 M_\infty^{-3}$$

The results of these curve-fits are compared to the basic method of characteristics solutions in figures 1 through 4 for Mach numbers of 5, 10, 17, and 25, and varying bluntness ratios. The agreement is good, therefore satisfying the first requirement of developing an analytical expression for forebody drag at zero angle of attack. It should be emphasized, however, that the curve-fits are valid only within the specified limits of M , θ , and R_N/R_B .

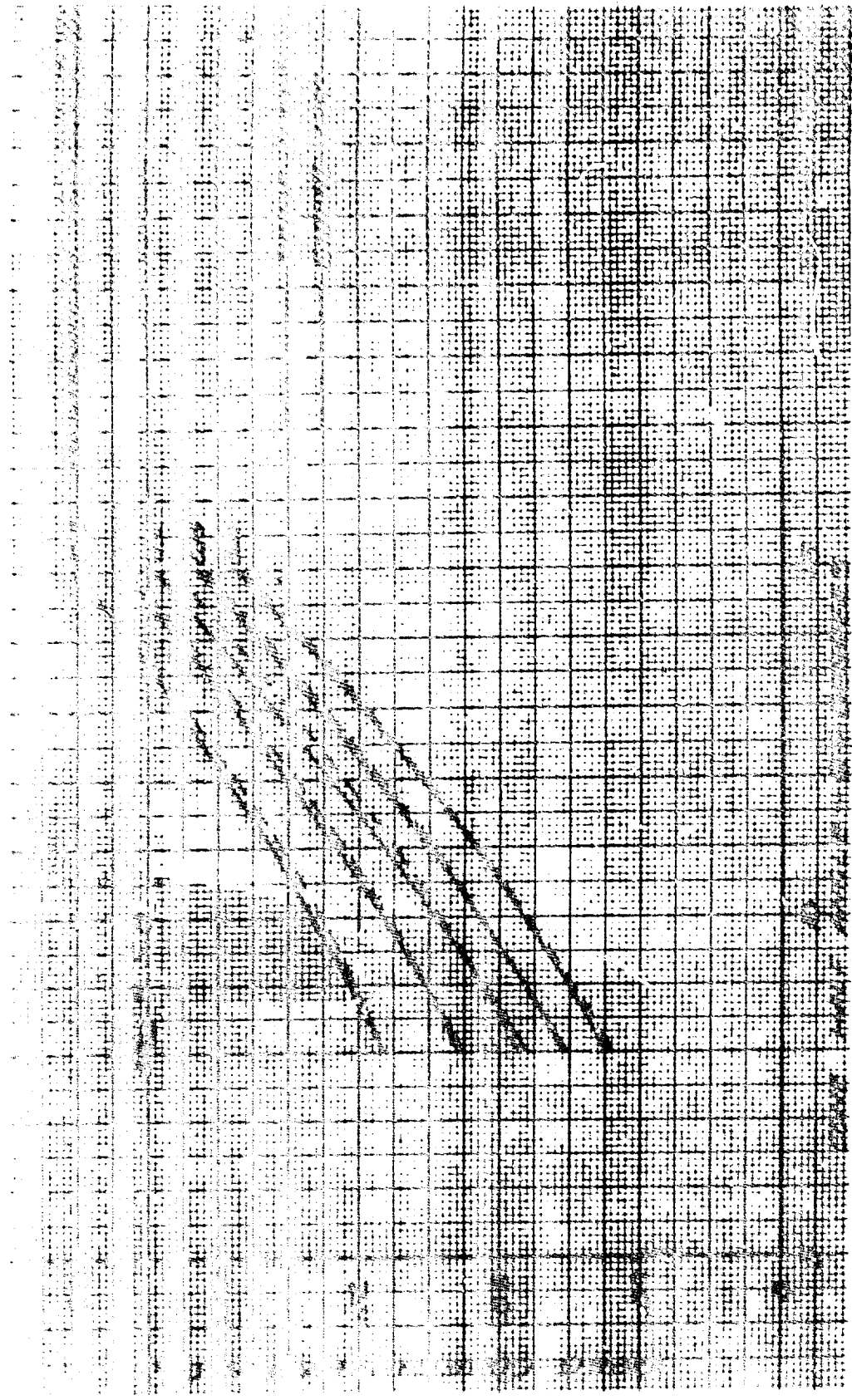


Figure 1 DIGITAL CURVE - FIT COMPARISON WITH BASIC DATA; FOREBODY DRAG
VARIATION WITH CONE ANGLE AND BLUNTNES RATIO - $M_{\infty} = 5.0$

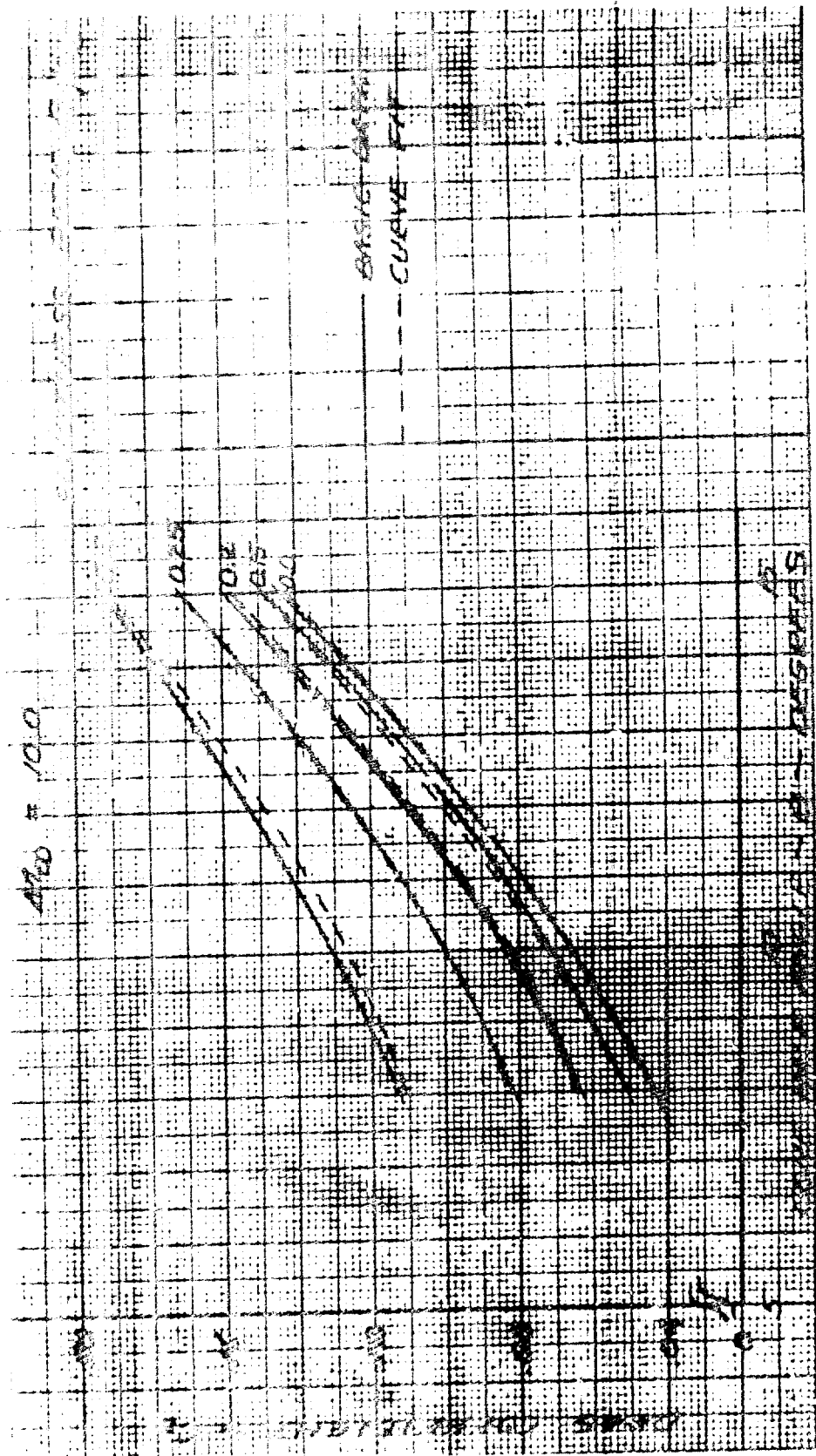


Figure 2 DIGITAL CURVE - FIT COMPARISON WITH BASIC DATA; FOREBODY DRAG VARIATION WITH CONE ANGLE AND BLUNTNESS RATIO - M = 10.0

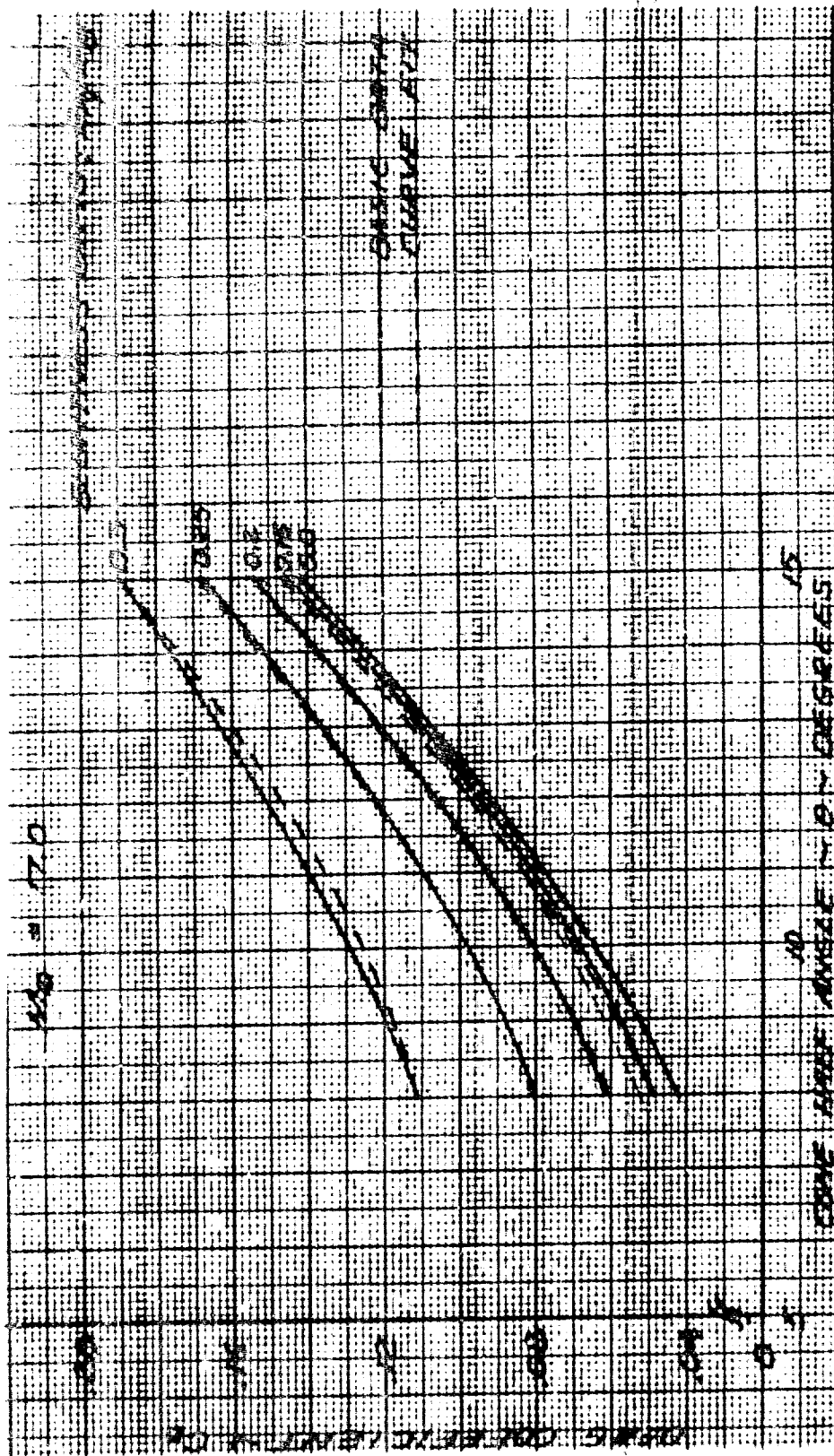


Figure 3 DIGITAL CURVE - FIT COMPARISON WITH BASIC DATA; FOREBODY DRAG VARIATION WITH CONE ANGLE AND BLUNTNES RATIO - $M_{\infty} = 17.0$

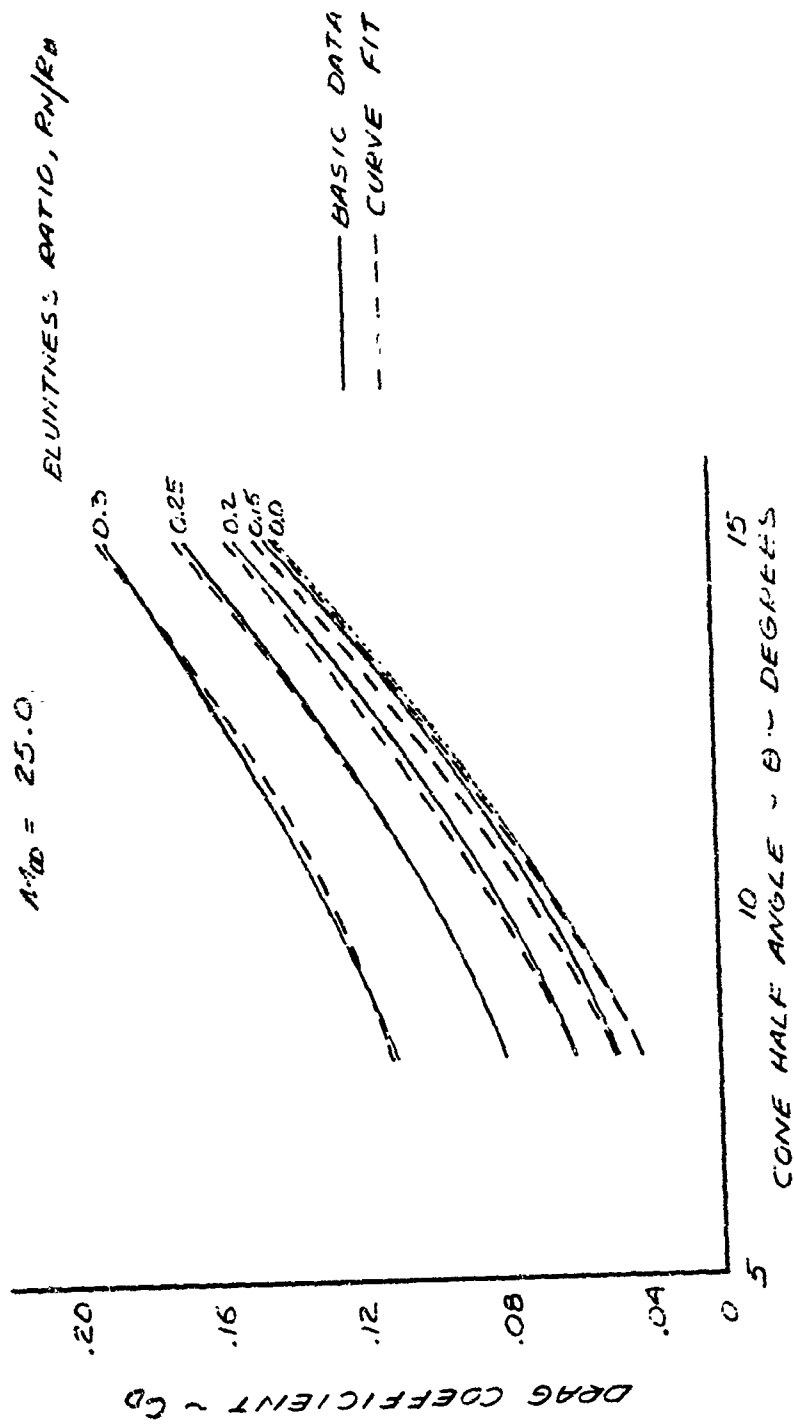


Figure 4 DIGITAL CURVE - FIT COMPARISON WITH BASIC DATA; FOREBODY DRAG VARIATION WITH CONE ANGLE AND BLUNTNESS RATIO - $M_{\infty} = 25.0$

D. Angle of Attack Effects

In order to account for angle of attack effects on forebody pressure drag, the following methods of analyses may be employed:

1) Sharp Cone

The circumferential pressure distribution around the yawed body (in a plane perpendicular to the axis of symmetry) may be obtained from a perturbation solution of the conical flow equations. This solution is presently programmed for machine computation (Program 1431) (reference 8). The resulting pressure distributions are then integrated over the body to yield the forebody pressure drag coefficient.

2) Blunt Cone

The circumferential pressure distribution for this configuration may be obtained from a recently developed method of integral relations (reference 9). Although this solution has been programmed, it has not been completely checked out; therefore, this method of analysis has not been employed in this investigation.

3) Newtonian Theory

This widely accepted theory may be applied to both sharp and blunt cones at angle of attack. The theory may be used directly to calculate forebody pressure drag, or it may be used to generate angle of attack scaling factors which are then applied to the $\alpha = 0$ solutions presented in the previous paragraphs.

A limited comparison has been made between methods 1 and 3, and the results indicate excellent agreement in the hypersonic range when Newtonian theory is used to generate scaling factors; i. e.,

$$(C_{D_p})_{\alpha} = (C_{D_p})_{\alpha=0} \left(\frac{C_{D_{\alpha}}}{C_{D_{\alpha=0}}} \right)_{\text{Newt}}$$

where $(C_{D_p})_{\alpha=0}$ is obtained from the correlations presented in paragraph C of this section.

The scaling factor $(C_{D_{\alpha}}/C_{D_{\alpha=0}})_{\text{Newt}}$ is obtained from Newtonian theory employing digital computer program 814 (reference 10). In this solution, the Newtonian pressure distributions at angle of attack are integrated

circumferentially and longitudinally along an axi-symmetric body of revolution. The program computes the bounds of the aerodynamic shadow region, and calculates aerodynamic coefficients for angles of attack from 0 to π radians at any input interval desired. Some results of this program are plotted in figures 5 through 7 as the drag coefficient C_D versus the cone angle θ for bluntness ratios R_N/R_B , of 0, 0.1, 0.2, and 0.3 for angles of attack of 0° , 10° , and 20° . Figure 8 presents the desired Newtonian drag ratio, $(C_{D\alpha}/C_{D\alpha=0})_{Newt}$, as a function of cone angle, bluntness ratio, and angle of attack.

In order to develop an analytical expression for this ratio, the results presented in figure 8 have been curve fit, employing a recently developed digital computer program. Avco RAD program 1413 (reference 11) enables a dependent variable to be fitted as a function of polynomial powers of up to three independent variables. The program uses the least-squares approach to data fitting where the independent variable are all presented as polynomials of a specified order.

The resulting curve-fit is of the form:

$$\begin{aligned}
 (C_D/C_{D_{\alpha=0}})_{Newt} = & \{ [A_1 + A_2 \alpha + A_3 \alpha^2] + [A_4 \alpha + A_5 \alpha + A_6 \alpha^2] \theta \\
 & + [A_7 + A_8 \alpha + A_9 \alpha^2] \theta^2 \} \\
 & + \{ [A_{10} + A_{11} \alpha + A_{12} \alpha^2] + [A_{13} + A_{14} \alpha + A_{15} \alpha^2] \theta \\
 & + [A_{16} + A_{17} \alpha + A_{18} \alpha^2] \theta^2 \} \frac{R_N}{R_B} \\
 & + \{ [A_{19} + A_{20} \alpha + A_{21} \alpha^2] + [A_{22} + A_{23} \alpha + A_{29} \alpha^2] \theta \\
 & + [A_{25} + A_{26} \alpha + A_{27} \alpha^2] \theta^2 \} \left(\frac{R_N}{R_B} \right)^2
 \end{aligned}$$

where the numerical values of the coefficients are given in table I. The accuracy of the curve-fit is within 5 percent of the actual Newtonian values.

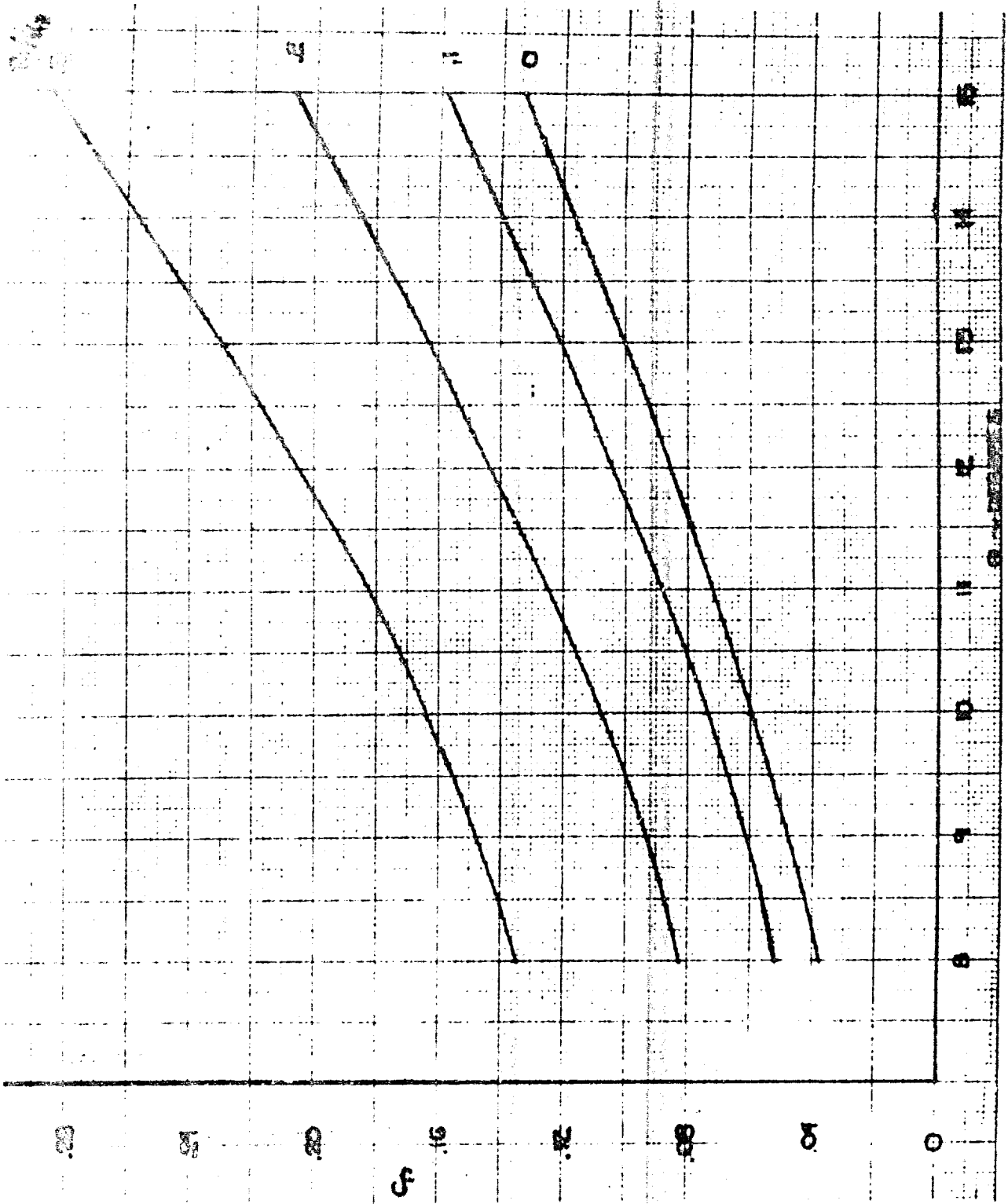


Figure 5 NEWTONIAN PRESSURE DRAG COEFFICIENT, 0° ANGLE OF ATTACK

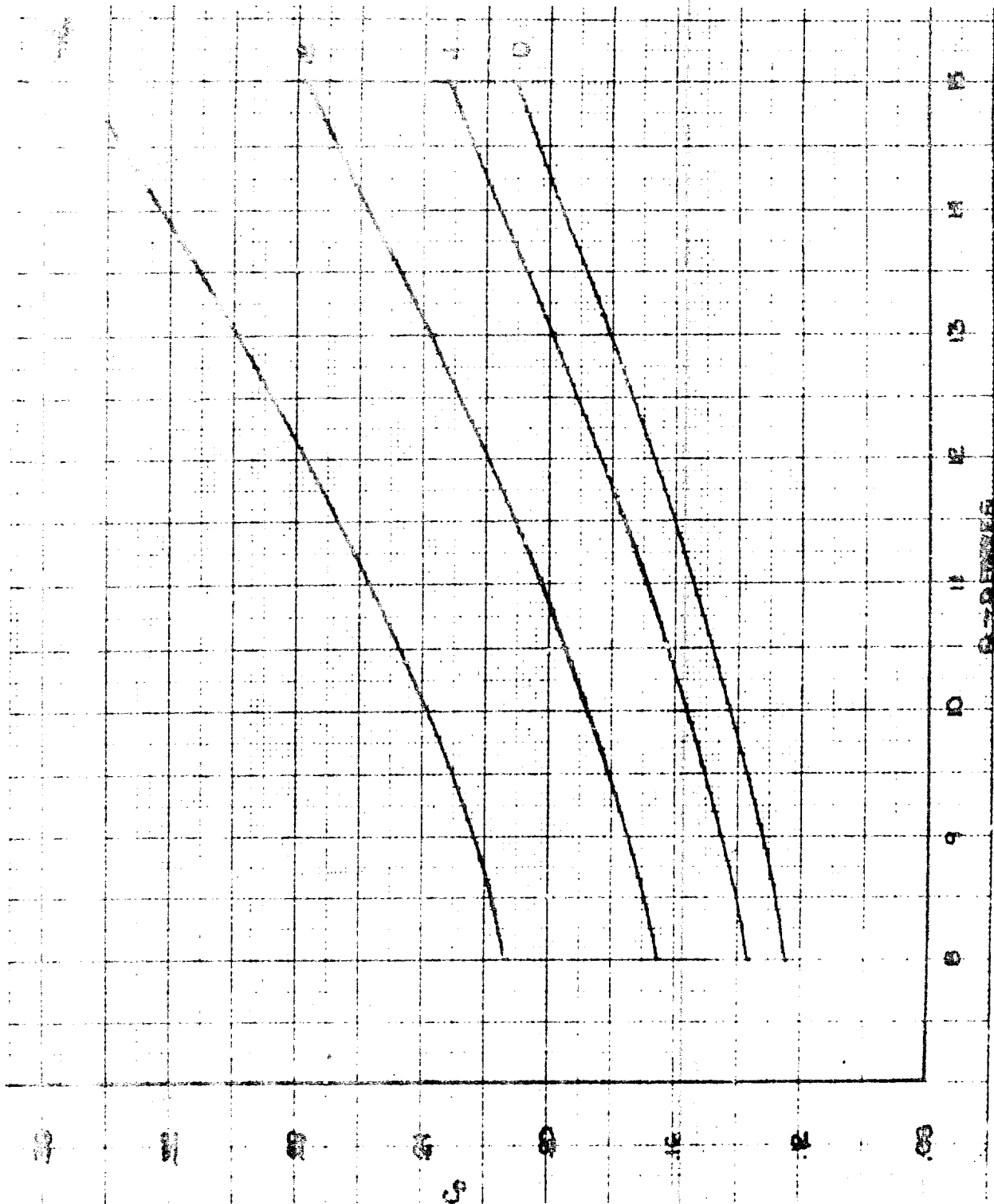


Figure 6 NEWTONIAN PRESSURE DRAG COEFFICIENT 10° ANGLE OF ATTACK

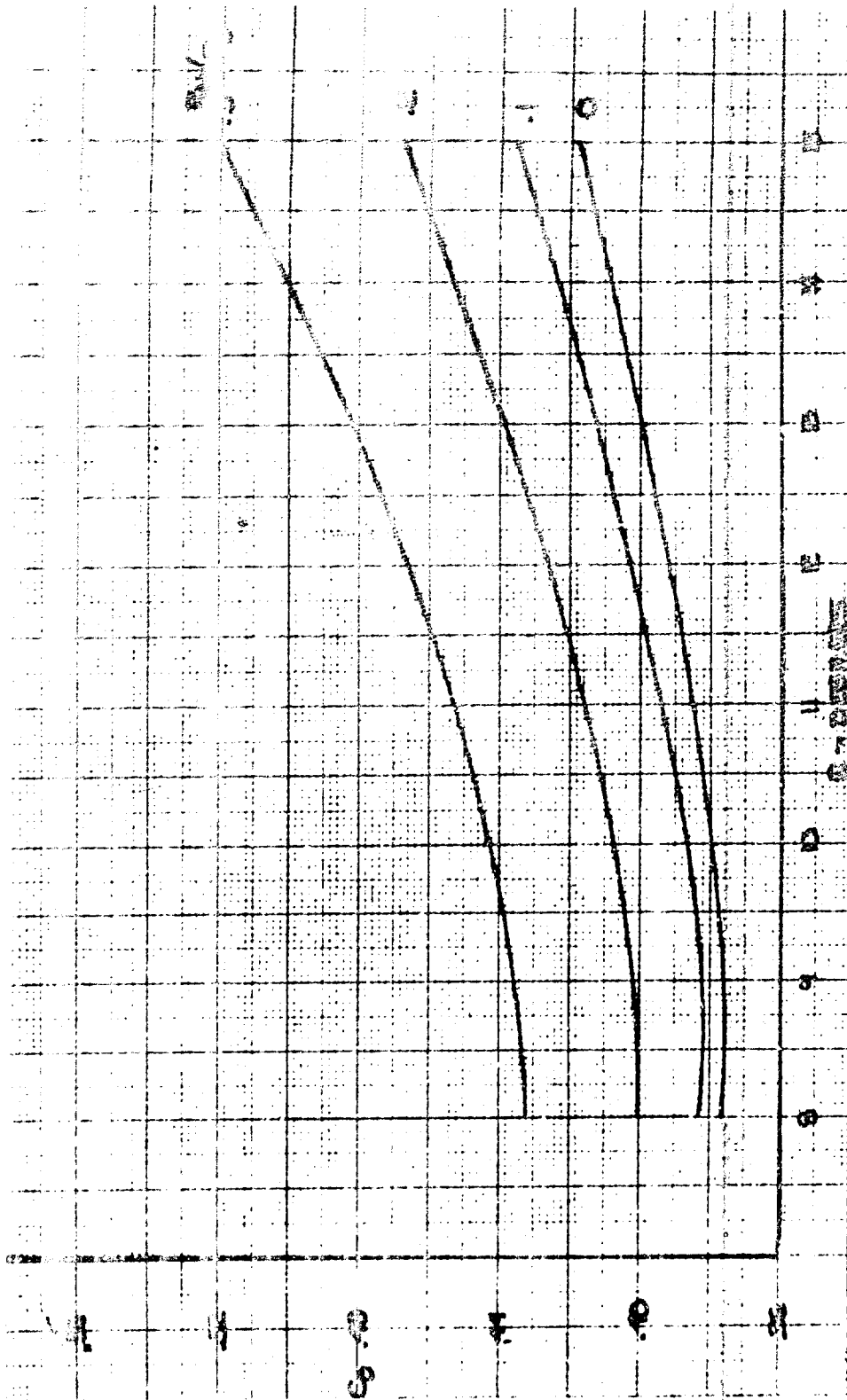


Figure 7 NEWTONIAN PRESSURE DRAG COEFFICIENT 20° ANGLE OF ATTACK

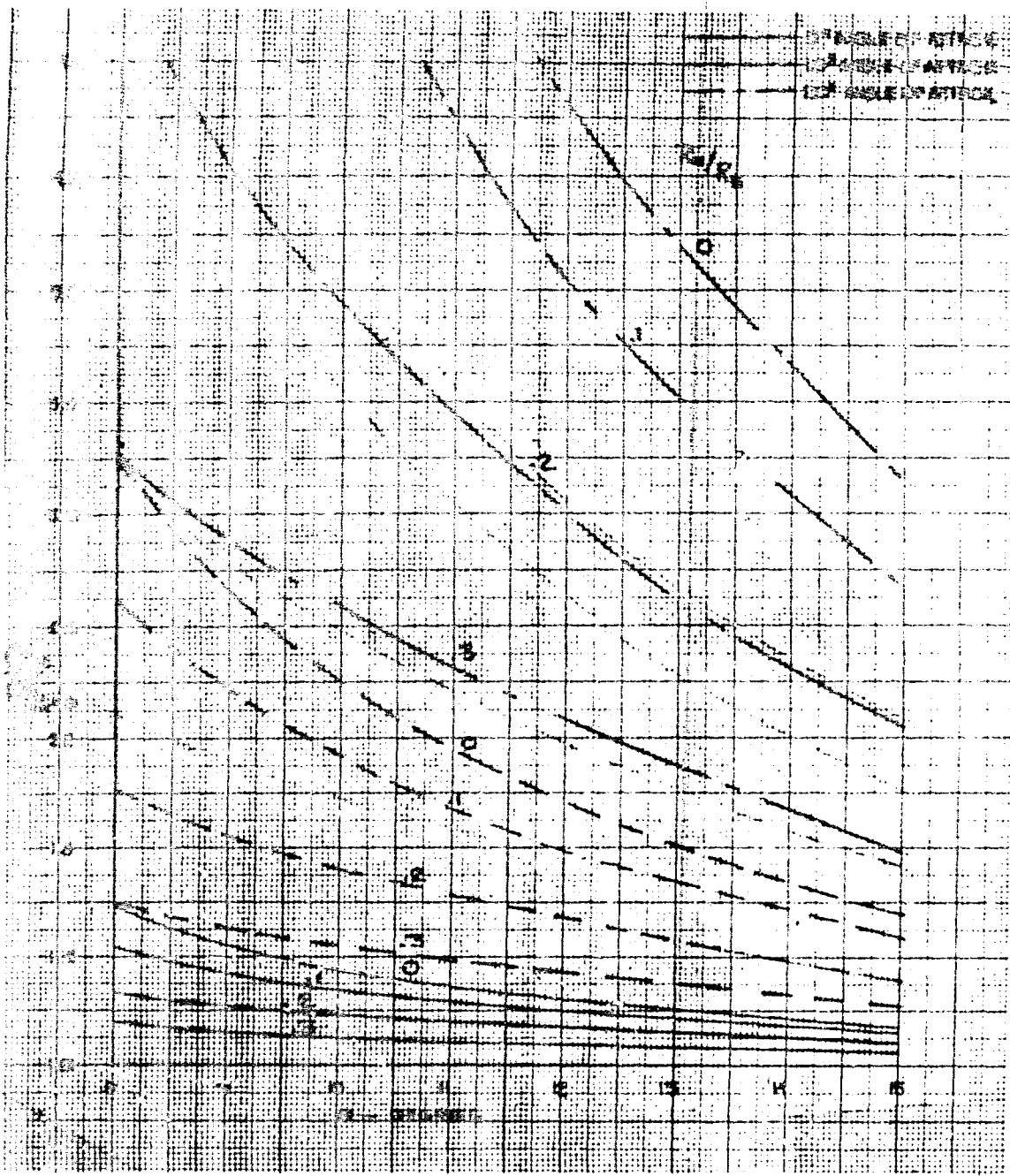


Figure 8 NEWTONIAN PRESSURE DRAG RATIO ($C_{D_n} / C_{D_{n=0}}$)

TABLE I

COEFFICIENTS FOR $(C_{D_a}/C_{D_{a=0}})_{Newt}$ CURVE-FIT SOLUTION

A₁ = 4.54681695 E-01
A₂ = 1.08259007 E-01
A₃ = 7.52646267 E-02
A₄ = 9.92751992 E-02

A₅ = -1.93200192 E-02
A₆ = -9.13259697 E-03
A₇ = -4.32304686 E-03
A₈ = 8.08808160 E-04

A₉ = 2.95970723 E-04
A₁₀ = 1.63346966 E+01
A₁₁ = -4.50010377 E+00
A₁₂ = -1.07061625 E-01

A₁₃ = -2.97740823 E+00
A₁₄ = 8.21443164 E-01
A₁₅ = 5.86190152 E-03
A₁₆ = 1.28462178 E-01

A₁₇ = -3.55578628 E-02
A₁₈ = 7.00471497 E-05
A₁₉ = -5.35168993 E+01
A₂₀ = 1.51758946 E+01

A₂₁ = -4.10820156 E-01
A₂₂ = 9.74715936 E+00
A₂₃ = -2.77304727 E+00
A₂₄ = 8.15759611 E-02

A₂₅ = -4.20040721 E-01
A₂₆ = 1.09716924 E-01
A₂₇ = -3.72121710 E-03

In order to confirm the validity of Newtonian scaling laws at angle of attack a typical comparison with experimental data is presented in figures 9 and 10. The comparison consists of plots of the pressure coefficient (C_p) versus meridian angle (ϕ) for sharp 10° and blunt 15° cones at zero and 10° angle of attack. The Newtonian pressure coefficient, C_p , was obtained from the relation,

$$C_p = \frac{P - P_\infty}{\frac{1}{2} \rho_\infty u_\infty^2} = 2(\sin \theta \cos \alpha + \sin \alpha \cos \theta \cos \phi)^2$$

for the sharp cone case, the result of integrating these pressure coefficients yielded a ratio $(C_{D_\alpha}/C_{D_{\alpha=0}})_{Newt}$ that was only 2 percent higher than the corresponding ratio for the experimental data. For the blunt cone case (figure 10), the Newtonian drag ratio is 3 percent higher than the experimental drag ratio.

The data of figures 9 and 10 in conjunction with other similar comparisons (reference 12, 13) have been correlated to determine the error incurred in employing Newtonian theory for pressure distributions. The results of this correlation indicate that at relatively low Mach numbers and small angles of attack, Newtonian flow under-estimates the pressure distribution on the windward side of the body. As both the Mach number and angle of attack are increased, the comparisons show improvement. The Newtonian assumption of a zero pressure coefficient for the leeward side in the shadow region tends to result in overestimation of the leeward pressures by as much as a factor of two in some cases. However, the leeward pressures at angle of attack are of course very much smaller than the windward pressures, and accordingly, the effect on vehicle drag of relatively large errors in leeward pressure will not be substantial.

In order to present some quantitative comparisons, the percentage error in C_p defined by

$$\% \text{ error in } C_p = \left(\frac{C_{p \text{ Newtonian}} - C_{p \text{ test}}}{C_{p \text{ test}}} \right) \times 100 \quad (6)$$

has been computed for the windward meridian. Figure 11 shows a plot of this percentage error as a function of the similarity parameter K defined as

$$K = 2 M_\infty \tan(\theta + \alpha) \quad (7)$$

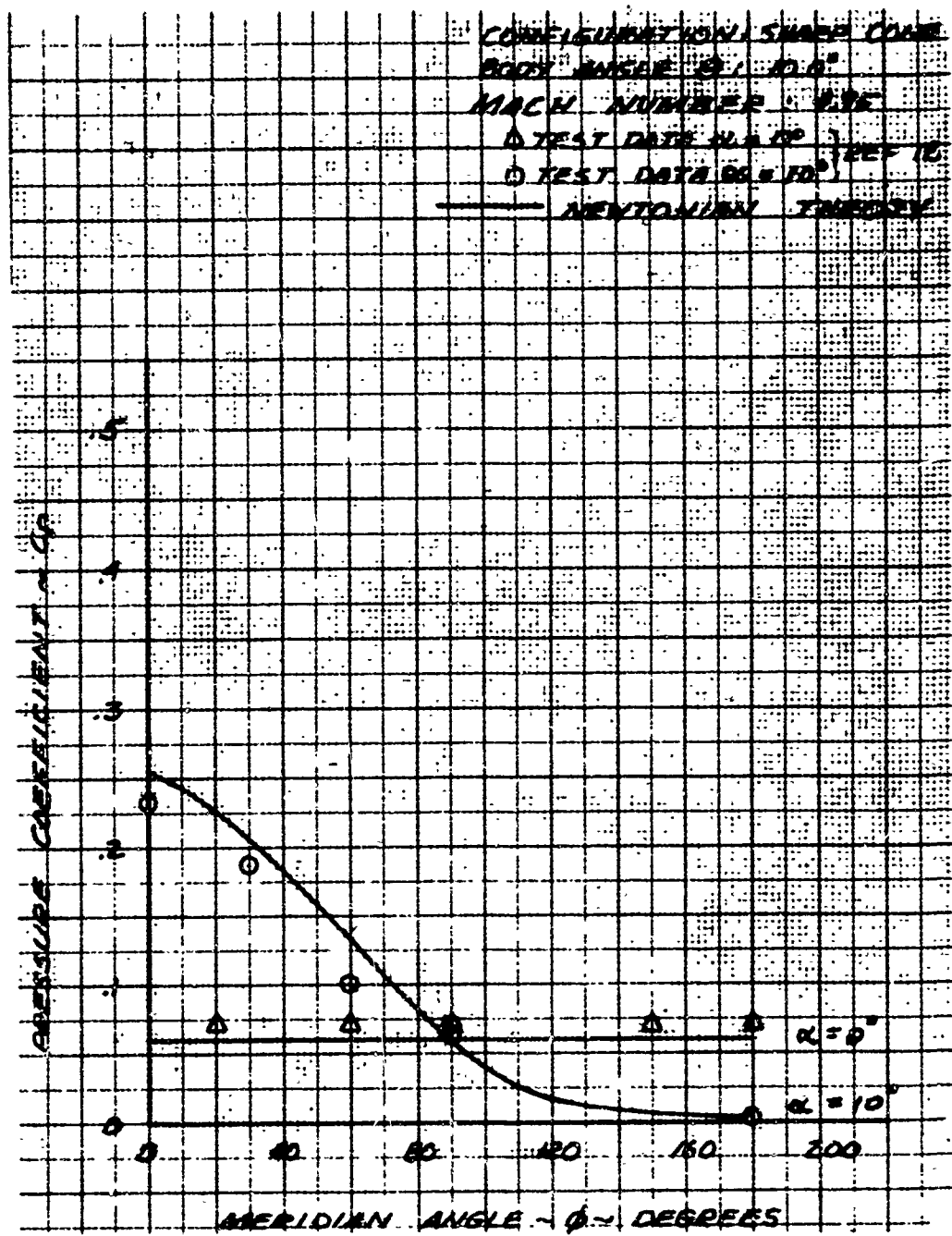


Figure 9 PRESSURE COEFFICIENT VERSUS MERIDIAN ANGLE

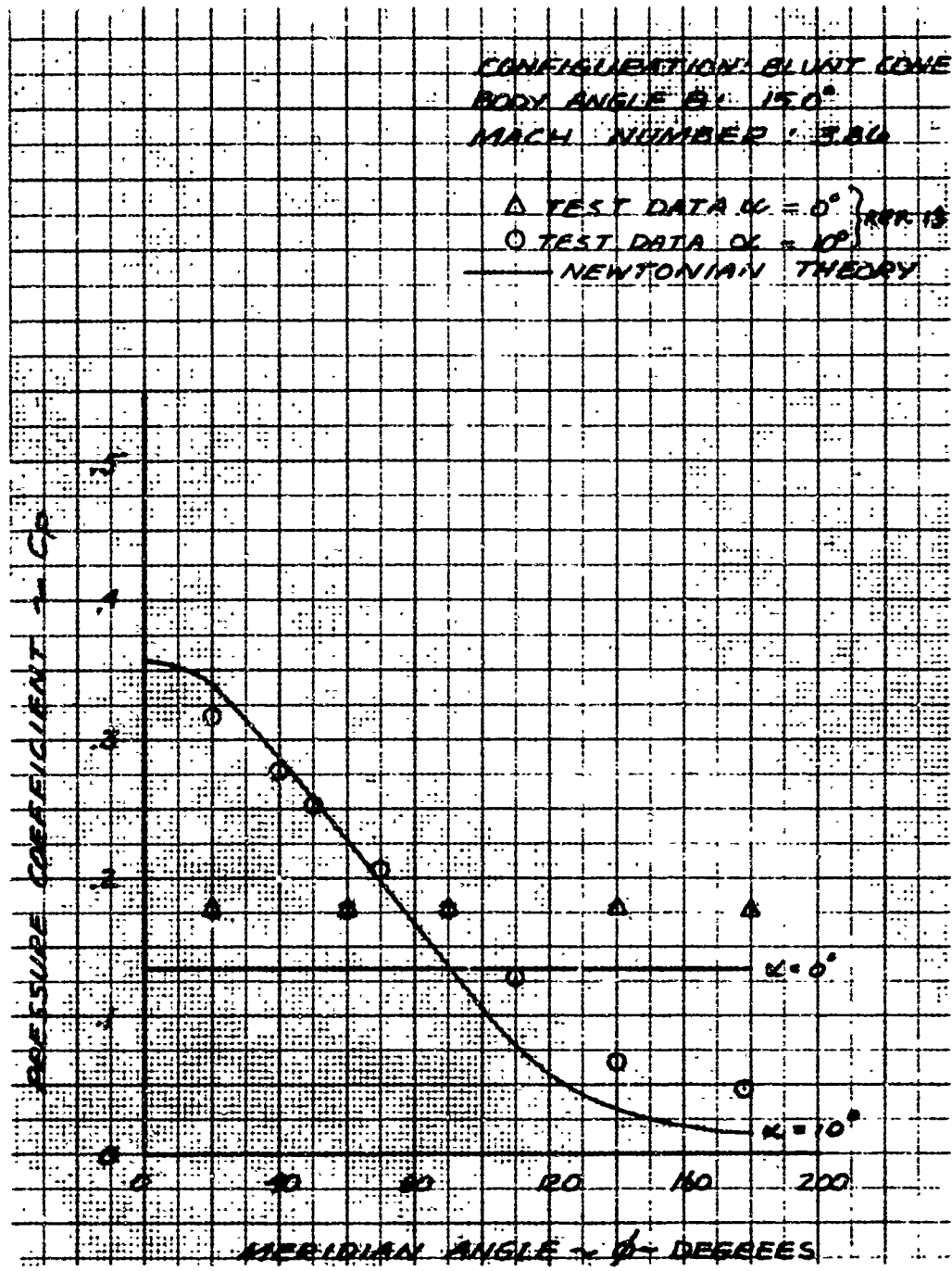


Figure 10 PRESSURE COEFFICIENT VERSUS MERIDIAN ANGLE

Also included in figure 11 are comparisons of Newtonian theory with analytical values computed from exact conical flow solutions, at $\alpha = 0$ as given in reference 14. The percentage error for this latter information is defined as:

$$\% \text{ error in } C_p = \left(\frac{C_{p\text{Newtonian}} - C_{p\text{analytical}}}{C_{p\text{analytical}}} \right) \times 100 \quad (8)$$

Figure 11 shows that Newtonian theory underpredicts windward pressures at the lower K values. The underprediction is about 10 percent for a K value of about 3.0. For a 10 degree cone, at a 5 degree angle of attack, for example, a K value of 3.0 would occur at a Mach number of 5.6. At K values of the order of 10.0, the Newtonian theory overpredicts the pressure coefficient by about 3 percent. For the same 10 degree cone at 5 degree angle of attack, a K value of 10.0 would be attained at a Mach number of 18.7. Thus it can be deduced that for moderate cone angles and even relatively small angles of attack, the Newtonian theory tends to be a reasonable approximation over the hypersonic flow regime.

For an 8 degree cone at zero angle of attack at Mach 5.0, which represents the lower limit of the K parameter in the current study, and therefore the maximum error in Newtonian flow, the percentage error is seen to be about 24 percent. However, this is the error incurred when Newtonian theory is employed directly, in the absolute sense. In this investigation, Newtonian theory is only used to scale the zero angle of attack solutions which are obtained by more accurate methods. Consequently, for an 8 degree cone at $M_\infty = 5$, the error will be much less than indicated by figure 11. It is also shown in this graph that as any of the parameters, Mach number, cone angle, or angle of attack, one increased, the percentage error incurred from Newtonian theory decreases.

E. Base Pressure Drag

The basic data used to calculate base drag coefficients were obtained from flight test pressure measurements reported in reference 15. This flight test data has been verified by ground test data reported in references 16 and 17. Investigation of the data shows that the major parameters influencing base pressure drag are Mach number and cone angle. The effects of Reynolds number, wall temperature, bluntness and ablation rates did not significantly effect the average pressure level in the separated flow region of the base.

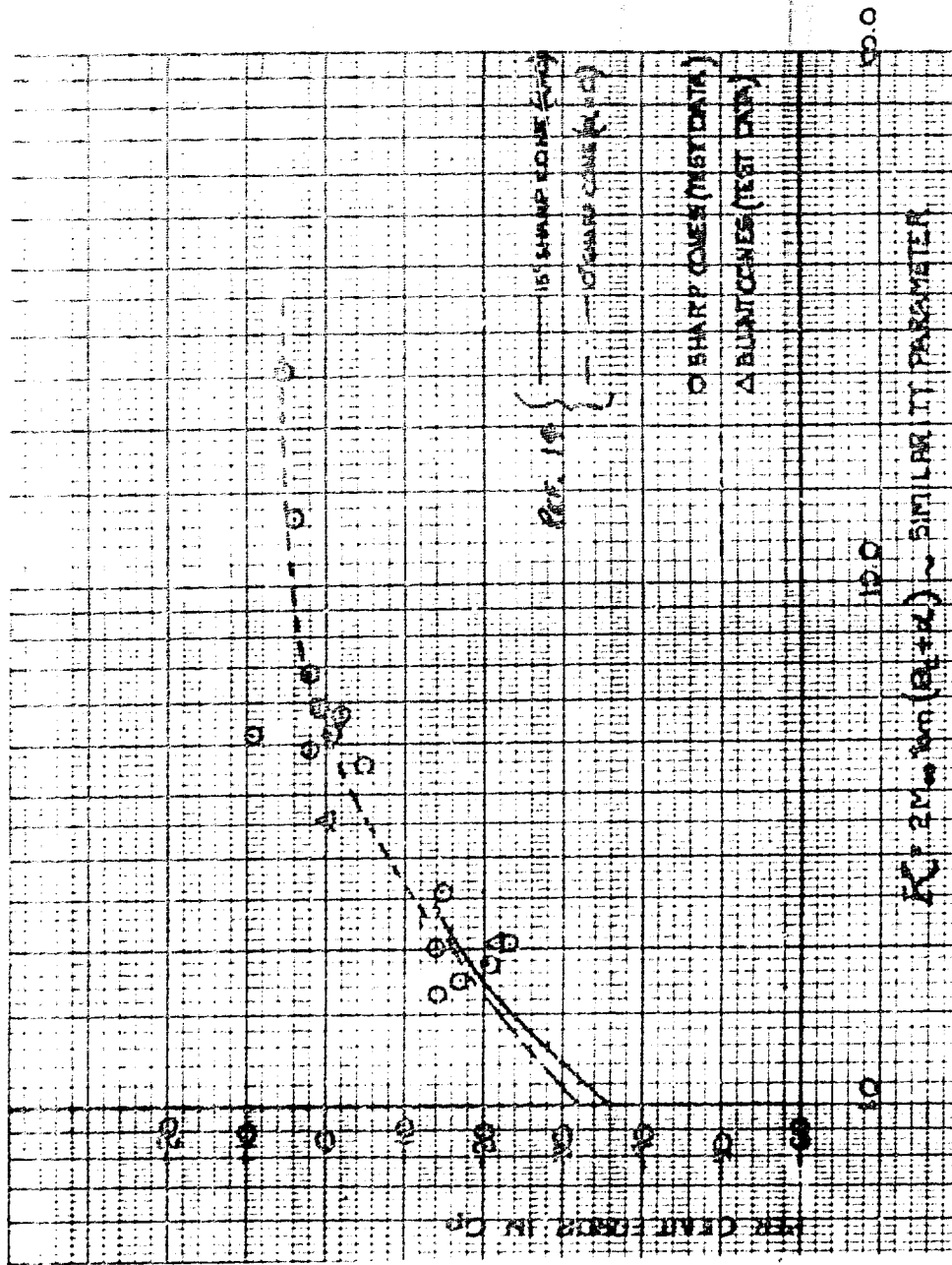


Figure 11 ACCURACY OF PROCEDURE FOR CALCULATING SURFACE-PRESSURE COEFFICIENT ON CONE CORRELATED BY MEANS OF HYPERSONIC SIMILARITY PARAMETER

To correlate the effects of Mach number, the flight test results obtained from reference 15 have been used to define a reference base drag coefficient $(C_{DB})_{ref}$, for a cone angle, $\theta = 0$ degree. A curve-fit of the variation of $(C_{DB})_{ref}$ with Mach number has been reported in reference 7 to be

$$(C_{DB})_{ref} = e^{(-1.706 - 0.33M_\infty + 0.00566 M_\infty^2)}$$

This variation is presented in figure 17, together with the limiting vacuum condition.

To correlate the effects of cone angle, the results of reference 12 show that $C_{DB} \sim (1 + \sin \theta)$.

The final equation for the base drag coefficient is then,

$$C_{DB} = (1 + \sin \theta) (C_{DB})_{ref} = (1 + \sin \theta) e^{(-1.706 - 0.33 M_\infty + 0.00566 M_\infty^2)}$$

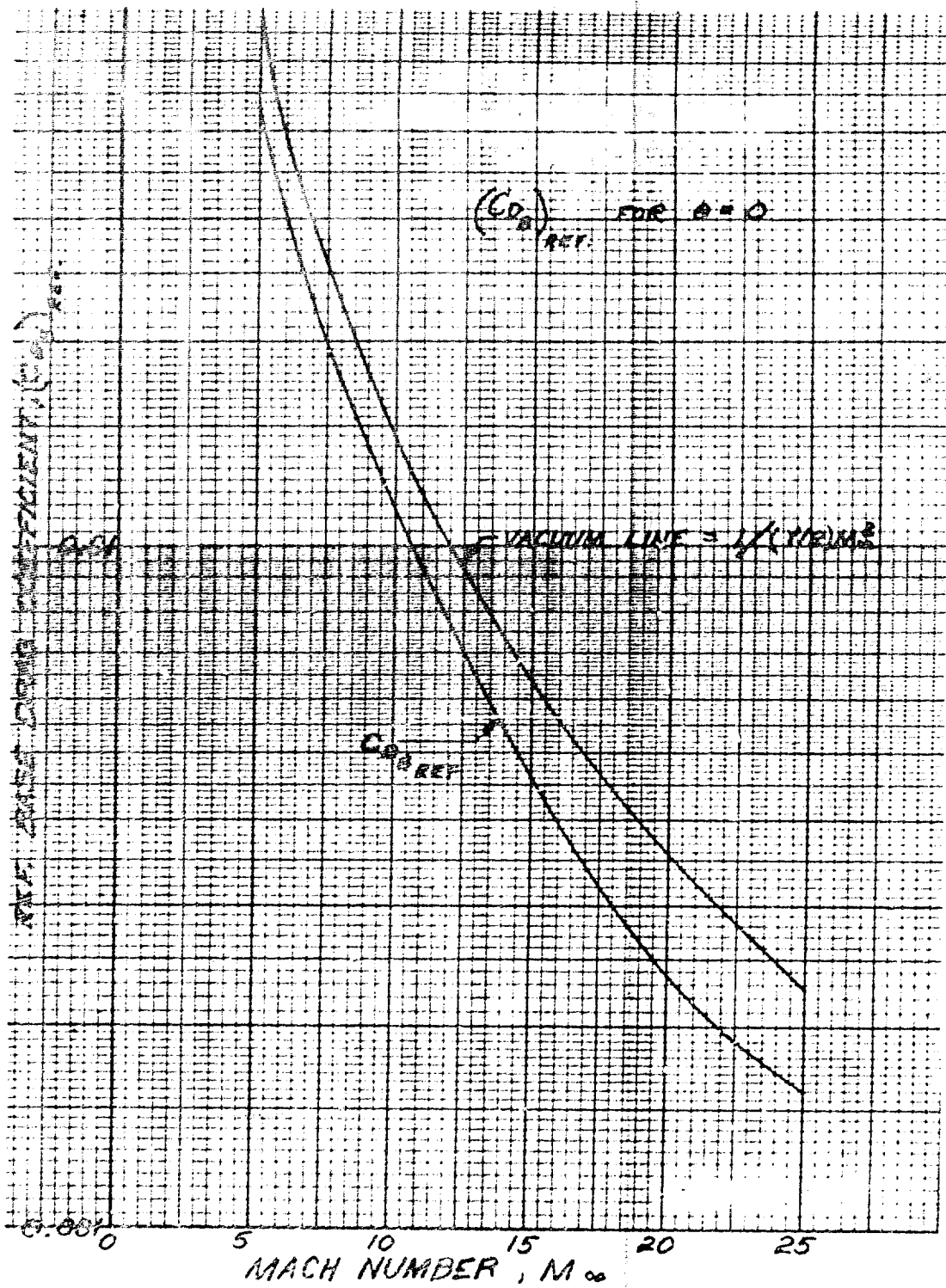


Figure 12 REFERENCE BASE - DRAG COEFFICIENT $(C_{D_B})_{REF}$ FOR $\theta = 0$

III. CONE SKIN-FRICTION DRAG

The skin-friction drag coefficient is defined by the relation,

$$C_{Df} = \frac{2\pi}{A_B} \int_0^L C_{f_w} \cos \theta r dx$$

where C_{f_w} is the local skin-friction coefficient defined by the relation,

$$C_{f_w} = \frac{\tau_w}{\frac{1}{2} \rho_\infty u_\infty^2}$$

The following two sections are devoted to the derivation of the equations for C_{Df} in both laminar and turbulent flow conditions for a sharp cone at $\alpha = 0$.

A. Sharp Cone, Laminar Flow, $\alpha = 0$

To compute the local skin-friction coefficient, we employ the Blasius flat plate incompressible solution modified for: 1) conical flow by the Mangler transformation (reference 18); 2) compressibility by Eckert's reference enthalpy method (reference 19); and 3) conversion from conditions at the edge of the boundary layer to free-stream conditions; i. e.,

$$C_{f_w} = C_{f_e} \frac{\rho_e u_e^2}{\rho_\infty u_\infty^2}$$

The modified Blasius equation is then,

$$C_{f_w} = \frac{0.664}{\sqrt{Re_x}} \sqrt{3} \sqrt{\frac{\rho^* \mu^*}{\rho_e \mu_e}} \left(\frac{\rho_e u_e^2}{\rho_\infty u_\infty^2} \right)$$

Since

$$Re_x = \frac{\rho_e u_e x}{\mu_e}$$

$$C_{f_w} = \frac{1.15}{\sqrt{x}} \frac{\rho_e^{0.5} u_e^{1.5} \mu_e^{0.5} \rho^{*0.5} \mu^{*0.5}}{\rho_\infty u_\infty^2 \rho_e^{0.5} \mu_e^{0.5}} = \frac{1.15}{\sqrt{x}} \frac{u_e^{1.5} \rho^{*0.5} \mu^{*0.5}}{\rho_\infty u_\infty^2}$$

Setting $Re_x = \frac{\rho_\infty u_\infty x}{\mu_\infty}$ and re-arranging, we obtain,

$$C_{f_w} = \frac{1.15}{\sqrt{Re_x}} \left(\frac{u_e}{u_\infty} \right)^{1.5} \sqrt{\frac{\rho^* \mu^*}{\rho_\infty \mu_\infty}}$$

Employing the curve-fit results of reference 20,

$$\sqrt{\frac{p^*}{p_{\infty}} \frac{h^*}{h_{\infty}}} = \left(\frac{p^*}{p_{\infty}}\right)^{0.5} \left(\frac{h^*}{h_{\infty}}\right)^{-0.185}$$

Since $p^* = p_e$, and $\frac{h^*}{h_{\infty}} = \frac{h^*}{h_e} \left(\frac{T_e}{T_{\infty}}\right)$ (assuming $C_{p_e} = C_{p_{\infty}}$)

$$C_{f_{\infty}} = \frac{1.15}{\sqrt{R_{\infty x}}} \left(\frac{u_e}{u_{\infty}}\right)^{1.5} \left(\frac{p_e}{p_{\infty}}\right)^{0.5} \left(\frac{T_e}{T_{\infty}}\right)^{-0.185} \left(\frac{h^*}{h_e}\right)^{-0.185}$$

where

$$\begin{aligned} \frac{h^*}{h_e} &= 0.5 + 0.5 \frac{h_w}{h_e} + 0.22 r \left(\frac{\gamma-1}{2}\right) M_e^2 \\ &= 0.5 + 0.5 \frac{T_w}{T_{\infty}} \left(\frac{T_e}{T_{\infty}}\right)^{-1} + 0.0374 M_e^2 \quad \text{assuming } \begin{cases} \gamma = 1.4, r = 0.85 \\ C_{p_e} = C_{p_{\infty}} = C_{p_w} \end{cases} \end{aligned}$$

the ratios, $\left(\frac{u_e}{u_{\infty}}\right)$, $\left(\frac{p_e}{p_{\infty}}\right)$, and $\left(\frac{T_e}{T_{\infty}}\right)$ are obtained from conical flow results which have been correlated as a function of the hypersonic similarity parameter, $M_{\infty} \sin \theta$. These correlations are valid for the range of this investigation which is $0.7 \leq M_{\infty} \sin \theta \leq 6.5$. This range is specified by an 8° cone at $M_{\infty} = 5$ as the lower limit, and a 15° cone at $M_{\infty} = 25$ as the upper limit. The velocity ratio (u_e/u_{∞}) is obtained from the conical flow results presented in reference 21. A curve-fit of these results yield:

$$\frac{u_e}{u_{\infty}} = \left[1 - \frac{1.4}{M_{\infty}^2} (M_{\infty} \sin \theta)^{1.9} \right]^{0.5}$$

The pressure ratio (p_e/p_{∞}) is obtained from the curve-fit relation presented in reference 22,

$$\frac{p_e}{p_{\infty}} = 1 + 2.8 M_{\infty}^2 \sin^2 \theta \left[\frac{2.5 + 8 M_{\infty} \sin \theta}{1 + 16 M_{\infty} \sin \theta} \right]$$

The temperature ratio (T_e/T_{∞}) is obtained from the conical flow solutions presented in reference 1. A curve-fit of these results yield:

$$\frac{T_e}{T_\infty} = 1 + 0.0966 M_\infty \sin \theta + 0.2267 (M_\infty \sin \theta)^2$$

The local Mach number is then computed from,

$$M_e = M_\infty \left(\frac{u_e}{u_\infty} \right) \left(\frac{T_e}{T_\infty} \right)^{-0.5}$$

Since the local skin-friction coefficient is now defined in terms of free-stream conditions, wall temperature, and cone angle, we may now integrate over the cone surface to obtain the skin-friction drag. Therefore,

$$C_{Df} = \frac{1}{\pi R_B^2} \int_0^L C_{f_\infty} \cos \theta (2\pi r) dx$$

Since

$$C_{f_\infty} = (C_{f_\infty})_{x=L} \left(\frac{L}{x} \right)^{0.5} \quad \text{and} \quad r = x \sin \theta$$

$$C_{Df} = \frac{2}{R_B^2} (C_{f_\infty})_{x=L} L^{0.5} \cos \theta \sin \theta \int_0^L x^{0.5} dx$$

$$= \frac{4}{3} (C_{f_\infty})_{x=L} \frac{\cos \theta \sin \theta}{R_B^2} L^2$$

Since

$$R_B^2 = L^2 \sin^2 \theta$$

and

$$(C_{f_\infty})_{x=L} = \frac{1.15}{\sqrt{R_{\infty L}}} \left(\frac{u_e}{u_\infty} \right)^{1.5} \left(\frac{P_e}{P_\infty} \right)^{0.5} \left(\frac{T_e}{T_\infty} \right)^{-0.185} \left(\frac{b^*}{b_e} \right)^{-0.185}$$

we obtain the final result for laminar flow,

$$(C_{Df})_{Lam.} = \frac{1.53}{\sqrt{R_{\infty L}}} \left(\frac{u_e}{u_\infty} \right)^{1.5} \left(\frac{P_e}{P_\infty} \right)^{0.5} \left(\frac{T_e}{T_\infty} \right)^{-0.185} \left(\frac{b^*}{b_e} \right)^{-0.185} \cos \theta$$

The solution of this equation is presented in figure 1² for 8° and 15° cones.

B. Sharp Cone, Turbulent Flow, $\alpha = 0$

We shall employ the Blasius flat plate incompressible solution modified by the conical flow transformation factor reported in reference 23, modified for compressibility by the reference enthalpy method (reference 19) and converted to free-stream conditions. The modified equation is then,

$$C_{f_x} = \frac{0.0592}{R_{e_x}^{0.2}} (1.18) \left(\frac{\rho^*}{\rho_e}\right)^{0.8} \left(\frac{\mu^*}{\mu_e}\right)^{0.2} \frac{\rho_e u_e^2}{\rho_\infty u_\infty^2}$$

Setting

$$R_{e_x} = R_{e_x} \left(\frac{\rho_e}{\rho_\infty}\right) \left(\frac{u_e}{u_\infty}\right) \left(\frac{\mu_\infty}{\mu_e}\right)$$

and re-arranging,

$$C_{f_x} = \frac{0.063}{R_{e_x}^{0.2}} \left(\frac{u_e}{u_\infty}\right)^{1.8} \left(\frac{\rho^*}{\rho_\infty}\right)^{0.8} \left(\frac{\mu^*}{\mu_\infty}\right)^{0.2}$$

Again employing the curve-fit results of reference 20, modified slightly in order to adequately cover the range of h^* , h_e , and h_∞ encountered in this study, we obtain,

$$\left(\frac{\rho^*}{\rho_\infty}\right)^{0.8} \left(\frac{\mu^*}{\mu_\infty}\right)^{0.2} = \left(\frac{p^*}{p_\infty}\right)^{0.8} \left(\frac{h^*}{h_\infty}\right)^{-0.58} = \left(\frac{p_e}{p_\infty}\right)^{0.8} \left(\frac{T_e}{T_\infty}\right)^{-0.58} \left(\frac{h^*}{h_e}\right)^{-0.58}$$

Assuming $C_{p_e} = C_{p_\infty} = C_{p_w}$, and setting $\gamma = 1.4$ and $r = 0.88$

$$\frac{h^*}{h_e} = 0.5 + 0.5 \left(\frac{T_w}{T_\infty}\right) \left(\frac{T_e}{T_\infty}\right)^{-1} + 0.0388 M_e^2$$

The local skin-friction equation in terms of free-stream conditions, wall temperature, and cone angle is now,

$$C_{f_x} = \frac{0.0698}{R_{e_x}^{0.2}} \left(\frac{u_e}{u_\infty}\right)^{1.8} \left(\frac{p_e}{p_\infty}\right)^{0.8} \left(\frac{h^*}{h_e}\right)^{-0.58} \left(\frac{T_e}{T_\infty}\right)^{-0.58}$$

where the "e" conditions are determined from the same equations specified in the previous paragraph.

To obtain the skin-friction drag coefficient, the local coefficients are integrated over the cone surface with the condition that

$$C_{f_x} = (C_{f_x})_{x=L} \left(\frac{L}{x}\right)^{0.2}$$

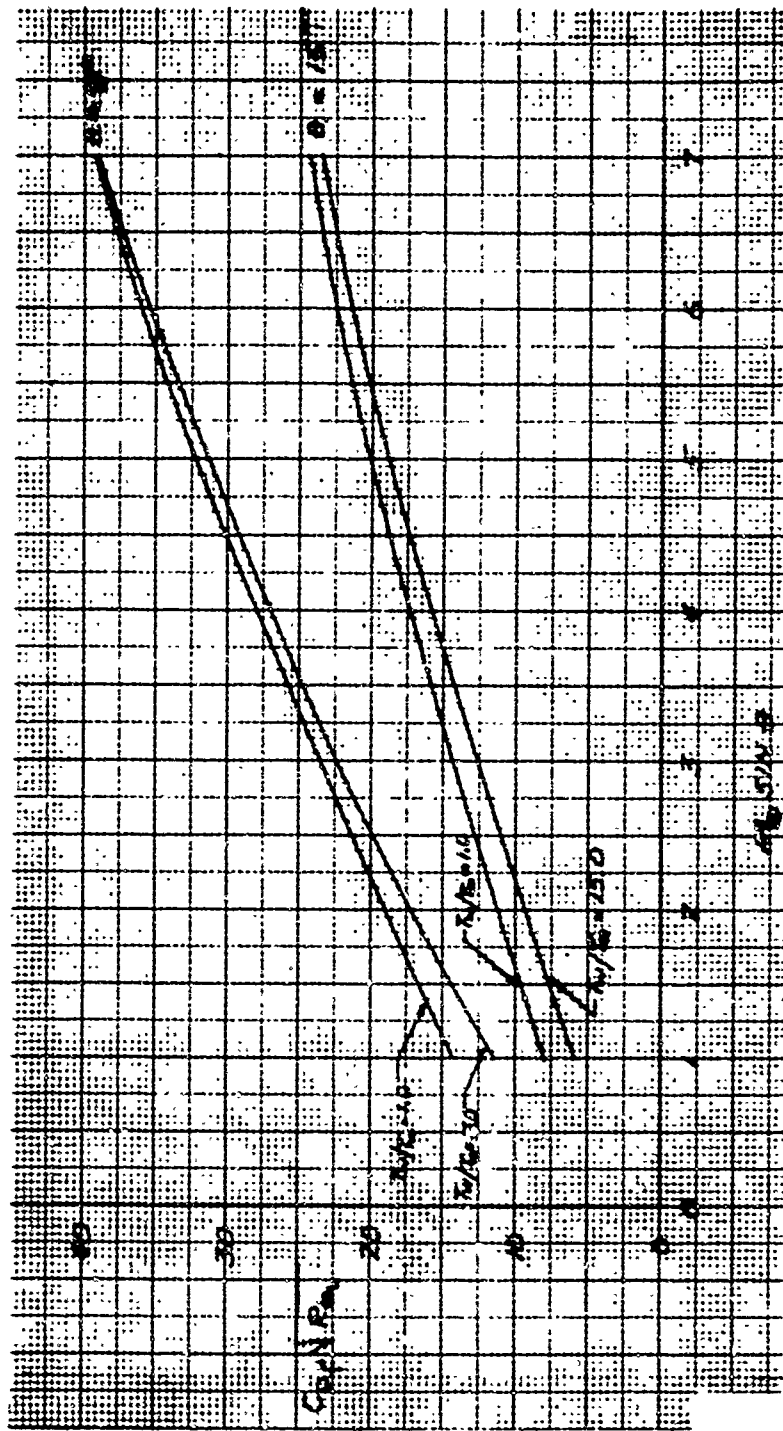


Figure 13 SKIN FRICTION DRAG COEFFICIENT, SHARP CONE, LAMINAR FLOW

Therefore,

$$C_{D_f} = \frac{2}{R_B} (C_{f_w})_{x=L} L^{0.2} \cos \theta \sin \theta \int_0^L x^{0.8} dx$$

$$= \frac{10}{9} (C_{f_w})_{x=L} \frac{\cos \theta \sin \theta}{R_B} L^2$$

Since

$$R_B^2 = L^2 \sin^2 \theta$$

and

$$(C_{f_w})_{x=L} = \frac{0.0698}{(R_{\infty L})^{0.2}} \left(\frac{u_e}{u_\infty} \right)^{1.8} \left(\frac{p_e}{p_\infty} \right)^{0.8} \left(\frac{T_e}{T_\infty} \right)^{-0.58} \left(\frac{h^*}{h_e} \right)^{-0.58}$$

we obtain the final result for turbulent flow,

$$(C_{D_f})_{\text{Turb.}} = \frac{0.0776}{(R_{\infty L})^{0.2}} \left(\frac{u_e}{u_\infty} \right)^{1.8} \left(\frac{p_e}{p_\infty} \right)^{0.8} \left(\frac{T_e}{T_\infty} \right)^{-0.58} \left(\frac{h^*}{h_e} \right)^{-0.58} \cot \theta$$

The solution of this equation is presented in figure 14, for 8° and 15° cones.

C. Bluntness Effects

The effects of nose bluntness tend to reduce the skin-friction drag compared to the sharp body case. This reduction is due primarily to the loss in dynamic pressure encountered by the free stream as it passes through a strong curved shock. An additional reduction in skin-friction is caused by the decreased cone pressure resulting from overexpansion of the flow.

To completely evaluate the effects of nose bluntness, the following methods of analysis have been employed:

- a. Method of characteristics (reference 3) (Avco Computer Program 596). This method was used to obtain the pressure distribution and shock shape.
- b. Blunt Body Viscid-Inviscid Solution (references 24 and 25) (Avco Computer Program 1115B). This method was used to compute the distribution of flow properties along the edge of the boundary layer and the resulting local skin-friction coefficients.

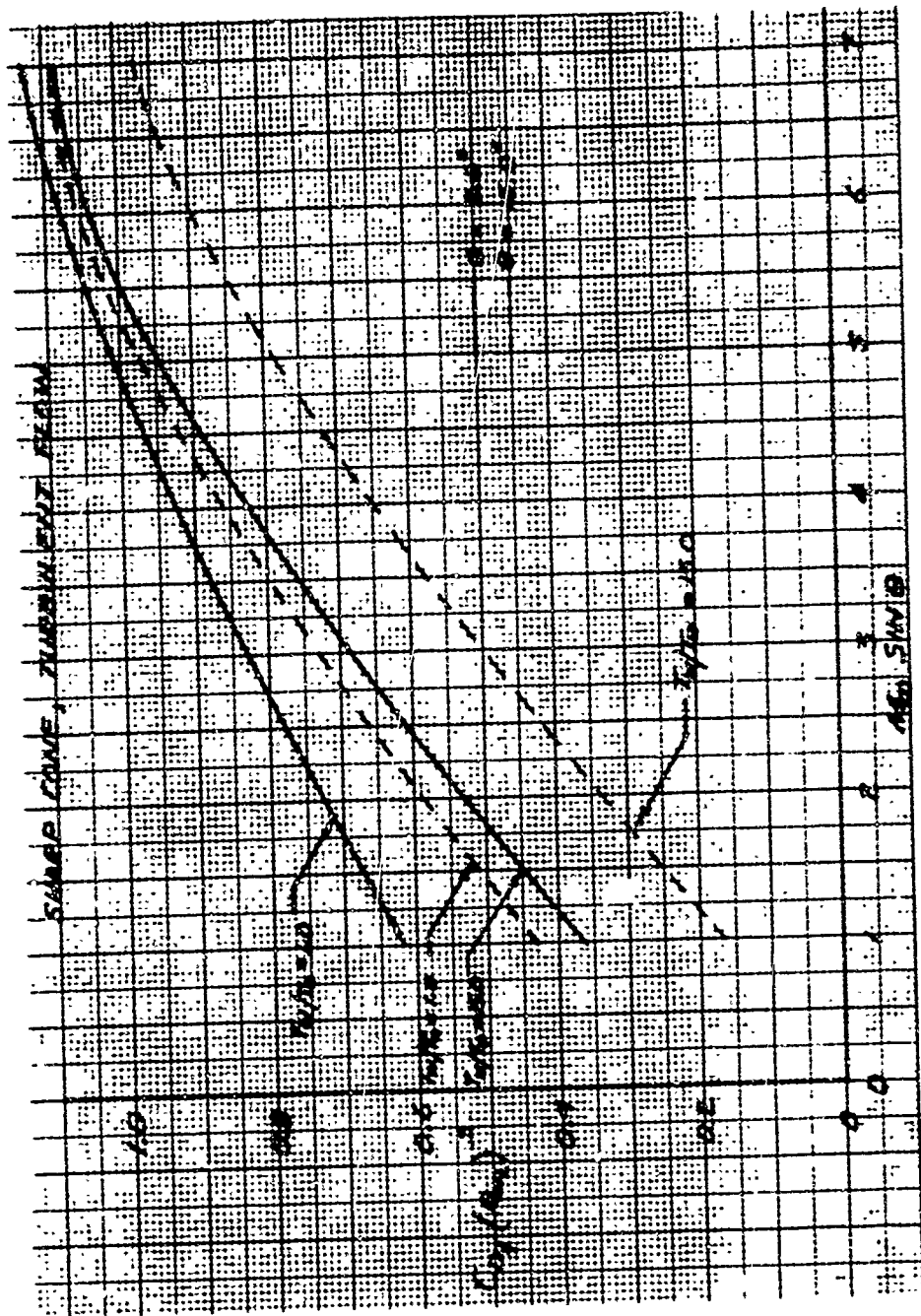


Figure 14 SKIN FRICTION DRAG COEFFICIENT, SHARP CONE, TURBULENT FLOW

In the employment of the latter method of analysis, the known parameters are free stream conditions, body geometry, surface temperature, surface pressure, and shock shape. The additional fluid property that can be evaluated along the edge of the boundary layer is entropy. This is determined from an iterative solution in which the free-stream mass flow is equated to the mass flow in the boundary layer. The analytical model used to perform this computation is shown in figure 15.

To obtain the flow properties at the edge of the boundary layer at Station "X", a value for the entropy is initially assumed. Since the pressure is known, all other properties may be computed. The mass flow in the boundary layer is then computed by employing the correlations reported in reference 24 which permit an approximate calculation of the mass flow as a function of boundary layer edge conditions and surface temperature. Employing the continuity equation between the boundary layer at Station "X" and the free stream, the bounding stream-tube radius, R_{∞} , is determined. From the known shock angle corresponding to R_{∞} , the entropy change across the shock can be computed. The resulting entropy is compared to the assumed value and iteration is made until convergence is achieved. The final fluid properties at the edge of the boundary layer are then used in the modified Blasius equation in order to compute the local skin-friction. The same procedure is then employed at the next station along the body. After all stations are computed, the local skin-friction coefficients are integrated over the surface of the body in order to obtain the skin-friction drag coefficient.

The foregoing methods of analysis have been employed in a parametric study in order to develop simplified correlations. The major problem encountered in this study is the number of variables affecting blunt body viscous drag; they are: R_N/R_B , $R_{\infty L}$, M_{∞} , θ , and T_w . Therefore a preliminary investigation was made of the relative significance of each parameter in order to determine which parameters were the most critical and which ones could be neglected.

For laminar flow it was determined that the critical parameters were R_N/R_B , and $R_{\infty L}$. Therefore, the study was conducted for fixed values of $M_{\infty} = 22$, $\theta = 10^\circ$, and $T_w = 3,000^\circ R$. The results are presented in figure 16 where the blunt body skin-friction drag is normalized by the corresponding sharp cone value. The characteristic length in the Reynolds number is the slant length (L) of the sharp cone. When the known quantities are cone angle, bluntness ratio, and blunt body axial length, the slant length is determined from the relation,

$$L = \frac{L_A}{\cos \theta - \frac{R_N}{R_B} (1 - \sin \theta)}$$

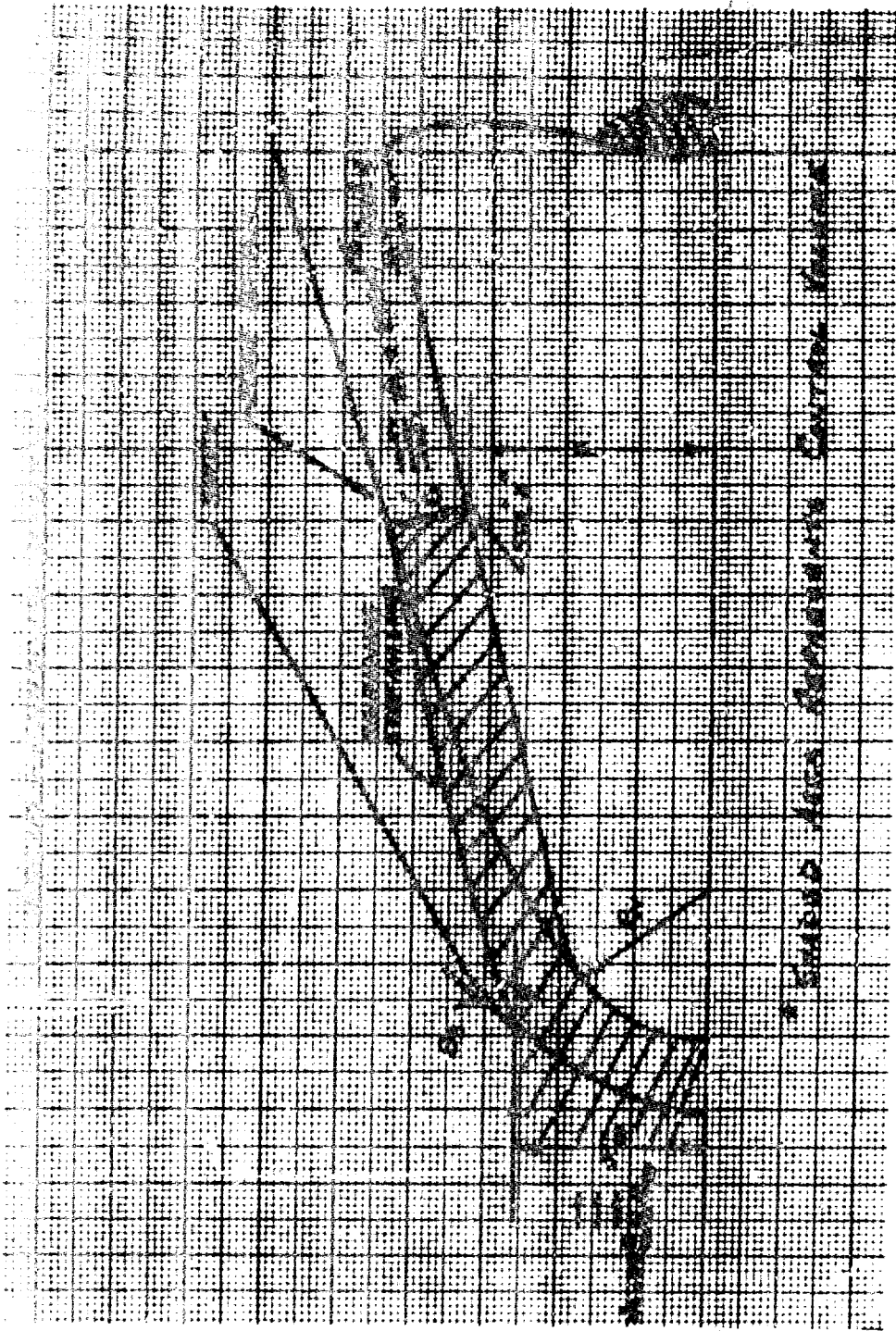


Figure 15 ANALYTICAL MODEL FOR BLUNT BODY

Best Available Copy

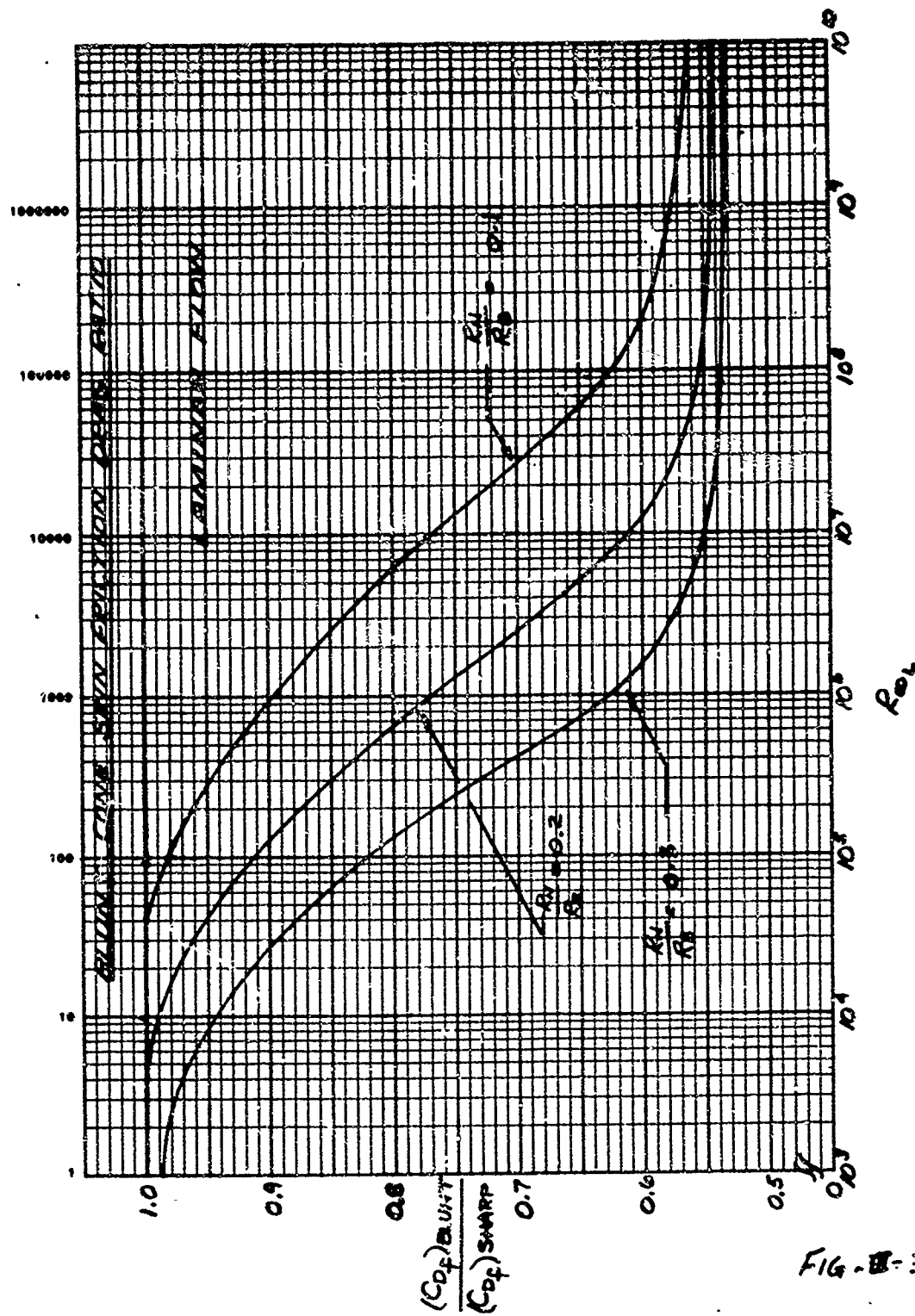


Figure 16 BLUNT CONE SKIN FRICTION DRAG RATIO, LAMINAR FLOW

The values of $R_{\infty L}$ shown in figure 16 represent many combinations of altitude and body length, and in all cases the correlation was quite satisfactory. To further confirm this correlation, a few cases were investigated with the velocity reduced by one-half. The resulting correlation was very good up to $R_{\infty L} = 10^6$; at higher Reynolds numbers there was some deviation due to Mach number effects.

The results presented in figure 16 show some interesting trends which are summarized as follows:

- (1) At low values of $R_{\infty L}$ ($< 10^4$), the bluntiness effects are negligible due to the thick boundary layer.
- (2) At high values of $R_{\infty L}$ ($> 10^9$), the boundary layer is so thin that the streamline intersecting the edge of the boundary layer at $x = L$ has passed through a region of the shock that is essentially normal. Therefore, the minimum value of the drag ratio corresponds to the case where the entropy along the boundary streamline equals the entropy behind a normal shock.

For turbulent flow, the parametric study indicated that the effect of $R_{\infty L}$ was not critical in the high Reynolds number range ($> 10^5$). The dominating effects were found to be the bluntiness ratio and free-stream Mach number. The other effects of cone angle and wall temperature were assumed to be negligible as in the case of laminar flow. The resulting variation of the skin-friction drag ratio is presented in figure 17. These results show that the ratio steadily decreases up to a bluntiness ratio of about 0.3, and then gradually approaches its asymptotic limit, which is the case of normal shock entropy at the edge of the boundary at $x = L$.

The results presented in figures 16 and 17 have been curve-fit to yield the following equations:

Laminar Flow

$$R = \frac{(C_{Df})_{Blunt}}{(C_{Df})_{Sharp}} = \left[1.0 + 9.8842 \left(\frac{R_N}{R_B} \right) - 44.0235 \left(\frac{R_N}{R_B} \right)^2 + 70.383 \left(\frac{R_N}{R_B} \right)^3 \right] - \left[\left(\frac{R_N}{R_B} \right)^{0.69 + 2.1 \frac{R_N}{R_B}} \right]^{(\log_{10} R_{\infty L})}$$

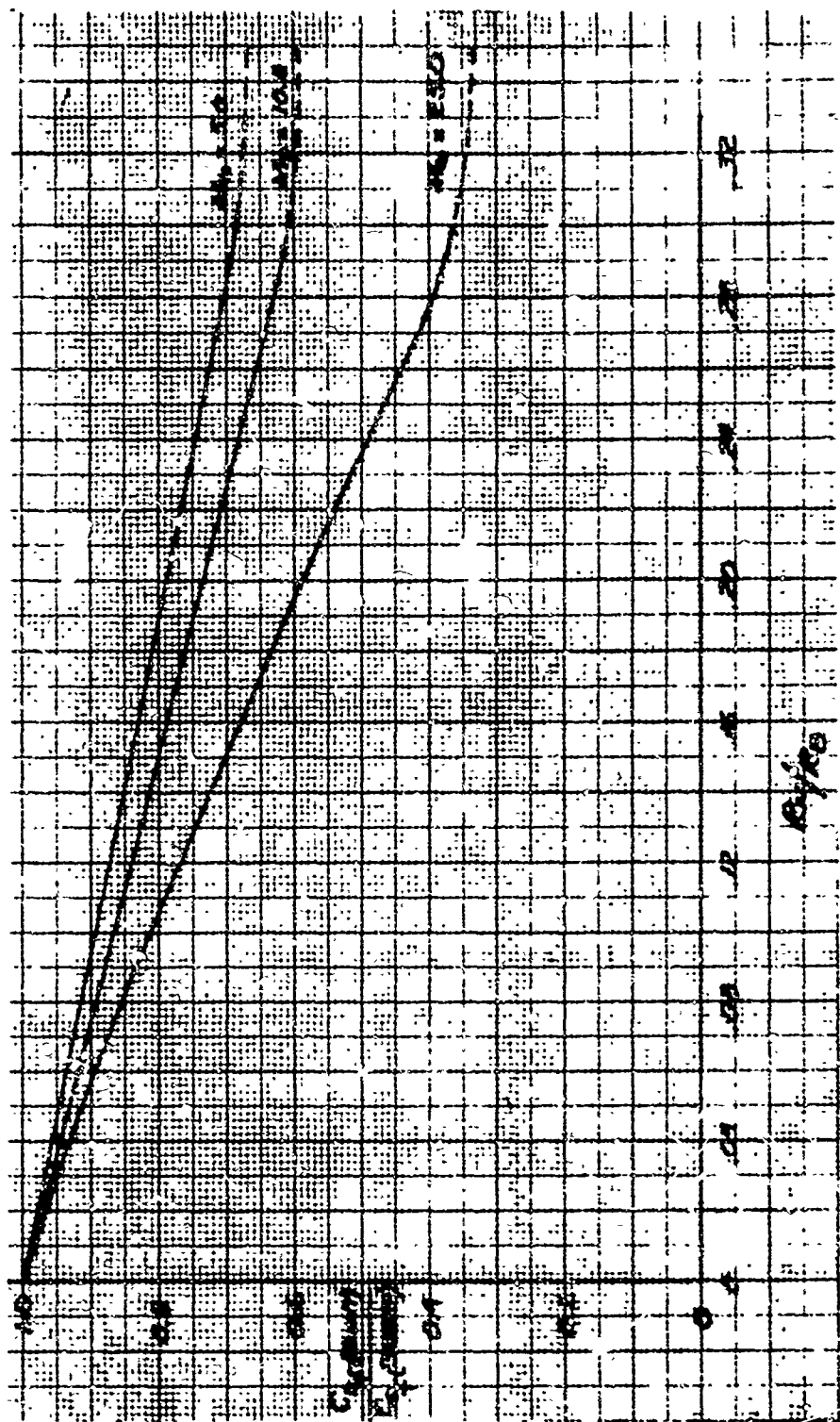


Figure 17 BLUNT CONE SKIN FRICTION DRAG RATIO, TURBULENT FLOW

with the conditions;

if $\lambda > 1.0$, set equal to 1.0

if $R < R_{\min}$: set equal to R_{\min}

$$\text{where } R_{\min} = 1.0 - 6.5076 \left(\frac{R_N}{R_B} \right) + 30.46 \left(\frac{R_N}{R_B} \right)^2 - 46.85 \left(\frac{R_N}{R_B} \right)^3$$

Turbulent Flow

$$\frac{(C_{Df})_{\text{Blunt}}}{(C_{Df})_{\text{Sharp}}} = 1.0 - \left[(0.8 + 0.052 M_\infty) \frac{R_N}{R_B} \right]$$

D. Angle of Attack Effects

There is presently no reliable solution available for the calculation of skin-friction drag on yawed axi-symmetric bodies. According to the results of reference 26, the cross-flow effects on the windward and side meridians are relatively small up to yaw angles equal to the cone angle. This implies that for $\alpha \leq \theta$, the Blasius solution can be employed with tangent-cone approximations for evaluating the fluid properties. Since a requirement of this study includes the evaluation of skin-friction drag on sharp and blunt cones up to 20° angle of attack, the assumption will have to be made that the modified Blasius solution is still valid over this entire range when the fluid properties are evaluated using tangent-cone approximations for the windward, leeward, and side meridians. Therefore, for the case of a sharp cone in laminar flow,

$$\left[(C_{Df})_a \right]_{\text{Lam.}} = \frac{1.53}{\sqrt{R_{\infty L}}} \left(\frac{\bar{u}_e}{u_\infty} \right)^{1.5} \left(\frac{\bar{p}_e}{p_\infty} \right)^{0.5} \left(\frac{\bar{T}_e}{T_\infty} \right)^{-0.185} \left(\frac{h^*}{h_e} \right)^{-0.185} \cot \theta$$

where:

$$\frac{\bar{u}_e}{u_\infty} = \left\{ 1 - \frac{0.35}{M_\infty^{0.1}} \left[\sin^{1.9}(\theta + \alpha) + \sin^{1.9}(\theta - \alpha) + 2 \sin^{1.9} \theta \right] \right\}^{0.5}$$

$$\frac{\bar{p}_e}{p_\infty} = 1 + 0.7 M_\infty^2 \left\{ \sin^2(\theta + \alpha) \left[\frac{2.5 + 8 M_\infty \sin(\theta + \alpha)}{1 + 16 M_\infty \sin(\theta + \alpha)} \right] \right. \\ \left. + \sin^2(\theta - \alpha) \left[\frac{2.5 + 8 M_\infty \sin(\theta - \alpha)}{1 + 16 M_\infty \sin(\theta - \alpha)} \right] + 2 \sin^2 \theta \left[\frac{2.5 + 8 M_\infty \sin \theta}{1 + 16 M_\infty \sin \theta} \right] \right\}$$

$$\frac{\bar{T}_e}{\bar{T}_\infty} = 1 + 0.02415 M_\infty [\sin(\theta + \alpha) + \sin(\theta - \alpha) + 2 \sin \theta] \\ + 0.0567 M_\infty^2 [\sin^2(\theta + \alpha) + \sin^2(\theta - \alpha) + 2 \sin^2 \theta]$$

$$\frac{\bar{h}^*}{h_e} = 0.5 + 0.5 \left(\frac{\bar{T}_w}{\bar{T}_\infty} \right) \left(\frac{\bar{T}_e}{\bar{T}_\infty} \right)^{-1} + 0.0374 \bar{M}_e^2$$

$$\bar{M}_e = M_\infty \left(\frac{\bar{u}_e}{u_\infty} \right) \left(\frac{\bar{T}_e}{\bar{T}_\infty} \right)^{-0.5}$$

with the condition that,

if $(\theta - \alpha) < 0$, set equal to zero.

For the case of turbulent flow, this same procedure for evaluating the average fluid properties is utilized in the zero angle of attack equation. Therefore,

$$[(C_{Df})_a]_{\text{Turb.}} = \frac{0.0776}{R_{\infty L}^{0.2}} \left(\frac{\bar{u}_e}{u_\infty} \right)^{1.8} \left(\frac{\bar{p}_e}{p_\infty} \right)^{0.8} \left(\frac{\bar{T}_e}{\bar{T}_\infty} \right)^{-0.58} \left(\frac{\bar{h}^*}{h_e} \right)^{-0.58} \cos \theta$$

For the case of the blunt cone, it is assumed that the skin friction drag ratios presented in figures 16 and 17 are still applicable.

E. Mass Addition Effects

The effect of mass addition due to ablation tends to reduce the skin-friction drag. To rigorously account for this effect, the following analyses should be employed:

- 1) Evaluation of thermodynamic and transport properties of the injected gas, employing Avco RAD digital computer programs 1291 and 1619B. (References 27 and 28).
- 2) Using the thermodynamic and transport properties in the solution of the boundary layer equations for both laminar and turbulent flow (Avco RAD digital computer programs 1475 and 1356, respectively, references 29 and 30).
- 3) Correlation of the skin-friction reduction ratio (C_f/C_{f_0}) as a function of the blowing parameter, $\frac{2 \dot{m}}{\rho_e u_e C_{f_0}}$.

Since the original requirements for this drag study did not include mass addition effects, the rigorous methods of analysis have not been employed. However, provided herein is a simplified approximate method which yields reasonable results for most heat shield materials. This method, which has been reported in reference 31, employs the following assumptions:

- a) The mass injection rate (\dot{m}) can be computed from an effective heat of ablation (q^*) and the heat flux to a non-ablating wall (\dot{q}_0). Therefore,

$$\dot{m} = \frac{\dot{q}_0}{q^*}$$

- b) The heat of ablation can be obtained from the relation,

$$q^* = C_p \Delta T + H_v + \eta (h_s - h_w)$$

(total energy absorbed) (energy lost by transpiration)

$$= H_T + \eta (h_s - h_w)$$

- c) Reynolds analogy is valid; i. e., $C_f / C_{f_0} = \dot{q} / \dot{q}_0$

The energy balance required at the wall is then,

$$\dot{q} = \dot{m} H_T$$

$$= \frac{\dot{q}_0}{q^*} H_T = \frac{\dot{q}_0 H_T}{H_T + \eta (h_s - h_w)}$$

Solving for \dot{q} / \dot{q}_0 , and setting equal to C_f / C_{f_0} , we obtain,

$$\frac{C_f}{C_{f_0}} = \frac{H_T}{H_T + \eta (h_s - h_w)}$$

This skin-friction reduction ratio due to mass addition effects is presented in figure 18 for laminar and turbulent flow for various heat shield materials. The ablation properties used in this approximate method are:

Material	T_w ($^{\circ}R$)	H_w / RT_0	H_T (Btu/lb)	η_{Turb}	η_{Lam}
LTa	1370	9.9	745	0.41	0.57
Teflon	1800	13.4	800	0.255	0.43
OTWR	4850	42.0	3200	0.32	0.50

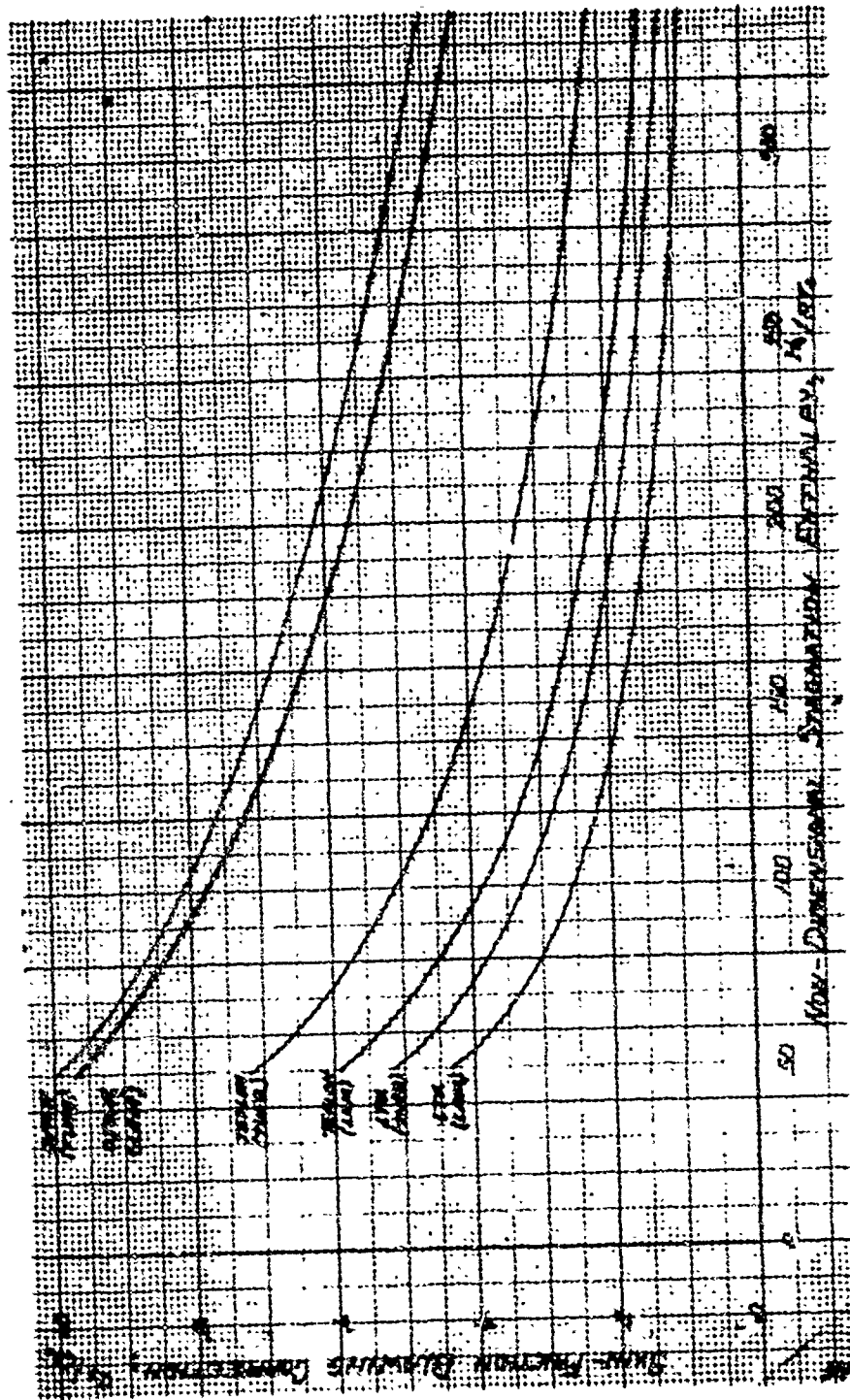


Figure 18 SKIN-FRICTION BLOWING CORRECTION, LT₂, OTWR AND TEFLON HEAT SHIELDS

IV CONE INDUCED DRAG

The induced drag resulting from a thick boundary layer around a slender body has been considered by Probstein (reference 32) and others for the case of laminar flow with no mass injection. It has been shown by Probstein that for sharp slender cones, the induced effects may be computed from "weak interaction" considerations; i. e., the induced pressure gradient does not significantly effect the boundary layer growth. For slightly blunted cones, there is a region of "strong interaction" starting immediately aft of the stagnation point and extending a few nose radii downstream. However, for purposes of computing induced drag, this region has a relatively small effect, and weak interaction assumptions may be employed throughout.

The total induced drag can be considered to be the summation of three effects as follows:

1. Induced Pressure Drag

This effect is due to a new apparent body shape represented by the displacement thickness profile. Employing the tangent-cone assumption, the new effective cone angle, $\theta_{eff} = \theta + \frac{d\delta^*}{dx}$. Since $d\delta^*/dx$ decreases as x increases, the induced pressure is greatest near the leading edge, and decays at a rate which is proportional to \sqrt{x} .

2. Pressure Induced Skin Friction Drag

This effect is due to the increase in local skin friction as a result of increased local pressure. As in the case of induced pressure, this effect is greatest near the leading edge.

3. Transverse-Curvature Induced Skin Friction Drag

This effect arises when the boundary layer thickness is not negligible compared to the body radius of curvature. The negligibly thin boundary layer assumption was made by Mangler (reference 18) when he transformed the boundary layer equations for an axi-symmetric body to a flat plate. Therefore, the transverse-curvature correction is used to modify the well-known Mangler transformation factor.

The following paragraphs present the derivations employed to compute induced drag in terms of free stream conditions. Results are presented for laminar flow only, since induced drag is negligible in turbulent flow when $\theta \geq 8^\circ$.

A. Induced Pressure Drag, Sharp Cone, $\alpha = 0$

Employing Probstein's equation for the local increased pressure on a sharp cone (neglecting second order terms of the series expansion),

$$\frac{\Delta P}{P_e} = F_1(K) d_m \bar{\chi}_e$$

where:

$$\bar{\chi}_e = \frac{\sqrt{C_e} M_e^3}{\sqrt{R_{ex}}} \quad \text{with} \quad C_e = \frac{\mu_w}{\mu_e} \frac{T_e}{T_w}$$

$$d_m = \frac{0.968}{M_\infty^2} \frac{T_w}{T_\infty} + 0.058 \quad (\text{For } \gamma = 1.4 \text{ and } Pr = 0.72)$$

$$F_1(K) = \frac{1}{\sqrt{3} \left(\frac{P_e}{P_\infty} \right)} \left[\frac{1}{M_\infty} \frac{d(p_e/p_\infty)}{d\theta} \right]_{\theta=\theta_c} \left(\frac{M_e}{M_\infty} \right)$$

which is a function of $M_\infty \sin \theta$ and γ . A curve-fit of $F_1(K)$ for $\gamma = 1.4$ yields,

$$F_1(K) = 0.9 - 0.119 M_\infty \sin \theta + 0.0108 (M_\infty \sin \theta)^2$$

In order to obtain the viscous interaction parameter $\bar{\chi}_e$ in terms of free-

stream conditions, $\bar{\chi}_e = \frac{\sqrt{C_\infty}}{\sqrt{R_{ex}}} M_\infty^3$, we write:

$$\frac{\bar{\chi}_e}{\bar{\chi}_\infty} = \left(\frac{C_e}{C_\infty} \right)^{0.5} \left(\frac{\rho_e}{\rho_\infty} \right)^{-0.5} \left(\frac{u_e}{u_\infty} \right)^{-0.5} \left(\frac{\mu_w}{\mu_e} \right)^{-0.5} \left(\frac{M_e}{M_\infty} \right)^3$$

where:

$$\frac{\mu_w}{\mu_e} = \left(\frac{T_w}{T_e} \right)^{0.6}$$

(This viscosity-temperature power law is assumed throughout)

$$\frac{C_e}{C_\infty} = \frac{\mu_w}{\mu_e} \frac{T_e}{T_\infty} = \left(\frac{T_e}{T_w} \right)^{0.4}$$

$$\frac{\rho_e}{\rho_\infty} = \left(\frac{P_e}{P_\infty} \right) \left(\frac{T_e}{T_\infty} \right)^{-1}$$

$$\frac{M_e}{M_\infty} = \frac{u_e}{u_\infty} \left(\frac{T_e}{T_\infty} \right)^{-0.5}$$

Substituting,

$$\frac{\bar{X}_e}{X_\infty} = \left(\frac{T_e}{T_\infty}\right)^{0.4} \left(\frac{p_e}{p_\infty}\right)^{-0.5} \left(\frac{T_e}{T_\infty}\right)^{0.5} \left(\frac{u_e}{u_\infty}\right)^{-0.5} \left(\frac{T_e}{T_\infty}\right)^{0.3} \left(\frac{u_e}{u_\infty}\right)^3 \left(\frac{T_e}{T_\infty}\right)^{-1.5}$$

$$= \left(\frac{p_e}{p_\infty}\right)^{-0.5} \left(\frac{T_e}{T_\infty}\right)^{-0.3} \left(\frac{u_e}{u_\infty}\right)^{2.5}$$

for $C_w = \left(\frac{T_\infty}{T_w}\right)^{0.4}$, we obtain

$$\bar{X}_e = \left(\frac{M_\infty^3}{\sqrt{R_{ax}}}\right) \left(\frac{T_\infty}{T_w}\right)^{0.2} \left(\frac{p_e}{p_\infty}\right)^{-0.5} \left(\frac{T_e}{T_\infty}\right)^{-0.3} \left(\frac{u_e}{u_\infty}\right)^{2.5}$$

The ratios, p_e/p_∞ , T_e/T_∞ , and u_e/u_∞ are a function of $M_\infty \sin \theta$ and are obtained from the relations given in section III.

Therefore, the equation for local induced pressure with all quantities in terms of free-stream conditions is:

$$\frac{\Delta p}{p_e} = K x^{-0.5}$$

where:

$$K = \left(\frac{0.968}{M_\infty^2} \frac{T_w}{T_\infty} + 0.058\right) \frac{M_\infty^3}{\sqrt{R_{ax}}} \left(\frac{T_\infty}{T_w}\right)^{0.2} \left(\frac{p_e}{p_\infty}\right)^{-0.5} \left(\frac{T_e}{T_\infty}\right)^{-0.3} \left(\frac{u_e}{u_\infty}\right)^{2.5} F_1(K)$$

To obtain the induced pressure drag, it is then necessary to integrate this equation over the cone surface. To account for nose bluntness effects, some approximations must be made in order to integrate the equation in closed form. (1) The value of the induced pressure at the sphere-cone tangent point is assumed to equal the value for the corresponding sharp cone case for the local Mach number and temperature associated with the blunt body, (2) The local flow properties are assumed to be invariant with x , and, (3) the induced pressure on the spherical nose is a negligible amount.

The body geometry employed, for the induced drag calculations is shown in figure 19.

The integration will now be performed in such a manner that when $R_N/R_B = 0$, the solution degenerates to the sharp body case.

$$\Delta C_{Dp} = \frac{1}{q_\infty \pi R_B^2} \int_{R_N \cos \theta}^{R_B} \left(\frac{\Delta p}{P_e} \right) P_e (2\pi r) dr$$

$$= \frac{2}{q_\infty R_B^2} \int_{R_N \cos \theta}^{R_B} (K x^{-0.5}) P_e r dr$$

Since

$$\frac{P_e}{q_\infty} = C_{Dp} \quad \text{and} \quad x = \frac{r}{\sin \theta}$$

$$\Delta C_{Dp} = 2 C_{Dp} \frac{K}{R_B^2} (\sin \theta)^{0.5} \int_{R_N \cos \theta}^{R_B} r^{0.5} dr$$

$$= \frac{4}{3} C_{Dp} \frac{K}{R_B^2} (\sin \theta)^{0.5} \left[R_B^{3/2} - (R_N \cos \theta)^{3/2} \right]$$

$$= \frac{4}{3} C_{Dp} K \left(\frac{\sin \theta}{R_B} \right)^{0.5} \left[1 - \left(\frac{R_N}{R_B} \cos \theta \right)^{3/2} \right]$$

Since $\frac{R_B}{\sin \theta} = L$, we obtain

$$\Delta C_{Dp} = \frac{4}{3} C_{Dp} K \left[1 - \left(\frac{R_N}{R_B} \cos \theta \right)^{3/2} \right] L^{-0.5}$$

B. Pressure Induced Skin-Friction Drag, Sharp Cone, $\alpha = 0$

Employing Probstein's first order solution for the local induced skin-friction coefficient, and assuming $\gamma = 1.4$, we obtain,

$$\frac{(\Delta C_f)_p}{C_f} = \left[-0.823 + 0.524 \frac{T_w/T_\infty}{T_e/T_\infty} + 0.438 M_e^2 \right] \frac{d_\infty F_1(K)}{M_e^2}$$

where d_w , $F_1(K)$, and \bar{x}_e are evaluated in the same manner as for the case of induced pressure.

Therefore,

$$\frac{(\Delta C_f)_p}{C_f} = K' x^{-0.5}$$

where:

$$K' = \left[-0.823 + 0.524 \frac{T_w/T_\infty}{T_e/T_\infty} + 0.438 M_e^2 \right] \frac{d_w F_1(K)}{M_e^2} \frac{M_\infty^3}{\sqrt{R_\infty}} \left(\frac{T_\infty}{T_w} \right)^{0.2} \left(\frac{P_e}{P_\infty} \right)^{-0.5} \left(\frac{T_e}{T_\infty} \right)^{-0.3} \left(\frac{u_e}{u_\infty} \right)^{2.5}$$

Employing the same blunt body approximations as previously discussed, we may now integrate in closed form:

$$\begin{aligned} (\Delta C_{Df})_p &= \frac{1}{\pi R_B^2} \int_l^L \frac{(\Delta C_f)_p}{C_f} \cdot C_f \cos \theta (2\pi r) dx \\ &= \frac{2}{R_B^2} \int_l^L K' x^{-0.5} C_f \cos \theta r dx \end{aligned}$$

Since

$$r = x \sin \theta \quad \text{and} \quad C_f = (C_f)_{x=l} \left(\frac{l}{x} \right)^{0.5}$$

we obtain:

$$\begin{aligned} (\Delta C_{Df})_p &= \frac{2}{R_B^2} K' \sin \theta \cos \theta (C_f)_{x=l} \int_l^L x^{-0.5} \left(\frac{l}{x} \right)^{0.5} x dx \\ &= \frac{2}{R_B^2} K' \sin \theta \cos \theta (C_f)_{x=l} l^{0.5} (L-l) \end{aligned}$$

For the non-interacting sharp cone case, it may be shown that (see section III):

$$C_{Df} = \frac{4}{3} (C_f)_{x=l} l^{0.5} \frac{\cos \theta}{\sin \theta} L^{-0.5}$$

or

$$(C_f)_{x=l} = \frac{3}{4} \frac{\sin \theta}{\cos \theta} l^{-0.5} L^{0.5} C_{Df}$$

Substituting in the induced drag equation,

$$(\Delta C_{Df})_p = \frac{3}{2} K' C_{L_f} \frac{\sin^2 \theta}{R_B^2} (L^{1.5} - l L^{0.5})$$

Since

$$R_B^2 = L^2 \sin^2 \theta \quad \text{and} \quad l = \frac{R_N}{R_B} L \cos \theta,$$

we obtain

$$\boxed{(\Delta C_{Df})_p = \frac{3}{2} K' C_{Df} \left(1 - \frac{R_N}{R_B} \cos \theta\right) L^{-0.5}}$$

C. Traverse Curvature Induced Skin-Friction Drag, Sharp Cone, $\alpha = 0$

Employing Probstein's first order solution for the local induced transverse curvature effect, and again assuming $\gamma = 1.4$, we obtain

$$\frac{(\Delta C_f)_{t.c.}}{C_f} = \left[0.517 + 0.913 \frac{T_w/T_\infty}{T_e/T_\infty} + 0.0484 M_e^2 \right] \frac{\bar{x}_e}{\sqrt{3} M_e^3 \tan \theta}$$

$$= K'' x^{-0.5}$$

where:

$$K'' = \left[0.517 + 0.913 \frac{T_w/T_\infty}{T_e/T_\infty} + 0.0484 M_e^2 \right] \frac{1}{\sqrt{3} M_e^3 \tan \theta} \frac{M_\infty^3}{\sqrt{R_\infty}} \left(\frac{T_\infty}{T_w} \right)^{0.2} \left(\frac{P_e}{P_\infty} \right)^{-0.5} \left(\frac{T_e}{T_\infty} \right)^{-0.3} \left(\frac{u_e}{u_\infty} \right)^{2.5}$$

The integration is performed in exactly the same manner as the pressure induced skin-friction drag. Therefore,

$$\left(\Delta C_{Df}\right)_{t.c.} = \frac{3}{2} K'' C_{Df} \left(1 - \frac{R_N}{R_B} \cos \theta\right) L^{-0.5}$$

The results of some induced drag calculations are presented in figures 20 to 23 for sharp 8° and 15° cones.

These results consist of induced pressure drag (ΔC_{Dp}) and the total induced skin-friction drag, $(\Delta C_{Df})_p + (\Delta C_{Df})_{t.c.}$.

The calculations indicate the following:

- a. The ratio $\frac{\Delta C_{Df}}{C_{Df}}$ is significantly greater than the ratio $\frac{\Delta C_{Dp}}{C_{Dp}}$.
- b. The more slender cone experiences much higher induced drag than the steep angle cone.
- c. Induced drag increases with wall temperature.
- d. The effect of increasing free-stream Mach number generally increases the induced drag (however, there is a reversal effect at high values of wall temperature).

The total induced drag coefficient is then,

$$C_{Di} = \Delta C_{Dp} + (\Delta C_{Df})_p + (\Delta C_{Df})_{t.c.}$$

D. Bluntness Effects

For the case of the blunt cone, the flow conditions at the edge of the boundary layer vary with x for two reasons; (1) the pressure distribution is not constant as in the sharp body case, and (2) the curved shock produces an entropy gradient along the edge of the boundary layer.

Since the integration scheme presented in the previous paragraphs is valid only for constant flow properties, several assumptions must be made in evaluating effective constant conditions. This approach is very approximate, but it is justified on the grounds that for a blunt body the induced drag is a very small portion of the total drag; in fact, it is most often neglected without any consequences.

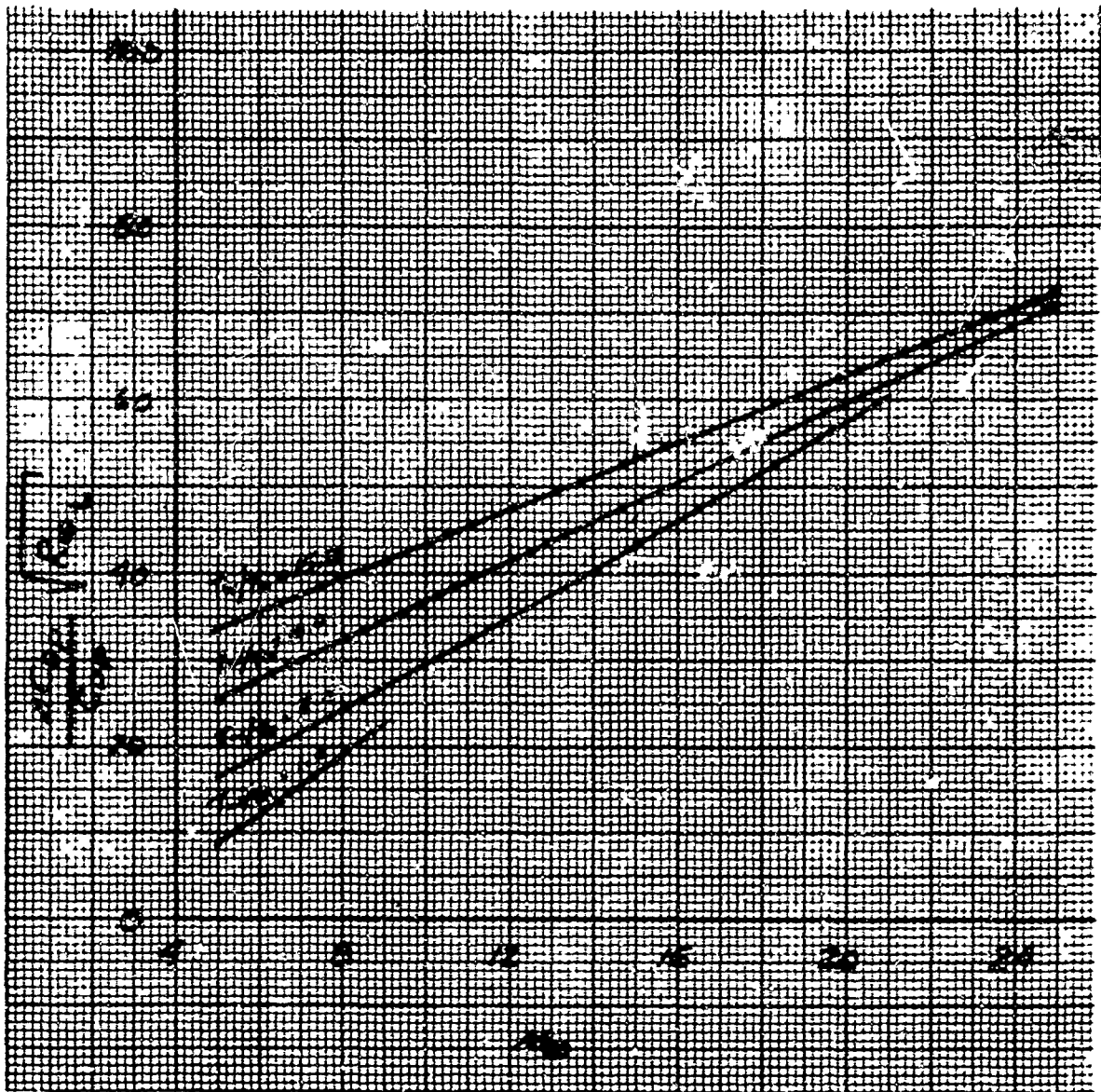


Figure 20 INDUCED PRESSURE DRAG 8° SHARP CONE, LAMINAR FLOW

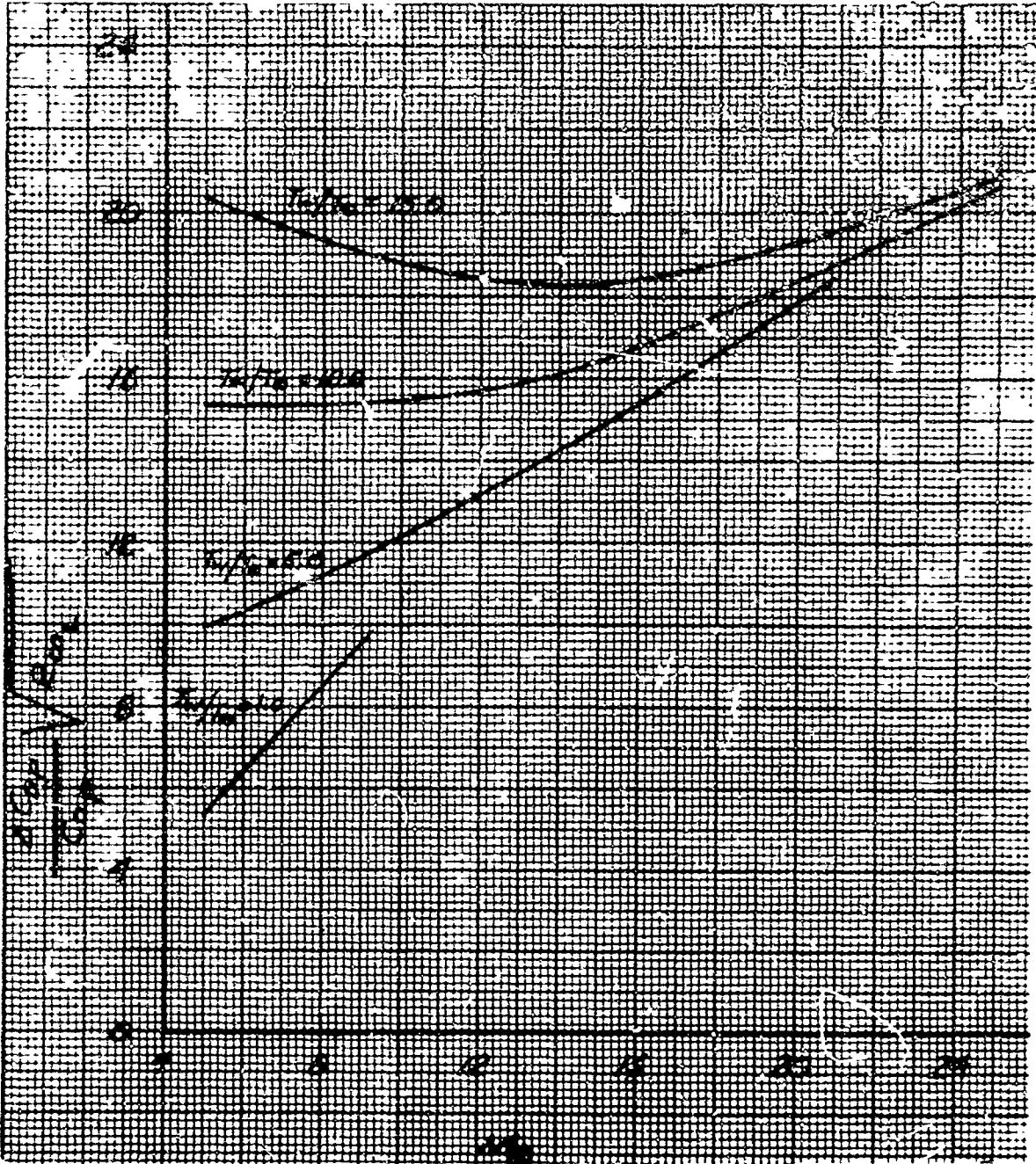


Figure 21 INDUCED PRESSURE DRAG 15° SHARP CONE, LAMINAR FLOW

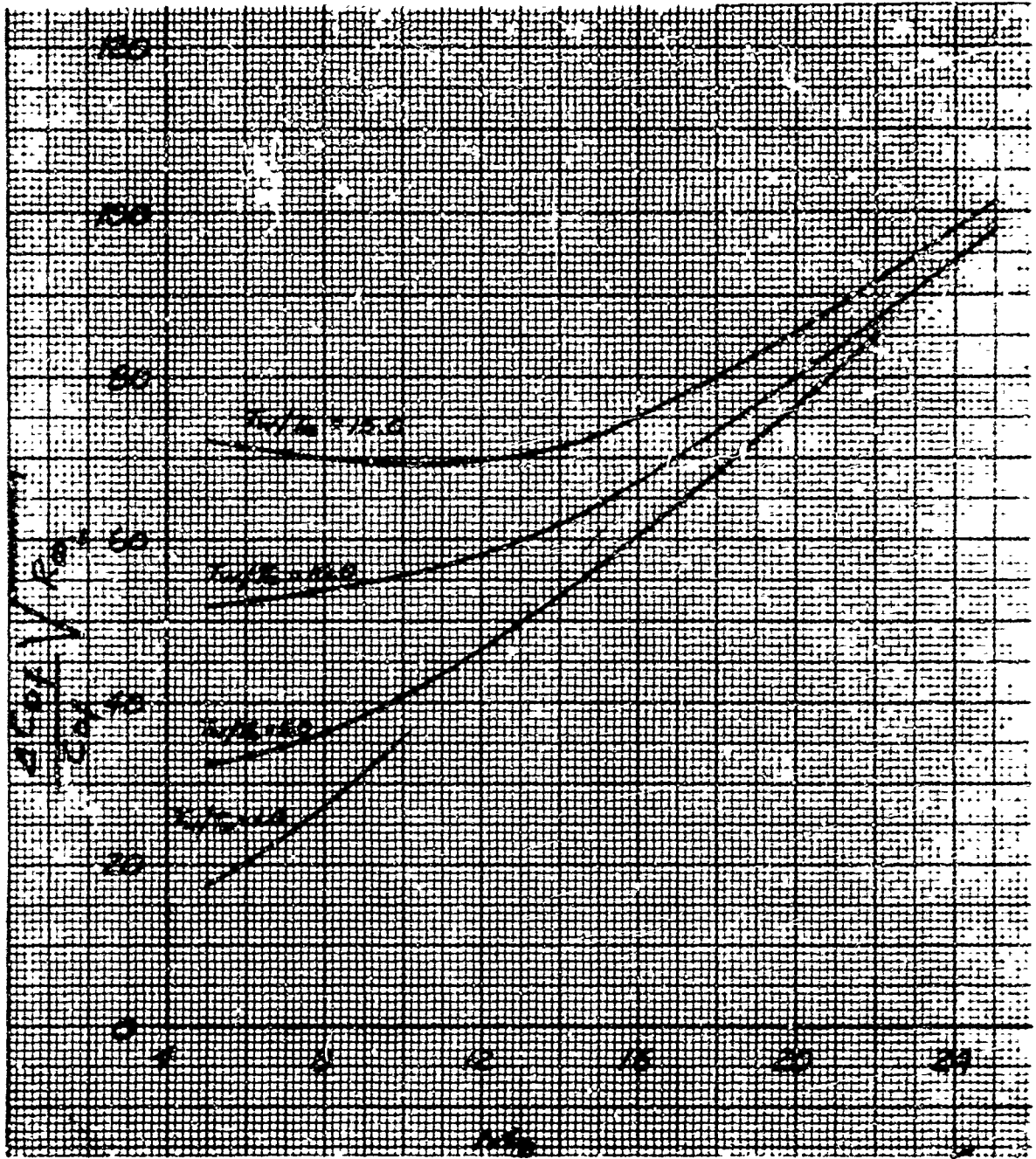
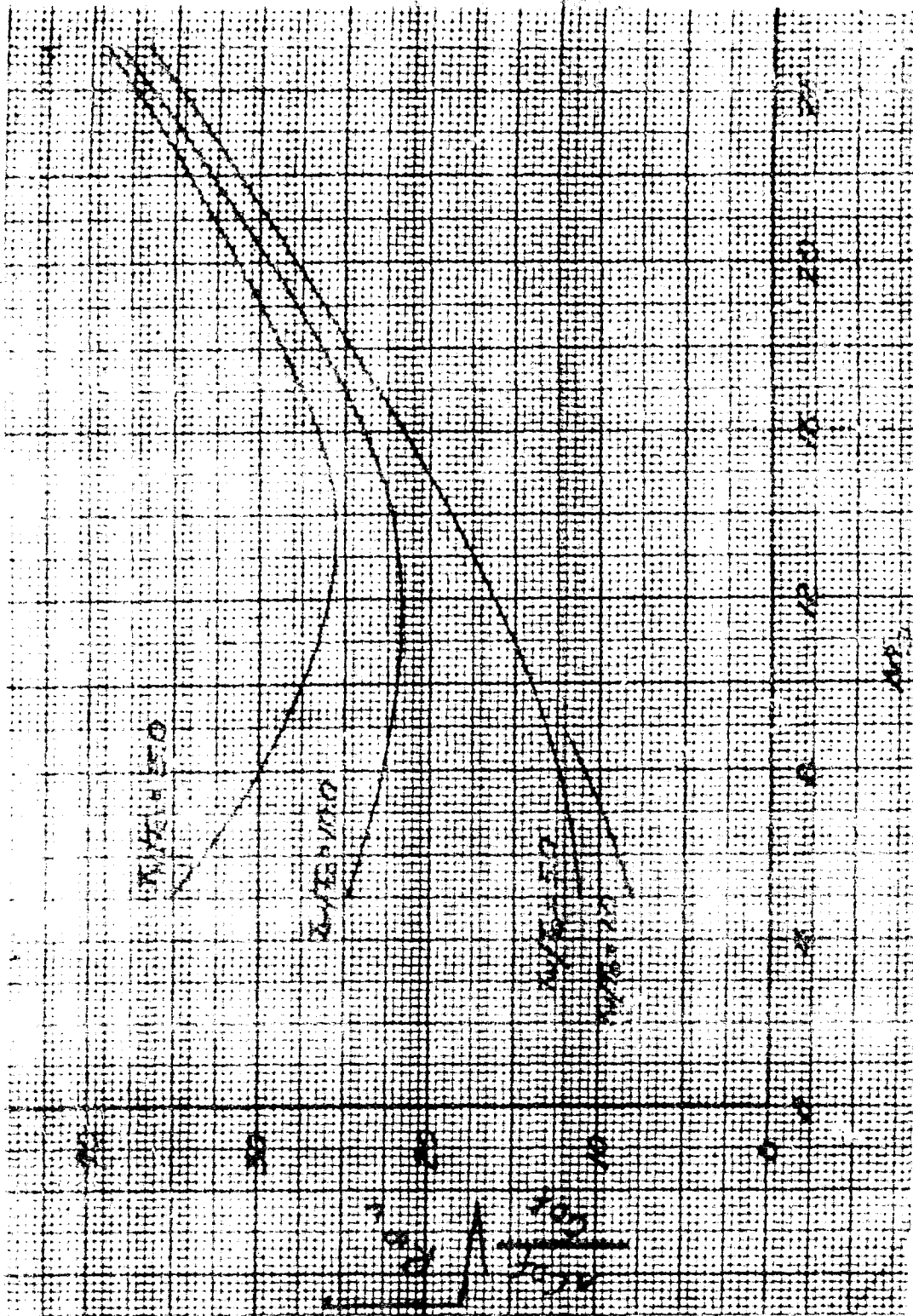


Figure 22 INDUCED SKIN FRICTION DRAG, 8° SHARP CONE, LAMINAR FLOW



In this approach the major assumptions employed are:

- a. The surface pressure ratio for the non-interaction case (p_e/p_∞) is the same as for the corresponding sharp cone between the limits, $l \leq x \leq L$.
- b. The assumed constant values of temperature and local Mach number are to be evaluated at the end of the cone ($x=L$). This assumption was made in reference 33 and was found to yield satisfactory results.

In order to compute the local Mach number at the edge of the boundary layer at $x=L$, a linear distribution is assumed between the conical shock value and the value at $x=l$, which is approximately equal to 2.0. The problem now reduces to determining where conical flow is reached.

If conical flow conditions are attained on the body, then $(M_e)_L = (M_e)_{\text{cone}}$.

If conical flow is not attained on the body, then $(M_e)_L < (M_e)_{\text{cone}}$ in accordance with the assumed linear distribution.

Employing the results of reference 25, the distance required to attain conical flow on a blunt cone in laminar flow is,

$$x_c = \left(\frac{R_N}{R_B} L \sin \theta \right)^{1.33} \left[\frac{(\cot \theta_s + 1.005)^2 (Re)^{0.5}}{8.77 \left(1 - \frac{0.75}{\rho_s/\rho_\infty - 1} \right)^2 (\sin \theta) \left(3.5 - 0.24 \frac{T_w/T_\infty}{T_e/T_\infty} \right) \left(\frac{\rho_e u_e}{\rho_\infty u_\infty} \right)} \right]^{2/3}$$

where

$$\theta_s = \arcsin \left[\sin \theta + \frac{0.6}{M_\infty} \right] \quad (\text{From Reference 21})$$

$$Re = R_\infty \left(\frac{p_e}{p_\infty} \right) \left(\frac{u_e}{u_\infty} \right) \left(\frac{T_e}{T_\infty} \right)^{-1.6} \quad (\text{assuming } \mu \sim T^{0.6})$$

$$\frac{\rho_e u_e}{\rho_\infty u_\infty} = \left(\frac{p_e}{p_\infty} \right) \left(\frac{T_e}{T_\infty} \right)^{-1} \left(\frac{u_e}{u_\infty} \right)$$

$$\rho_s/\rho_\infty = \frac{6M_\infty^2}{M_\infty^2 + 5} \quad (\text{assuming a perfect gas with } \gamma = 1.4)$$

It should be noted that the "e" conditions are evaluated for conical flow.

Employing the subscript "L" to designate conditions at $x = L$, and the subscript "C" to designate conical flow conditions. The assumed relation for M_e at $x = L$ is,

$$M_{eL} = 2 + (M_{eC} - 2) \frac{L}{r_c}$$

with the condition that if $\frac{L}{r_c} > 1$, set $\frac{L}{r_c} = 1$

To obtain T_e at $x = L$, we employ the relations,

$$\left(\frac{u_{eL}}{u_{eC}}\right)^2 = \left(\frac{M_{eL}}{M_{eC}}\right)^2 \left(\frac{T_{eL}}{T_{eC}}\right)$$

and

$$\left(\frac{u_{eL}}{u_{eC}}\right)^2 = \frac{h_s - h_{eL}}{h_s - h_{eC}}$$

Solving these relations simultaneously and assuming that $h_{eL} = h_{eC} \left(\frac{T_{eL}}{T_{eC}}\right)$ we obtain,

$$\frac{T_{eL}}{T_{\infty}} = \frac{1}{\left(\frac{M_{eL}}{M_{eC}}\right)^2 \left(\frac{T_{\infty}}{T_{eC}}\right) + \frac{h_{\infty}}{h_s} \left[1 - \left(\frac{M_{eL}}{M_{eC}}\right)^2\right]}$$

where,

$$\frac{h_s}{h_{\infty}} = 1 + 0.2 M_{\infty}^2 \quad \text{for } \gamma = 1.4$$

The flow properties at $x = L$ computed in the above manner are then used in the previously derived equations for induced pressure drag, pressure induced skin-friction drag, and transverse curvature induced skin-friction drag.

E. Angle of Attack Effects

The effect of angle of attack is to increase the induced drag on the leeward side and decrease the induced drag on the windward side. Since there are no rigorous solutions available for handling this problem, the approximate method discussed in section III will be employed. This method assumes

that the zero angle of attack solutions are applicable when the flow properties at the edge of the boundary layer are computed using tangent cone theory for the windward, leeward, and side meridians. The "effective" flow properties are then obtained by averaging the properties of the four meridians.

Therefore, the relations given in section III for $\frac{u_e}{u_\infty}$, $\frac{p_e}{p_\infty}$, and $\frac{T_e}{T_\infty}$ will be utilized in the induced drag equations.

F. Mass Addition Effects

The effect of mass addition is to increase all the induced drag contributions as a result of a thickening of the boundary layer. For the case of teflon ablation on an eight degree cone in high altitude laminar flow, the results of reference 34 show that the induced pressures due to viscous interaction with blowing may be quite significant.

No similar calculations have been made during this drag investigation, since the effects of mass addition were not to be considered in this study. However, the procedures followed in pursuing induced drag calculations with mass addition are as follows:

a. Employing the non-interacting flow properties for the first interaction, compute the laminar boundary layer displacement thickness derivative $\left(\frac{d\delta^*}{dx}\right)$ and the ratio of the injected mass flow to external mass flow $\left(\frac{\rho_w v_w}{\rho_e u_e}\right)$. This is obtained using laminar similarity theory (Program 1475) (reference 29), in conjunction with the previously determined thermodynamic and transport properties of the injected gas.

b. Employing the solution derived in reference 35, the new effective cone angle for the calculation of induced external flow properties is,

$$\theta_{\text{eff}} = \theta_{\text{orig}} + \frac{d\delta^*}{dx} + \frac{\rho_w v_w}{\rho_e u_e}$$

c. Employing the new external flow properties for the second iteration, recompute the boundary layer parameters, the new effective cone angle, and the corresponding induced external flow properties. This procedure converges after a relatively few iterations.

The final requirement would be to correlate the results of the solutions into closed form expressions. Since this task has not yet been undertaken, it is not obvious what correlation parameters would be employed for this purpose.

V. ERROR ANALYSIS

A. Accuracy Limits

Sections II, III and IV discuss the various assumptions and approximations employed in the development of the equations for the components of C_D . This section compares the values of total C_D predicted by these equations with wind tunnel and ballistic range data. In addition, a comparison of predicted C_D with the one set of flight data available (containing accelerometer and pressure measurements) is made.

The accuracy limits for total C_D predictions are 30 percent at 200,000 feet and 10 percent below 100,000 feet. A linear interpolation is made between these two altitudes. As will be shown below, these accuracy limits have been met.

B. Data Sources

A literature search was conducted at three libraries; Avco RAD, Massachusetts Institute of Technology and the Redstone Scientific Information Center. A number of reports were evaluated as to their applicability to this investigation. Those not used are listed in the bibliography with a note indicating the reason. Those used are references 36 through 41.

C. Typical Drag Coefficient Data

Typical wind tunnel test data are presented along with the predicted values (solid lines) in figures 24 through 27. The first three curves show C_D versus α for several Mach numbers, cone angles and bluntness ratios. The predicted curves agree well with the data except at the larger angles of attack where they tend to fall below the measured points. This deviation is greatest for the blunter cones, figure 26.

Figure 27 shows C_D versus Reynolds number for a cone at zero angle of attack. At $R_\infty \sim 10^7$ there appears to be a jump in the experimental values of C_D which was attributed by the investigators (reference 38) to be a transition effect. The separate laminar and turbulent curves shown in this range are drawn through the values predicted for each ballistic range data point. These curves indicate that some of these test conditions might have been partially turbulent.

Figure 27 also shows a trend of increasing C_D with Mach number in both the predicted curves and experimental data. This trend is due to the increase in skin-friction drag and induced drag as the Mach number is increased. To investigate the differences between theory and experiment, the ratio of predicted to experimental C_D versus Mach number is plotted in figure 28. Here it is seen as in figure 27 that the predicted values are somewhat less

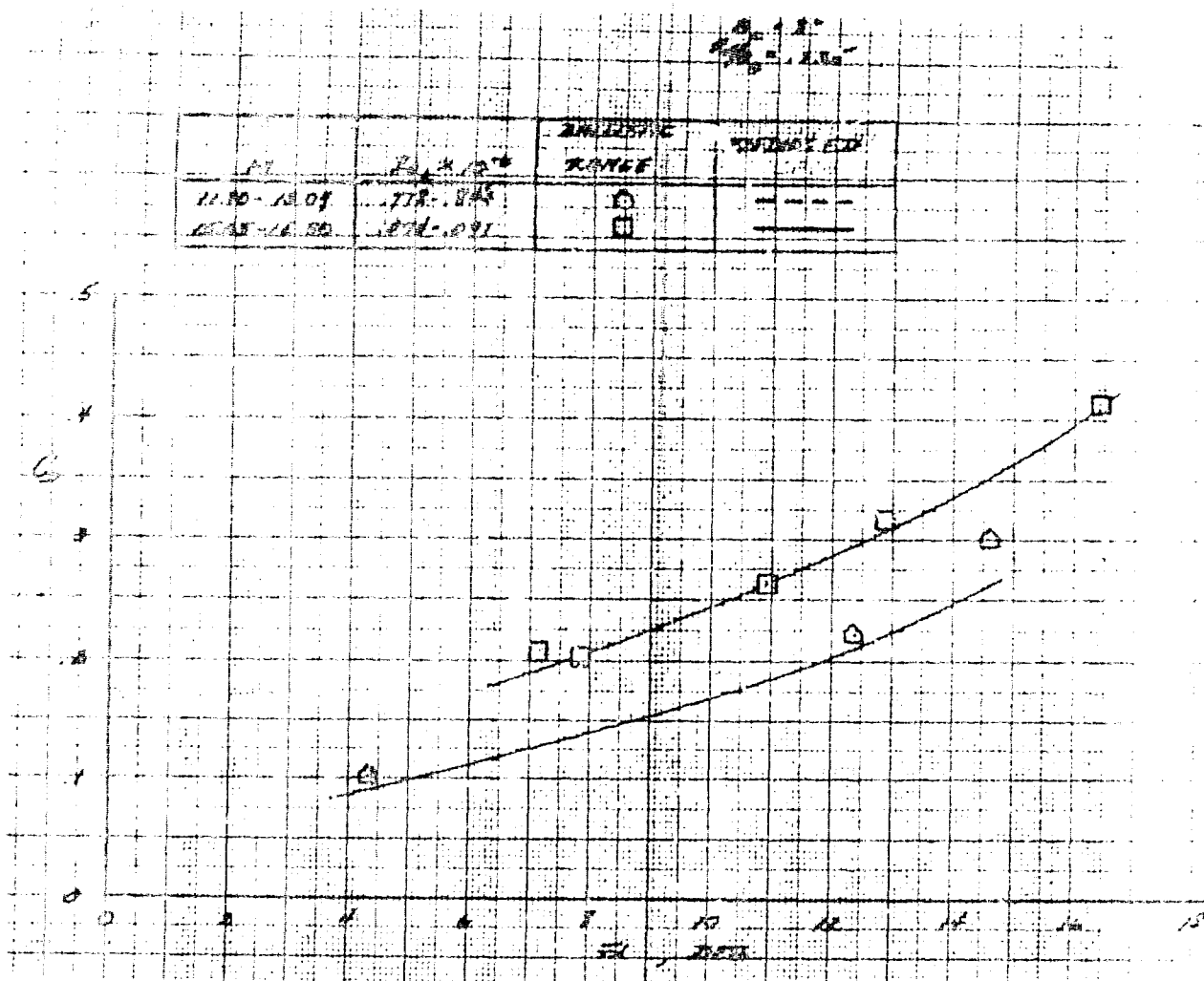


Figure 24 DRAG COEFFICIENT AS A FUNCTION OF ANGLE OF ATTACK

Best Available Copy

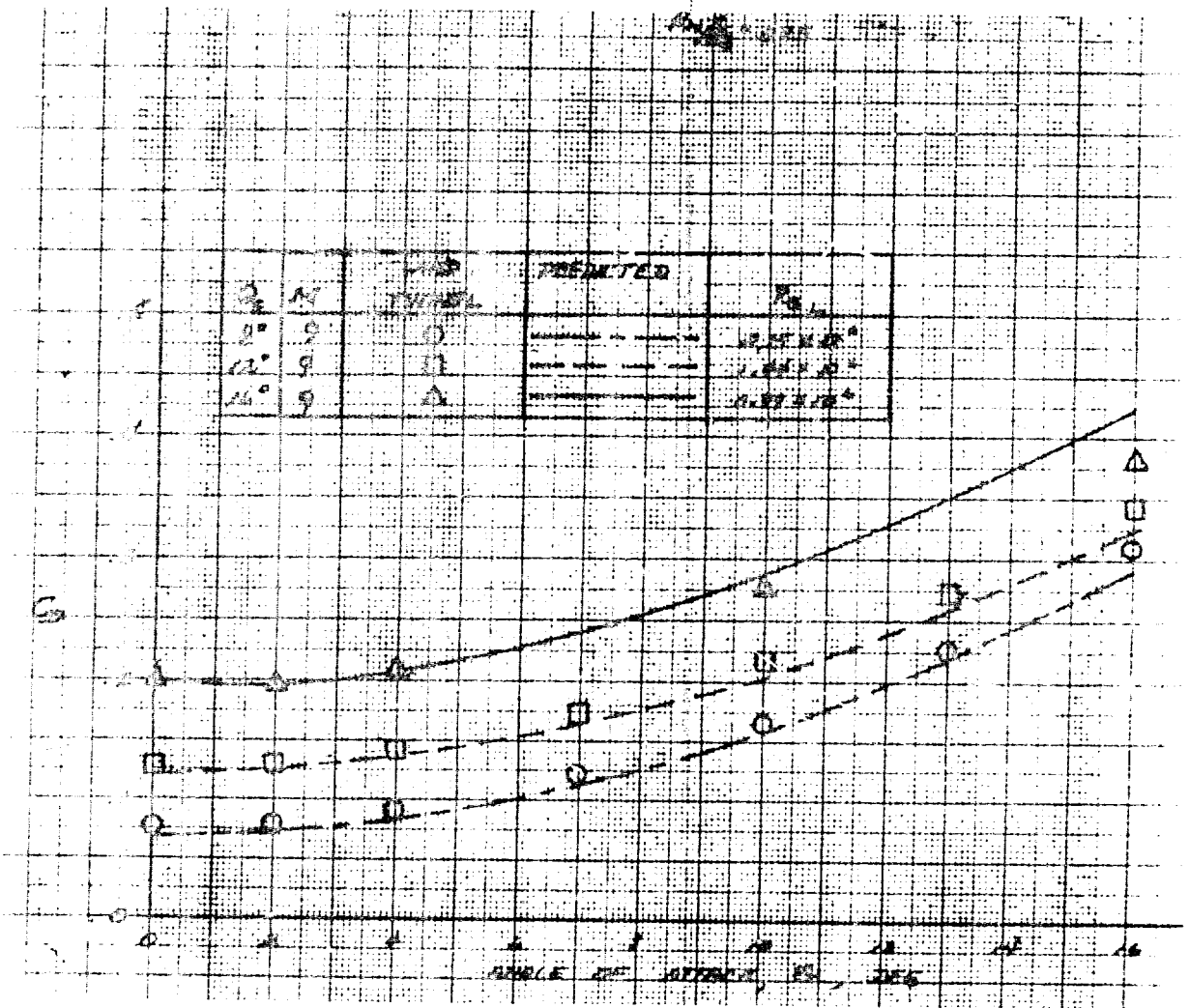


Figure 25 DRAG COEFFICIENT AS A FUNCTION OF ANGLE OF ATTACK

Best Available Copy

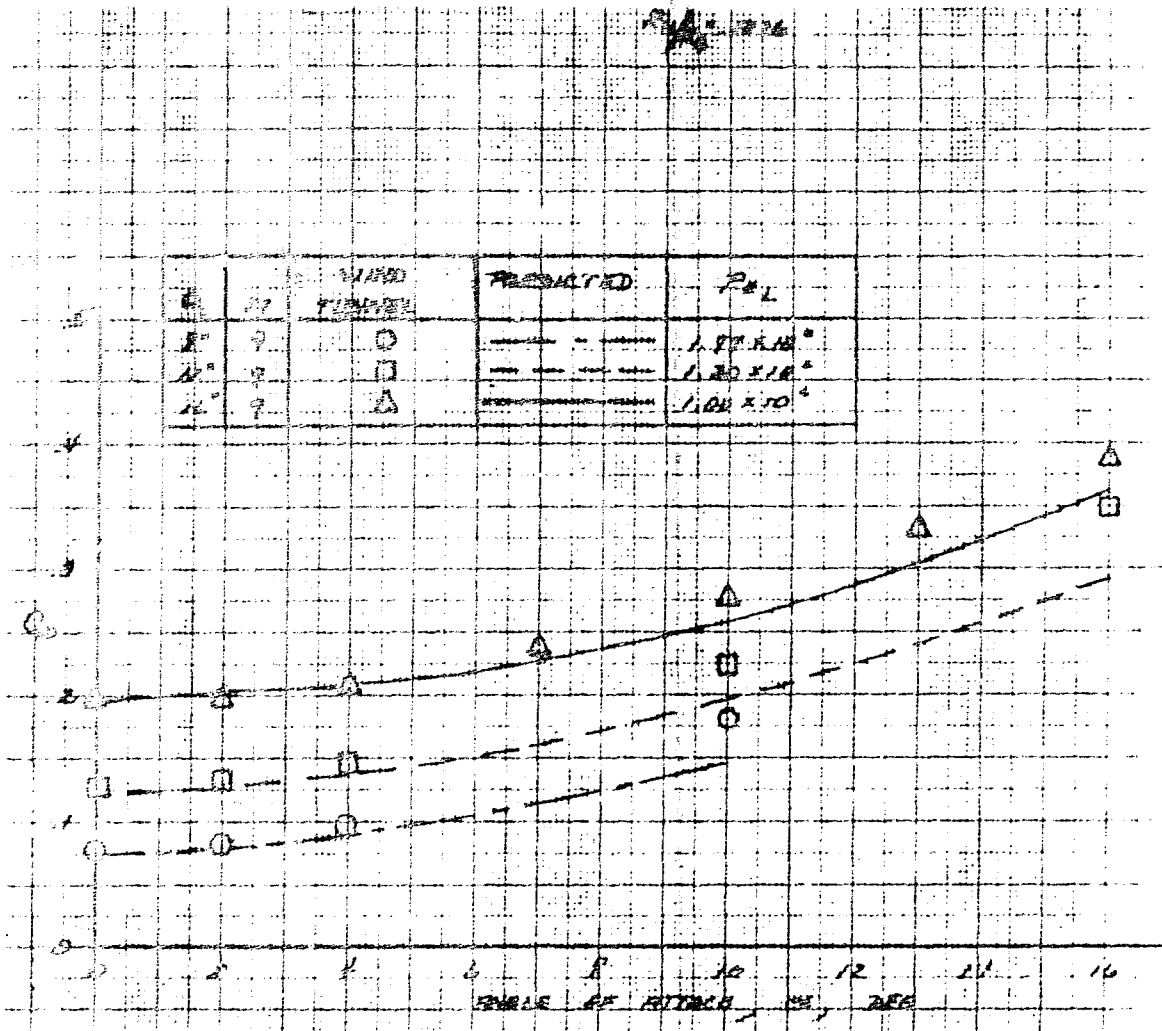


Figure 26 DRAG COEFFICIENT AS A FUNCTION OF ANGLE OF ATTACK

Best Available Copy

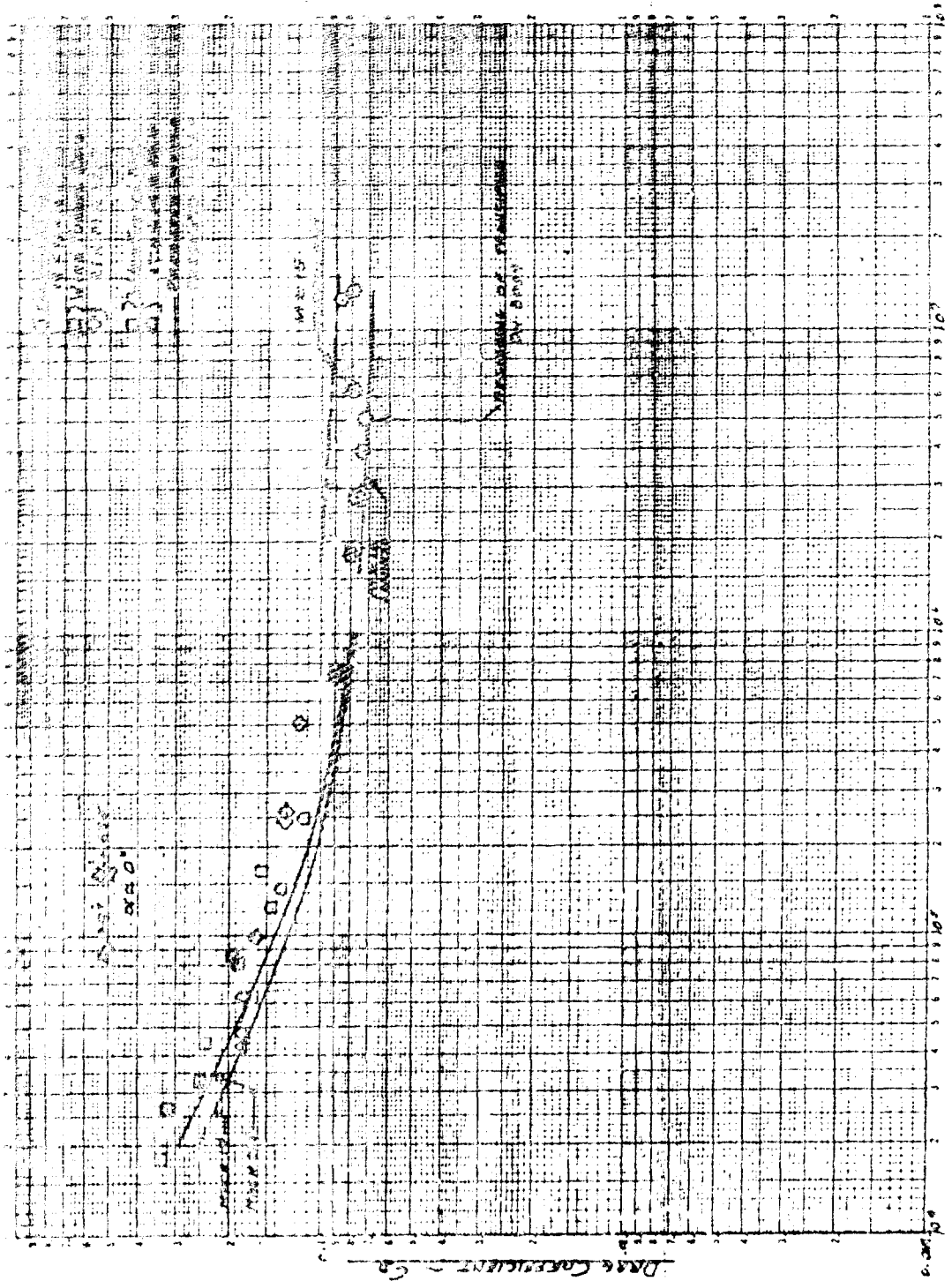


Figure 27 EFFECT OF REYNOLDS NUMBER ON DRAG COEFFICIENT

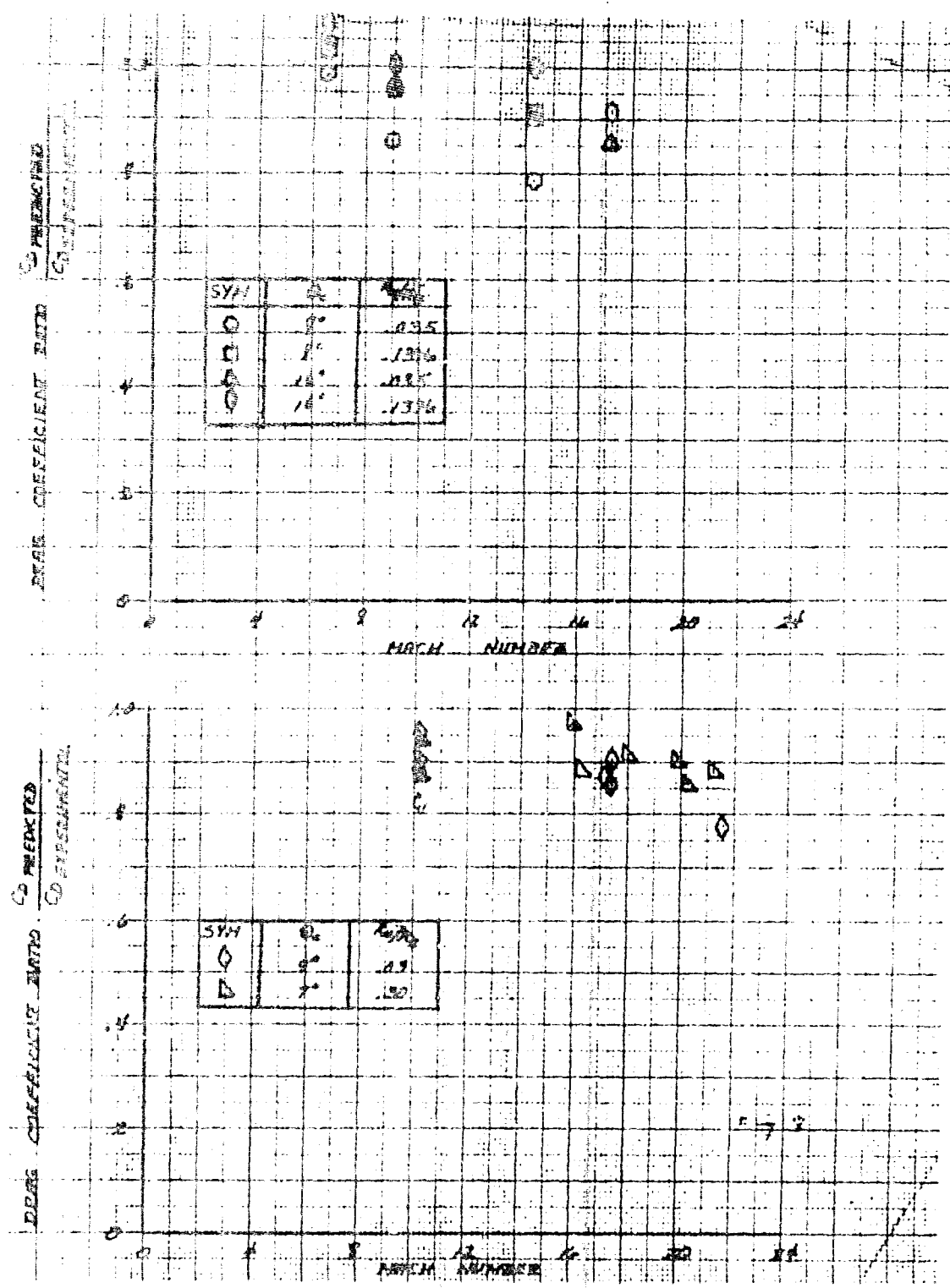


Figure 28 DRAG COEFFICIENT RATIO AS A FUNCTION OF MACH NUMBER

than the experimental values. No curve was drawn through these data because of the scatter. It may be that factors other than Mach number play a part in producing the variation shown, since the wall temperature, Reynolds number, nose bluntness ratio and cone angle are all varying.

Figure 29 shows a similar ratio versus cone angle. Here a correction trend is indicated but no line is drawn due to the number of parameters involved and the data scatter.

D. Error Evaluation Based on Ground Test Data

To assess the reliability of the methods employed for evaluating drag coefficients, calculations have been made for every experimental data point used in this investigation. The results are presented in table II, which includes the measured total drag, the ratio of predicted to experimental drag and the predicted values for each drag component.

The last column shows the minimum effective altitude of the data. It is required to compute this factor to assess whether the results are within the required accuracy limits.

With a simple manipulation the expression

$$\frac{R_{\infty} L}{M_{\infty}} = \left[\frac{\rho a}{\mu} \right]_{\infty} L \quad \text{can be}$$

derived. The bracketed expression (containing density, sound speed, and viscosity of air) is altitude dependent and decreases with increasing altitude. Fixing the left side of the equation from ground test parameters, an infinite number of combinations of altitude and length will satisfy the equation. The larger the length chosen the higher the effective altitude. It is clear that with a length range of 1 to 12 feet an altitude band of over 50,000 feet could be assigned for each data point. To assess the accuracy, however, the smallest length, 1 foot, was chosen to establish the applicable minimum effective altitude, hence the most stringent possible accuracy requirements.

Figure 30. presents the conversion chart used to establish the minimum altitude for each data point. The drag coefficient ratio is then plotted versus this altitude along with the allowable error band in figure 31. It is seen that close to 90 percent of the points fall within the allowable band. It is considered that this verifies the accuracy of the analytical expressions. There does appear to be a trend in this data, as in the previous curves, showing that the predicted values are somewhat less than the experimental values. Additional analyses are required to determine the reasons for this apparent trend and whether adjustments to the theory are warranted.

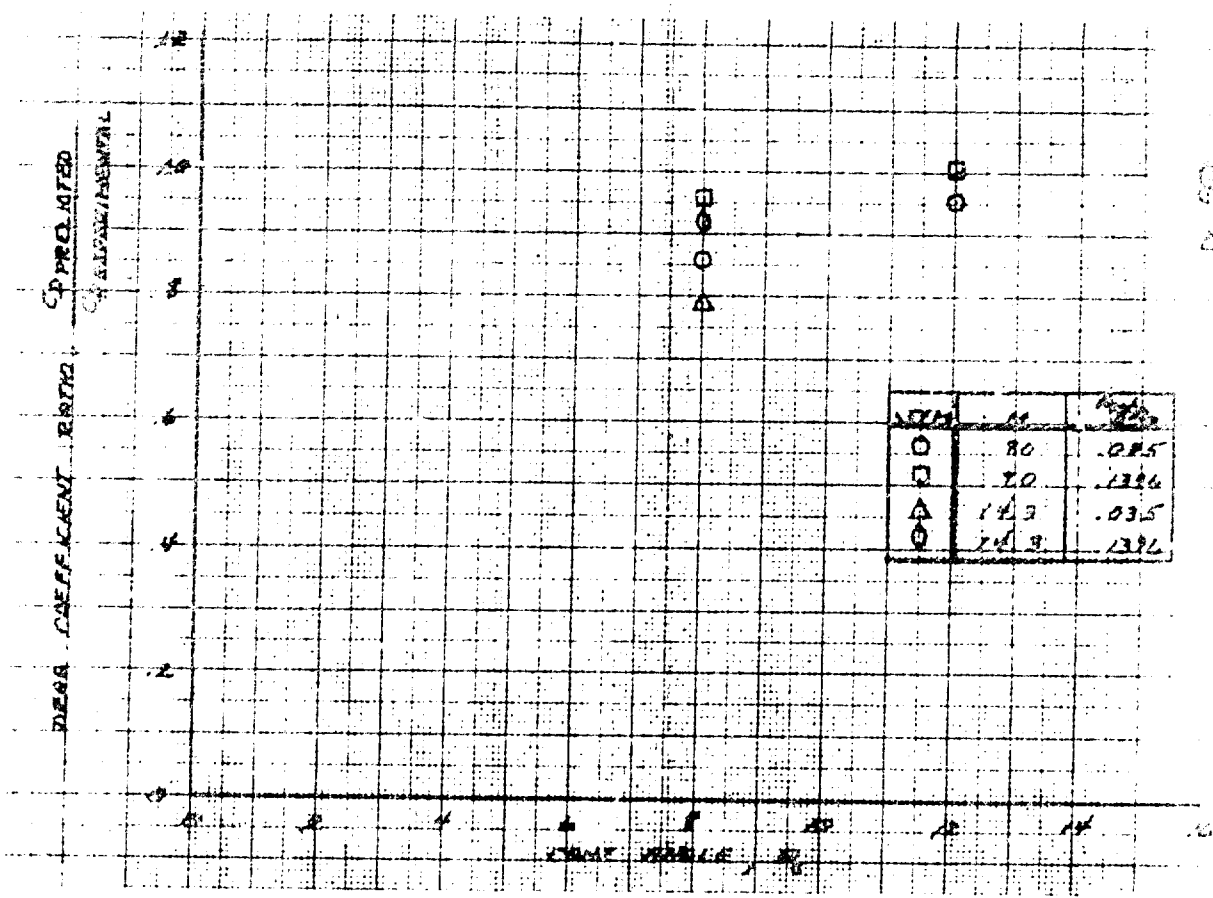
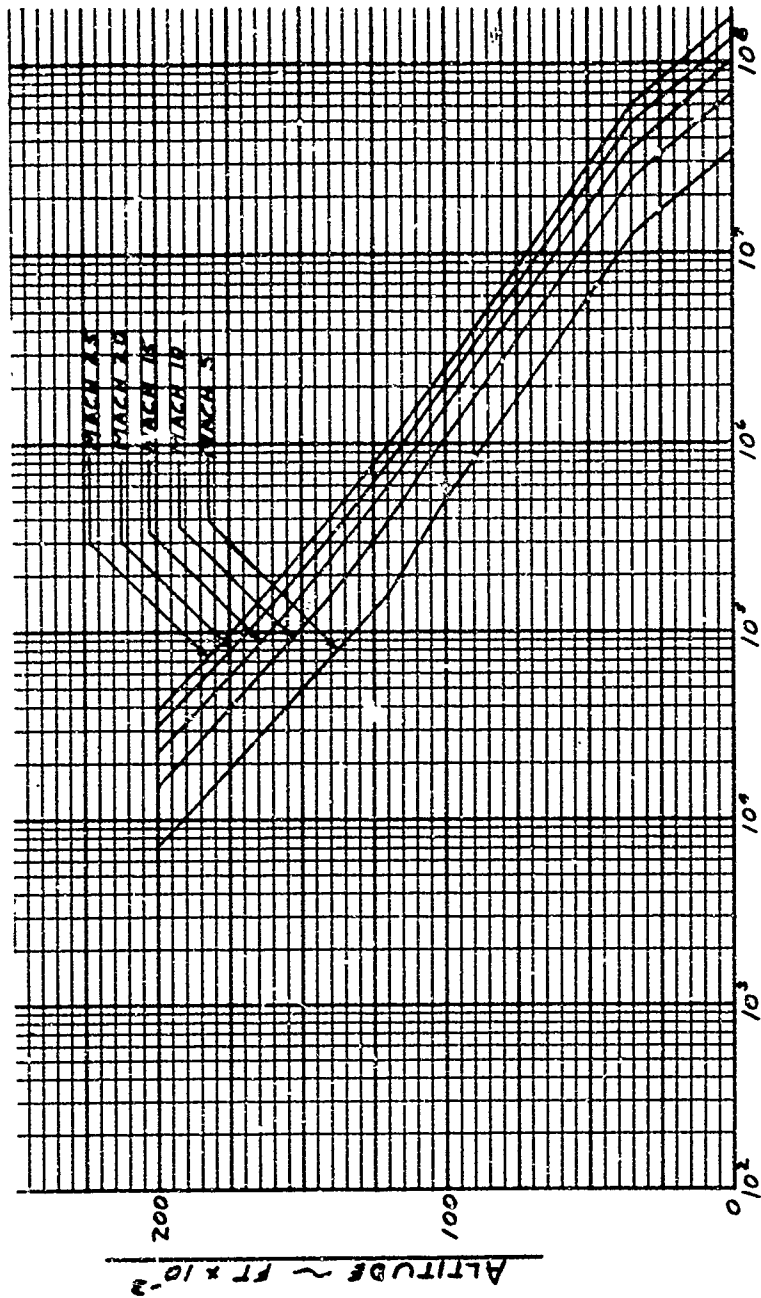


Figure 29 DRAG COEFFICIENT RATIO AS A FUNCTION OF CONE ANGLE



REYNOLDS NUMBER

Figure 30 ALTITUDE AS A FUNCTION OF REYNOLDS NUMBER FOR VARIOUS MACH NUMBERS -- BODY LENGTH 1 FOOT

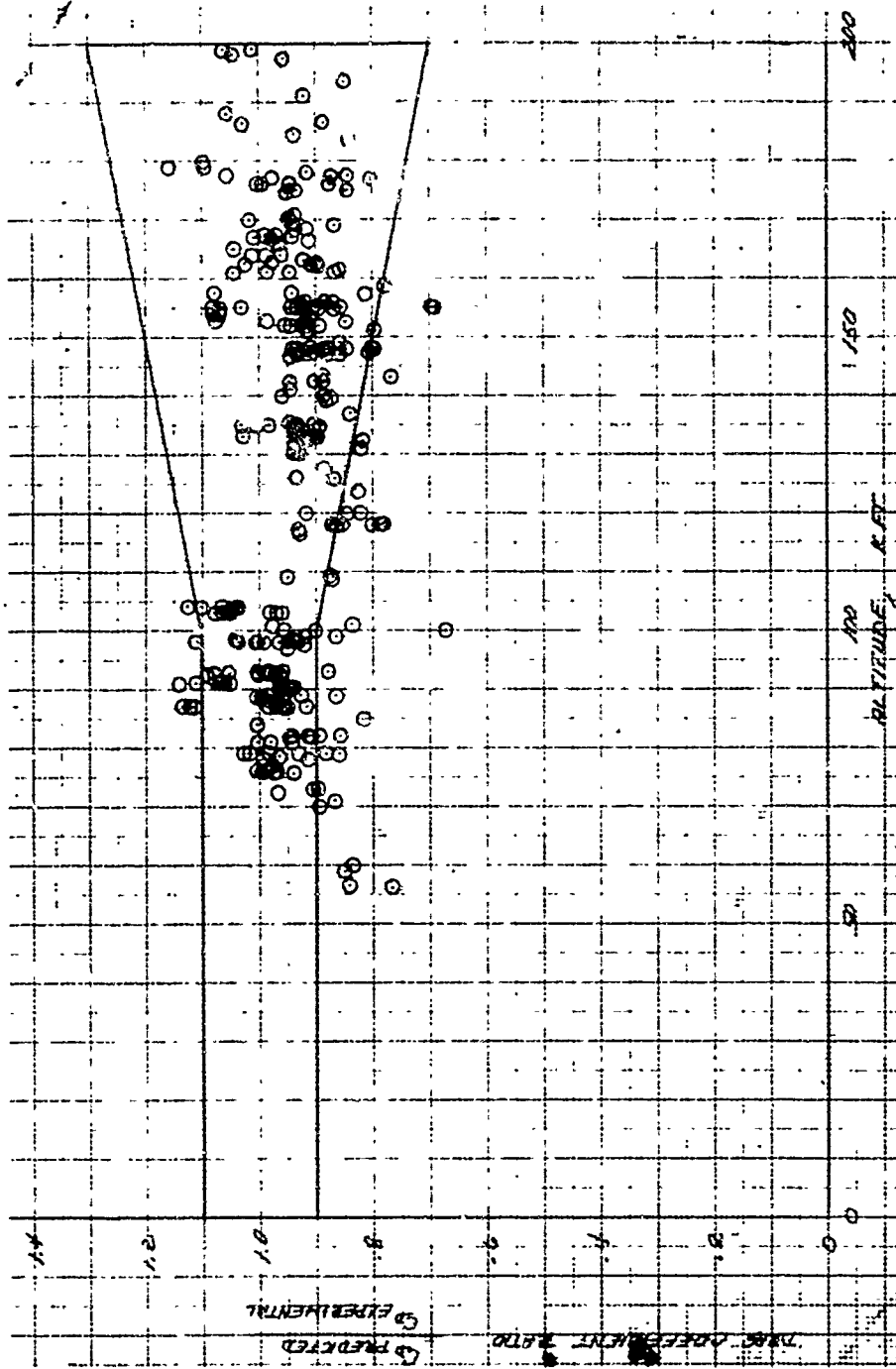


Figure 31 DRAG COEFFICIENT RATIO AS A FUNCTION OF EQUIVALENT MINIMUM ALTITUDE

TABLE II TABULATED DRAG DATA AND RATIOS

TABULATED DRAG DATA AND RATIOS

θ	λ	M_0	R_{OL}	T_w/T_f	T_f	α	C_D EXP.	$(C_D)_{LAM.}$
CONE ANGLE	BLUNTNES RATIO	MACH NUMBER	REYNOLDS NUMBER	WALL TEMPERATURE RATIO	TOTAL TEMPERATURE θ_R	ANGLE OF ATTACK	EXPERIMENTAL DRAG COEFFICIENT	PREDICTED LAMINAR DRAG COEFFICIENT
9.0	0.035	6.5	1,160,000	0.70	1560	0	0.090	0.0864
						2	0.092	0.09037
						4	0.107	0.10179
						7	0.138	0.13232
						10	0.187	0.17878
			↓			13	0.248	0.24099
			1,910,000			0	0.095	0.08383
						2	0.097	0.08782
						4	0.100	0.09916
						7	0.130	0.12947
						10	0.180	0.17564
		↓	↓			13	0.244	0.23753
		9.0	2,150,000			0	0.080	0.06870
						2	0.081	0.07257
						4	0.091	0.08357
						7	0.124	0.11292
						10	0.166	0.15754
						13	0.229	0.21723
		↓	↓	↓	↓	16	0.310	0.29192
		14.3	628,000	0.21	2460	0	0.090	0.07097
						2.5	0.099	0.07720
						4.2	0.110	0.08799
						6.0	0.134	0.10498
						6.2	0.134	0.10721
						10.4	0.197	0.16986
						14.1	0.292	0.24918
↓	↓	↓	↓	↓	↓	20.0	0.486	0.42167

NAD 6-662
4-66

16 COLUMN COMPUTING SHEET

PROBLEM

TABLE II (Cont'd)

$\theta_{cone} = 8.0^\circ, 12.0^\circ, 16.0^\circ$

	$C_{D EXP.}$	$(C_D)_{LAM.}$	C_D RATIO	$(C_{Df})_{LAM.}$	C_{DP}	C_{DB}	C_{DI}	$Z_{MIN.}$
EXPERIMENTAL DRAG COEFFICIENT	PREDICTED LAMINAR DRAG COEFFICIENT	LAMINAR $C_{D PRED. LAMINAR CO. EXPERIMENTAL}$	PREDICTED LAMINAR DRAG COEFFICIENT	PREDICTED PRESSURE DRAG COEFFICIENT	PREDICTED BASE DRAG COEFFICIENT	PREDICTED LAMINAR INDUCED DRAG COEFFICIENT	MINIMUM EQUIVALENT ALTITUDE	
0.095	0.09526	1.003	0.00926	0.05427	0.03076	0.00098	89,000	
0.100	0.09955	0.995	0.00932	0.05845	0.03076	0.00102		
0.110	0.10832	0.985	0.00949	0.06695	0.03076	0.00112		
0.143	0.13271	0.928	0.00995	0.09065	0.03076	0.00135		
0.197	0.17053	0.866	0.01061	0.12748	0.03076	0.00169		
0.256	0.22159	0.866	0.01130	0.17744	0.03076	0.00210	▼	
0.090	0.09263	1.029	0.00693	0.05427	0.03076	0.00066	79,000	
0.095	0.09689	1.020	0.00698	0.05845	0.03076	0.00070		
0.107	0.10558	0.987	0.00711	0.06695	0.03076	0.00076		
0.139	0.12980	0.934	0.00746	0.09065	0.03076	0.00094		
0.190	0.16736	0.881	0.00795	0.12748	0.03076	0.00118		
0.254	0.21813	0.859	0.00847	0.17744	0.03076	0.00147	▼	
0.079	0.07565	0.958	0.00750	0.05043	0.01679	1.00094	87,000	
0.083	0.07965	0.960	0.00756	0.05432	0.01679	0.00098		
0.096	0.08783	0.915	0.00775	0.06222	0.01679	0.00107		
0.180	0.14578	0.810	0.00891	0.11846	0.01679	0.00162	▼	
0.084	0.07669	0.913	0.01933	0.04823	0.00587	0.00325	120,000	
0.096	0.08133	0.847	0.01959	0.05247	0.00587	0.00340		
0.110	0.09031	0.821	0.02024	0.06054	0.00587	0.00365		
0.218	0.15951	0.732	0.02442	0.12399	0.00587	0.00523		
0.307	0.22365	0.729	0.02711	0.18426	0.00587	0.00641		
0.488	0.35181	0.721	0.03096	0.30667	0.00587	0.00831	▼	

16 COLUMN COMPUTING SHEET

COMPUTER

2

TABLE II (Cont'd)

$\theta_{cone} = 8.0^\circ, 12.0^\circ, 16.0^\circ$

CD EXP.	(CD) LAM	CD RATIO	(CD) LAM	CDP	CDB	CDI	Z MIN.
EXPERIMENTAL DRAG DEFICIENT	PREDICTED LAMINAR DRAG COEFFICIENT	LAMINAR CD RATIO CONVENTIONAL	PREDICTED LAMINAR SKIN FRICTION DRAG COEFFICIENT	PREDICTED PRESSURE DRAG COEFFICIENT	PREDICTED BASE DRAG COEFFICIENT	PREDICTED LAMINAR INDUCED DRAG COEFFICIENT	MINIMUM EQUIVALENT ALTITUDE
0.125	0.13912	1.113	0.00850	0.09712	0.03262	0.00088	87,000
0.127	0.14446	1.137	0.00895	0.10194	0.03262	0.00096	↓
0.139	0.15561	1.119	0.00901	0.11292	0.03262	0.00104	↓
0.128	0.12181	0.952	0.00765	0.09424	0.01780	0.00211	90,000
0.131	0.12659	0.966	0.00769	0.09892	0.01780	0.00219	
0.143	0.13751	0.952	0.00778	0.10957	0.01780	0.00236	
0.174	0.16459	0.946	0.00804	0.13602	0.01780	0.00274	
0.217	0.20442	0.942	0.00840	0.17501	0.01780	0.00321	
0.273	0.25695	0.941	0.00885	0.22657	0.01780	0.00373	
0.341	0.32207	0.944	0.00932	0.29067	0.01780	0.00429	↓
0.150	0.13954	0.930	0.03453	0.09279	0.00401	0.00821	147,000
0.170	0.15603	0.918	0.03522	0.10788	0.00401	0.00891	↓
0.224	0.19687	0.879	0.03717	0.14535	0.00401	0.01034	↓
0.280	0.26092	0.932	0.04005	0.20478	0.00401	0.01207	↓
0.566	0.45576	0.805	0.04632	0.38958	0.00401	0.01585	↓

COLUMN COMPUTING SHEET

COMPUTER

2

TABLE II (Cont'd)

$\theta_{\text{cone}} = 8.0^\circ, 12.0^\circ, 16.0^\circ$

	$C_{D \text{ EXP.}}$	$(C_D)_{\text{LAM.}}$	$C_D \text{ RATIO}$	$(C_{DF})_{\text{LAM.}}$	C_{SP}	C_{-B}	C_{DI}	$Z_{\text{MIN.}}$
ANGLE OF STACK (DEGREES)	EXPERIMENTAL DRAG COEFFICIENT	PREDICTED LAMINAR DRAG COEFFICIENT	LAMINAR C_D PRED. LAMINAR C_D EXPERIMENTAL	PREDICTED LAMINAR SKIN FRICTION DRAG COEFFICIENT	PREDICTED PRESSURE DRAG COEFFICIENT	PREDICT BASE DRAG COEFFICIENT	PREDICTED LAMINAR INDUCED DRAG COEFFICIENT	MINIMUM EQUIVALENT ALTITUDE
0	0.127	0.12732	1.003	0.00812	0.09993	0.01780	0.00147	93,000
1	0.132	0.12931	0.980	0.00815	0.10186	0.01780	0.00149	↓
7	0.146	0.13999	0.959	0.00826	0.11233	0.01780	0.00161	↓
5	0.225	0.19755	0.878	0.00891	0.16871	0.01780	0.00214	↓
3	0.349	0.29303	0.840	0.00988	0.26252	0.01780	0.00282	↓
7	0.155	0.14617	0.943	0.03682	0.19724	0.00401	0.00810	148,000
0	0.163	0.14820	0.910	0.03701	0.09912	0.00401	0.00815	↓
17	0.171	0.15947	0.933	0.03756	0.10931	0.00401	0.00859	↓
2	0.197	0.17512	0.889	0.03895	0.12355	0.00401	0.00911	↓
6	0.244	0.19516	0.80	0.03964	0.14183	0.00401	0.00968	↓
3	0.259	0.21953	0.845	0.04108	0.16416	0.00401	0.01028	↓
8	0.373	0.29878	0.801	0.04530	0.23771	0.00401	0.01176	↓
31	0.507	0.40331	0.795	0.04990	0.33655	0.00401	0.01335	↓

2

TABLE II (Cont'd)

θ	L	M	Re_L	T_w/T_f	T_f	α	C_D EXP.	(C_D) LAM.	C
CONE ANGLE (DEGREES)	BLUNTNES RATIO	MACH NUMBER	REYNOLDS NUMBER	WALL TEMPERATURE RATIO	TOTAL TEMPERATURE (°R)	ANGLE OF ATTACK (DEGREES)	EXPERIMENTAL DRAG COEFFICIENT	PREDICTED LAMINAR DRAG COEFFICIENT	L/C_D
16	0.035	6.5	587,000	0.70	1560	0	0.205	0.21295	
						2	0.207	0.21656	
						4	0.219	0.22939	
						7	0.251	0.26131	
						10	0.289	0.30892	
						13	0.336	0.37067	
			↓			16	0.398	0.44799	
			968,000			0	0.200	0.21013	
						2	0.203	0.21373	
						4	0.214	0.22651	
						7	0.242	0.25832	
						10	0.284	0.30528	
						13	0.331	0.36735	
		↓	↓		↓	16	0.390	0.44448	
		9.0	990,000		1660	0	0.200	0.19286	
						2	0.198	0.19642	
						4	0.209	0.20898	
						10	0.277	0.28638	
		↓	↓	↓	↓	16	0.381	0.42300	
		14.3	318,000	0.21	2460	0	0.218	0.19546	
						2.2	0.222	0.19999	
						4.0	0.230	0.21169	
		↓	↓	↓	↓	6.1	0.249	0.23216	
		17.2	163,000	0.10	4300	0	0.247	0.21103	
						4	0.221	0.22757	
						8	0.302	0.27369	
						12	0.368	0.34659	
↓	↓	↓	↓	↓	↓	20	0.529	0.57093	

PROBLEM

TABLE II (Cont'd)

$\theta_{\text{cone}} = 8.0^\circ, 12.0^\circ, 16.0^\circ$

EXP.	(C _D) LAM.	C _D RATIO	(C _{Df}) LAM.	C _{DP}	C _{DB}	C _{DI}	Z MIN.
EXPERIMENTAL DRAG COEFFICIENT	PREDICTED LAMINAR DRAG COEFFICIENT	LAMINAR C _D PRED LAMINAR C _D EXPERIMENT	PREDICTED LAMINAR DRAG COEFFICIENT	PREDICTED PRESSURE DRAG COEFFICIENT	PREDICTED BASE DRAG COEFFICIENT	PREDICTED LAMINAR INDUCED DRAG COEFFICIENT	MINIMUM EQUIVALENT ALTITUDE
205	0.21295	1.039	0.00944	0.16658	0.03444	0.00298	104,000
207	0.21656	1.046	0.00947	0.17013	0.03444	0.00252	
219	0.22939	1.047	0.00951	0.18276	0.03444	0.00267	
251	0.26131	1.041	0.00966	0.21421	0.03444	0.00300	
289	0.30842	1.067	0.00987	0.26065	0.03444	0.00395	
336	0.37067	1.103	0.01014	0.32210	0.03444	0.00398	
398	0.44799	1.126	0.01044	0.39855	0.03444	0.00455	↓
200	0.21013	1.051	0.00720	0.16658	0.03444	0.00190	91,000
201	0.21373	1.053	0.00721	0.17013	0.03444	0.00193	
214	0.22651	1.058	0.00726	0.18276	0.03444	0.00205	
242	0.25832	1.067	0.00737	0.21421	0.03444	0.00231	
284	0.30528	1.075	0.00753	0.26065	0.03444	0.00266	
331	0.36735	1.110	0.00773	0.32210	0.03444	0.00307	
390	0.44448	1.140	0.00797	0.39855	0.03444	0.00351	↓
200	0.19286	0.964	0.00841	0.16296	0.01880	0.00272	98,000
198	0.19642	0.992	0.00842	0.16644	0.01880	0.00276	
209	0.20898	1.00	0.00848	0.17879	0.01880	0.00292	
277	0.28638	1.034	0.00885	0.25499	0.01880	0.00375	
381	0.42300	1.110	0.00944	0.38989	0.01880	0.00487	↓
218	0.19546	0.897	0.02229	0.14126	0.00658	0.00533	133,000
222	0.19999	0.901	0.02236	0.16563	0.00658	0.00543	
230	0.21169	0.920	0.02251	0.17692	0.00658	0.00568	
249	0.23216	0.932	0.02280	0.19670	0.00658	0.00608	↓
247	0.21103	0.854	0.03692	0.16105	0.00424	0.00882	155,000
221	0.22757	1.030	0.03730	0.17767	0.00424	0.00934	
302	0.27369	0.906	0.03837	0.22045	0.00424	0.01064	
368	0.34659	0.942	0.04000	0.28999	0.00424	0.01236	
529	0.57093	1.079	0.04408	0.50643	0.00424	0.01619	↓

COLUMN COMPUTING SHEET

COMPUTER

2

TABLE II (Cont'd)

θ	λ	M	R_{00L}	T_w/T_f	T_f	α	C_D EXP.	(C_D) LAM.
CONE ANGLE (DEGREES)	BLUNTNES RATIO	MACH NUMBER	REYNOLDS NUMBER	WALL TEMPERATURE RATIO	TOTAL TEMPERATURE (OR)	ANGLE OF ATTACK (DEGREES)	EXPERIMENTAL DRAG COEFFICIENT	PREDICTED LAMINAR DRAG COEFFICIENT
16.0	0.1396	6.5	541,000	0.7	1560	0	0.205	0.21913
						2	0.211	0.22761
						4	0.221	0.23216
						10	0.289	0.28305
						13	0.343	0.32939
			Y			16	0.401	0.38960
			993,000			0	0.200	0.21608
						2	0.206	0.22453
						4	0.218	0.22906
						7	0.246	0.24745
						10	0.285	0.27974
						13	0.337	0.32592
		Y	Y			16	0.397	0.38593
		9.0	1,000,000			0	0.196	0.19662
						2	0.197	0.20485
						4	0.209	0.20927
						7	0.240	0.22719
						10	0.278	0.25864
						13	0.333	0.30360
		Y	Y	Y	Y	16	0.389	0.36202
		14.3	294,000	0.21	2460	0	0.200	0.20043
						2.4	0.203	0.20909
						4.3	0.213	0.21436
						5.7	0.226	0.22174
						6.3	0.243	0.22581
						9.9	0.289	0.26162
						14.4	0.374	0.33363
Y	Y	Y	Y	Y	Y	20.3	0.508	0.47333

PROBLEM

1

TABLE II (Cont'd)

$\theta_{cone} = 8.0^\circ, 12.0^\circ, 16.0^\circ$

EXP.	(C _D) _{LAM.}	C _D RATIO	(C _{Df}) _{LAM.}	C _{DP}	C _{DB}	C _{DI}	Z MIN.
EXPERIMENTAL DRAG COEFFICIENT	PREDICTED LAMINAR DRAG COEFFICIENT	LAMINAR C _D EXPERIMENTAL	PREDICTED LAMINAR SKIN FRICTION DRAG COEFFICIENT	PREDICTED PRESSURE DRAG COEFFICIENT	PREDICTED BASE DRAG COEFFICIENT	PREDICTED INDUCED DRAG COEFFICIENT	MINIMUM EQUIVALENT ALTITUDE
05	0.21913	1.069	0.00975	0.17283	0.03444	0.00210	103,000
11	0.22761	1.079	0.00977	0.18121	0.03444	0.00219	
21	0.23216	1.050	0.00983	0.18567	0.03444	0.00222	
89	0.28305	0.9794	0.01020	0.23580	0.03444	0.00261	
43	0.32939	0.9603	0.01048	0.28152	0.03444	0.00295	
101	0.38960	0.9716	0.01079	0.34101	0.03444	0.00335	↓
100	0.21608	1.080	0.00732	0.17283	0.03444	0.00148	92,500
26	0.22453	1.090	0.00733	0.18121	0.03444	0.00154	
18	0.22906	1.051	0.00738	0.18567	0.03444	0.00157	
46	0.24745	1.006	0.00749	0.20385	0.03444	0.00167	
85	0.27974	0.9915	0.00765	0.23580	0.03444	0.00195	
37	0.32592	0.9671	0.00786	0.28152	0.03444	0.00209	
97	0.38593	0.9721	0.00810	0.34101	0.03444	0.00238	↓
96	0.19662	1.003	0.00808	0.16779	0.01880	0.00195	98,500
27	0.20485	1.040	0.00810	0.17592	0.01880	0.00203	
29	0.20927	1.001	0.00816	0.18025	0.01880	0.00206	
10	0.22717	0.9466	0.00830	0.19790	0.01880	0.00219	
78	0.25864	0.9304	0.00851	0.22892	0.01880	0.00242	
33	0.30360	0.9117	0.00877	0.27331	0.01880	0.00272	
89	0.36202	0.9306	0.00908	0.33107	0.01880	0.00308	↓
100	0.20043	1.002	0.02347	0.16581	0.00658	0.00519	135,000
103	0.20909	1.030	0.02356	0.17358	0.00658	0.00538	
13	0.21436	1.006	0.02374	0.17860	0.00658	0.00544	
26	0.22174	0.9811	0.02394	0.18568	0.00658	0.00554	
43	0.22581	0.9293	0.02404	0.18960	0.00658	0.00560	
89	0.26162	0.9053	0.02482	0.22913	0.00658	0.00610	
74	0.33363	0.8921	0.02612	0.29395	0.00658	0.00698	
108	0.47333	0.9318	0.02804	0.43038	0.00658	0.00934	↓

COMPUTING SHEET

COMPUTER

2

TABLE II (Cont'd)

$\theta_{\text{cone}} = 8.0^\circ, 12.0^\circ, 16.0^\circ$

COEFF.	(C _D) LAM.	C _D RATIO	(C _{DF}) LAM.	C _{DP}	C _{DB}	C _{DI}	Z MIN.
EXPERIMENTAL DRAG EFFICIENT	PREDICTED LAMINAR DRAG COEFFICIENT	LAMINAR C _{DF} RATIO C _{DF} EXPERIMENTAL	PREDICTED LAMINAR SKIN FRICTION DRAG COEFFICIENT	PREDICTED PRESSURE DRAG COEFFICIENT	PREDICTED BASE DRAG COEFFICIENT	PREDICTED LAMINAR INDUCED DRAG COEFFICIENT	MINIMUM EQUIVALENT ALTITUDE
0.237	0.21730	0.9169	0.03964	0.16984	0.00424	0.00859	155,000
0.325	0.22569	0.6944	0.03974	0.17293	0.00424	0.00889	
0.247	0.23030	0.9324	0.04004	0.17708	0.00424	0.00894	
0.349	0.24110	0.6909	0.04053	0.18719	0.00424	0.00915	
0.298	0.25809	0.8659	0.04119	0.20311	0.00424	0.00950	
0.337	0.31018	0.9204	0.04294	0.25250	0.00424	0.01050	
0.457	0.48602	1.063	0.04732	0.42132	0.00424	0.01314	▼

COLUMN COMPUTING SHEET

COMPUTER

2

TABLE II (Cont'd)

TABULATED DRAG DATA AND RATIOS

θ	λ	M	Re_L	T_w/T_T	T_T	α	$C_{D EXP}$	$(C_D) LAM.$
CONE ANGLE (DEGREES)	BLUNTNES RATIO	MACH NUMBER	REYNOLDS NUMBER	WALL TEMPERATURE RATIO	TOTAL TEMPERATURE (°R)	ANGLE OF ATTACK (DEGREES)	EXPERIMENTAL DRAG COEFFICIENT	PREDICTED LAMINAR DRAG COEFFICIENT
6.34	0.03	14.7	150500	0.1	5500	0.0	0.099	0.09024
		16.2	57200				0.072	0.05929
		17.2	161000				0.109	0.09245
		17.4	338000				0.084	0.07046
		17.5	258000				0.101	0.07753
	0.30	15.9	412000				0.136	0.12608
		16.9	172000				0.185	0.14689
		17.5	109000				0.179	0.16473
		18.0	224400				0.164	0.14055
9.0	0.0	17.0	63000				0.167	0.16267
		18.0	47800				0.181	0.18581
		17.0	60300				0.181	0.16534
		17.0	42200				0.180	0.19018
	0.03	17.4	247000				0.112	0.10115
		16.1	395400				0.110	0.09016
		17.4	122400				0.143	0.12276
		17.2	143800				0.134	0.11657
		22.4	84600				0.192	0.15379
		21.0	32700				0.246	0.22429
		21.6	167000				0.154	0.11965
		22.0	87700				0.185	0.15533
		21.8	44000				0.235	0.19954
		21.4	26300				0.318	0.25268
		21.0	18300				0.336	0.30193
		10.18	246900	0.75	1900		0.121	0.09876
		10.15	149000				0.120	0.10573
		10.19	318730				0.109	0.09422
		10.19	321400				0.101	0.09410
		10.19	165300				0.111	0.10620
		10.15	166600				0.120	0.10604
		10.07	67400				0.148	0.13272
		10.04	37400				0.167	0.15765
		10.07	66800				0.148	0.13307

NAD 5-083
4-88

16 COLUMN COMPUTING SHEET

PROBLEM

TABLE II (Cont'd)

DATA AND RATIOS

AEDC-TDR-63-35

	$C_{D EXP}$	$(C_D)_{LAM.}$	C_D RATIO	$(C_{Df})_{LAM.}$	C_{DP}	C_{DB}	C_{DI}	Z_{MIN}
TEST	EXPERIMENTAL DRAG COEFFICIENT	PREDICTED LAMINAR DRAG COEFFICIENT	LAMINAR C_D PRED. LAM. C_D EXPERIMENTAL	PREDICTED LAMINAR SKIN FRICTION DRAG COEFFICIENT	PREDICTED PRESSURE DRAG COEFFICIENT	PREDICTED BASE DRAG COEFFICIENT	PREDICTED LAMINAR INDUCED DRAG COEFFICIENT	MINIMUM EQUIVALENT ALTITUDE
	0.099	0.09024	0.912	0.04496	0.02712	0.00536	0.01281	151,000
	0.072	0.05929	0.824	0.02291	0.02709	0.00425	0.00505	123,500
	0.10°	0.09245	0.848	0.04640	0.02109	0.00369	0.01528	152,500
	0.084	0.07046	0.839	0.03135	0.02709	0.00359	0.00843	137,000
	0.101	0.07753	0.767	0.03633	0.02709	0.00354	0.01058	143,000
	0.136	0.12608	0.927	0.01999	0.09665	0.00444	0.00501	130,000
	0.185	0.14689	0.794	0.03514	0.09666	0.00384	0.01124	151,000
	0.179	0.16473	0.920	0.04709	0.09668	0.00354	0.01741	163,000
	0.164	0.14055	0.857	0.03074	0.09670	0.00332	0.00979	147,000
	0.167	0.16267	0.974	0.07794	0.05437	0.00395	0.02642	177,000
	0.181	0.18581	1.029	0.09222	0.05436	0.00346	0.03577	186,500
	0.181	0.16534	0.913	0.07966	0.05437	0.00395	0.02737	178,000
	0.180	0.19018	1.057	0.09523	0.05437	0.00395	0.03664	188,000
	0.112	0.10115	0.903	0.03434	0.05432	0.00374	0.00876	142,500
	0.110	0.09016	0.820	0.02562	0.05433	0.00449	0.00572	131,000
	0.143	0.12276	0.858	0.04999	0.05432	0.00374	0.01472	161,500
	0.134	0.11657	0.870	0.04559	0.05432	0.00384	0.01283	156,000
	0.192	0.15379	0.801	0.06988	0.05434	0.00222	0.02736	177,000
	0.246	0.22429	0.912	0.11196	0.05432	0.00249	0.05351	GREATER THAN 200,000 FEET
	0.154	0.11165	0.727	0.04761	0.05433	0.00236	0.01535	158,500
	0.185	0.15533	0.840	0.07095	0.05434	0.00229	0.02776	177,500
	0.235	0.19954	0.849	0.09758	0.05433	0.00232	0.04531	193,500
	0.318	0.25268	0.795	0.12707	0.05433	0.00240	0.06888	GREATER THAN 200,000 FEET
	0.336	0.30193	0.898	0.15254	0.05433	0.00249	0.09257	↓
	0.121	0.09876	0.816	0.02317	0.05495	0.01312	0.00752	132,500
	0.120	0.10573	0.881	0.02798	0.05496	0.01321	0.00958	139,000
	0.109	0.09422	0.864	0.01995	0.05495	0.01309	0.00623	126,000
	0.101	0.09410	0.932	0.01986	0.05495	0.01309	0.00619	126,000
	0.111	0.10620	0.957	0.02836	0.05495	0.01309	0.00979	140,000
	0.120	0.10604	0.883	0.02819	0.05496	0.01321	0.00968	140,000
	0.148	0.13272	0.899	0.04558	0.05498	0.01344	0.01872	162,500
	0.167	0.15765	0.944	0.06062	0.05499	0.01352	0.02885	176,000
	0.178	0.13307	0.899	0.04580	0.05498	0.01344	0.01885	162,500

16 COLUMN COMPUTING SHEET

COMPUTER

2

TABLE II (Cont'd)

θ	λ	M	Re _{0L}	T _w /T _f	T _f	α	C _D EXP.	(C _D) _{LA}		
CONE ANGLE (DEGREES)	BLUNTNES RATIO	MACH NUMBER	REYNOLDS NUMBER	WALL TEMPERATURE RATIO	TOTAL TEMPERATURE (°R)	ANGLE OF ATTACK (DEGREES)	EXPERIMENTAL DRAG COEFFICIENT	PRED. LAMINAR DRAG COEFF.		
9.0	0.03	10.04	39100	0.75	1900	0.0	0.181	0.13		
		10.02	29800				0.208	0.17		
		9.23	818	0.20	3000		0.704	1.100		
		9.23	818				0.712	1.100		
		9.00	883				0.663	1.02		
		8.77	959				0.637	0.94		
		8.77	959				0.625	0.945		
		9.66	1529	0.25	2400		0.567	0.762		
		9.66	1527				0.572	0.762		
		9.40	1457				0.556	0.708		
		9.40	1457				0.551	0.708		
		9.13	1807				0.526	0.656		
		9.13	1807				0.515	0.656		
		0.30	19.8	245000	0.1	5500		0.173	0.156	
				21.2	176000				0.170	0.1673
				20.2	232000				0.185	0.1584
18.6	94100						0.214	0.185		
16.8	253000						0.173	0.152		
17.0	81200						0.199	0.188		
17.1	82300						0.200	0.187		
18.0	226000						0.189	0.1732		
17.7	67200						0.200	0.1990		
17.9	79500						0.206	0.195		
17.8	71830						0.206	0.196		
15.8	90000						0.186	0.1815		
16.8	30300						0.260	0.248		
17.0	29200						0.250	0.252		
17.0	27900						0.245	0.2566		
15.9	102300						0.183	0.1769		
18.8	81000				0.230	0.1951				
21.5	57100				0.250	0.2205				
20.2	76600				0.228	0.1989				
10.15	126000	0.75	1900		0.189	0.1656				

NAC 6-082
4-88

1/6 COLUMN COMPUTING SH

PROBLEM

Cont'd

TABLE II (Cont'd)

AEDC-TDR-63-35

EXP.	(C _D) LAM.	C _D RATIO	(C _D) LAM.	C _{DP}	C _{DB}	C _{DI}	Z MIN.	
EXPERIMENTAL DRAG EFFICIENT	PREDICTED LAMINAR DRAG COEFFICIENT	LAMINAR C _D PRED. LAM EXPERIMENTAL	PREDICTED LAMINAR SKIN FRICTION DRAG COEFFICIENT	PREDICTED PRESSURE DRAG COEFFICIENT	PREDICTED BASE DRAG COEFFICIENT	PREDICTED LAMINAR INDUCED DRAG COEFFICIENT	MINIMUM EQUIVALENT ALTITUDE	
0.15	0.181	0.15809	0.873	0.06087	0.05999	0.01352	0.02869	176,000
0.17	0.208	0.17463	0.840	0.07030	0.05500	0.01358	0.03575	183,500
1000	0.704	1.10000	1.562	0.49148	0.05528	0.01617	0.53704	GREATER THAN 200,000 FEET
1000	0.712	1.10000	1.546	0.49148	0.05528	0.01617	0.53704	
021	0.663	1.02130	1.541	0.46841	0.05538	0.01704	0.48049	
945	0.637	0.94553	1.484	0.44503	0.05550	0.01796	0.42705	
945	0.625	0.94553	1.513	0.44503	0.05550	0.01796	0.42705	
762	0.567	0.76251	1.344	0.36094	0.05511	0.01469	0.33176	
762	0.572	0.76251	1.333	0.36094	0.05511	0.01469	0.33176	
708	0.556	0.70885	1.276	0.34295	0.05521	0.01557	0.29513	
708	0.551	0.70885	1.287	0.34295	0.05521	0.01557	0.29513	
656	0.526	0.65685	1.248	0.32466	0.05532	0.01654	0.26033	
656	0.515	0.65685	1.276	0.32466	0.05532	0.01654	0.26033	↓
156	0.173	0.15673	0.906	0.02871	0.11786	0.00281	0.00735	147,500
1673	0.190	0.16738	0.881	0.03650	0.11799	0.00245	0.01045	156,000
5847	0.185	0.15847	0.857	0.03002	0.11790	0.00269	0.00787	149,000
185	0.214	0.18546	0.866	0.04968	0.11777	0.00321	0.01480	169,000
1529	0.173	0.15296	0.884	0.02538	0.11763	0.00436	0.00560	142,500
882	0.189	0.18825	0.946	0.05176	0.11766	0.00395	0.01489	170,000
1878	0.200	0.18789	0.940	0.05152	0.11766	0.00389	0.01484	169,500
732	0.189	0.17325	0.916	0.04092	0.11772	0.00346	0.01115	162,500
990	0.209	0.19106	0.995	0.05934	0.11770	0.00359	0.01844	176,000
1950	0.208	0.19500	0.937	0.05647	0.11771	0.00350	0.01731	175,000
1962	0.206	0.19623	0.952	0.05734	0.11771	0.00355	0.01763	174,500
1815	0.186	0.18155	0.976	0.04683	0.11761	0.00469	0.01241	166,500
248	0.260	0.24855	0.955	0.09262	0.11765	0.00406	0.03402	197,500
520	0.250	0.25257	1.010	0.09526	0.11766	0.00395	0.03571	199,000
566	0.245	0.25663	1.047	0.09786	0.11766	0.00395	0.03716	198,000
769	0.182	0.17699	0.979	0.04349	0.11761	0.00462	0.01126	162,500
951	0.230	0.19510	0.848	0.05624	0.11786	0.00281	0.01818	175,000
202	0.250	0.22021	0.881	0.07258	0.11802	0.00238	0.02722	186,500
989	0.228	0.19896	0.873	0.05860	0.11790	0.00269	0.01956	177,500
656	0.189	0.15546	0.876	0.02673	0.11845	0.01321	0.00727	148,000

66 COLUMN COMPUTING SHEET

COMPUTER

2

TABLE II (Cont'd)

θ	λ	M	Re_{0L}	T_w/T_f	T_f	α	$C_D \text{ EXP}$	$(C_D) \text{ LAM}$	C
CONE ANGLE (DEGREES)	BLUNTNESS RATIO	MACH NUMBER	REYNOLDS NUMBER	WALL TEMPERATURE RATIO	TOTAL TEMPERATURE (°R)	ANGLE OF ATTACK (DEGREES)	EXPERIMENTAL DRAG COEFFICIENT	PREDICTED LAMINAR DRAG COEFFICIENT	C
9°	0.30	10.17	24000	0.75	1900	0.0	0.169	0.15398	
		10.17	179400				0.182	0.15859	
		10.18	210800				0.165	0.15596	
		10.0	64500				0.192	0.18461	
		10.07	58000				0.200	0.18815	
		10.07	49200				0.207	0.19461	
		10.03	29280				0.235	0.22046	
		10.00	15140				0.286	0.26768	
		10.02	22300				0.257	0.23828	
		9.23	610	0.20	3000		0.760	1.08000	
		9.23	610				0.758	1.08000	
		9.23	610				0.772	1.08000	
		9.00	658				0.724	1.01250	
		9.00	658				0.731	1.01250	
		8.77	714				0.699	0.94723	
		8.77	714				0.684	0.94723	
		8.77	714				0.696	0.94723	
		9.06	1139	0.25	2400		0.642	0.78572	
		9.66	1139				0.648	0.78572	
		9.40	1235				0.590	0.73798	
		9.40	1235				0.608	0.73798	
		9.13	1346				0.577	0.69189	
		9.13	1346				0.585	0.69189	
		9.13	1346				0.565	0.69189	

TABLE II (Cont'd)

AEDC-TDR-63-55

C_D EXP	(C_D) LAM	C_D RATIO	(C_D) LAM	C_{DP}	C_{DB}	C_{DI}	Z MIN.
EXPERIMENTAL DRAG COEFFICIENT	PREDICTED LAMINAR DRAG COEFFICIENT	LAMINAR C_D PRED. LAM C_D EXPERIMENTAL	PREDICTED LAMINAR SKIN FRICTION COEFFICIENT	PREDICTED PRESSURE DRAG COEFFICIENT	PREDICTED BASE DRAG COEFFICIENT	PREDICTED LAMINAR INDUCED DRAG COEFFICIENT	MINIMUM EQUIVALENT SLUDGE
0.169	0.15398	0.911	0.01807	0.11844	0.01309	0.00438	132,500
0.182	0.15859	0.871	0.02155	0.11844	0.01312	0.00548	139,500
0.165	0.15596	0.945	0.01956	0.11844	0.01312	0.00484	135,500
0.182	0.18461	0.962	0.04011	0.11847	0.01335	0.01267	164,000
0.200	0.18815	0.941	0.04250	0.11849	0.01344	0.01373	167,000
0.207	0.19461	0.940	0.04689	0.11849	0.01344	0.01580	171,000
0.235	0.22046	0.938	0.06372	0.11850	0.01355	0.02468	189,500
0.286	0.26768	0.935	0.09175	0.11852	0.01364	0.04378	GREATER THAN 200,000 FEET
0.259	0.23828	0.920	0.07481	0.11851	0.01358	0.03138	191,000
0.760	1.08000	1.420	0.49725	0.11889	0.01617	0.44770	GREATER THAN 200,000 FEET
0.758	1.08000	1.424	0.49725	0.11889	0.01617	0.44770	
0.772	1.08000	1.377	0.49725	0.11889	0.01617	0.44770	
0.724	1.01250	1.399	0.47408	0.11901	0.01704	0.40241	
0.731	1.01250	1.385	0.47408	0.11901	0.01704	0.40241	
0.699	0.94723	1.355	0.45062	0.11914	0.01796	0.35950	
0.684	0.94723	1.325	0.45062	0.11914	0.01796	0.35950	
0.696	0.94723	1.360	0.45062	0.11914	0.01796	0.35950	
0.642	0.78572	1.224	0.36537	0.11867	0.01469	0.28698	
0.648	0.78572	1.212	0.36537	0.11867	0.01469	0.28698	
0.590	0.73798	1.252	0.34706	0.11880	0.01557	0.25655	
0.608	0.73798	1.214	0.34706	0.11880	0.01557	0.25655	
0.577	0.69189	1.199	0.32866	0.11894	0.01654	0.22775	
0.585	0.69189	1.182	0.32866	0.11894	0.01654	0.22775	
0.565	0.69189	1.224	0.32866	0.11894	0.01654	0.22775	↓

COLUMN COMPUTING SHEET

COMPUTER

2

TABULATED DRAG DATA AND RATIOS

θ	λ	M	Re _{0L}	T _w /T _f	T _f	α	C _{D EXP.}	(C _D) _{LAM.}	C _D
CONF ANGLE (DEGREES)	BRIGHTNESS RATIO	MACH NUMBER	REYNOLDS NUMBER	WALL TEMPERATURE RATIO	TOTAL TEMPERATURES (°R)	ANGLE OF ATTACK (DEGREES)	EXPERIMENTAL DRAG COEFFICIENT	PREDICTED LAMINAR DRAG COEFFICIENT	LAMINAR C _D
9.0	0.05	15.4	1,890,000	0.021	25700	1.5	0.0794	0.07538	0.07538
		15.4	750,000	0.021	25700	5.5	0.1194	0.11092	0.11092
		14.2	13,330,000	0.024	22000	1.8	0.0813	0.06848	0.06848
		14.1	12,640,000	0.025	21600	1.0	0.0870	0.06644	0.06644
		15.3	730,000	0.021	25300	3.3	0.1003	0.09327	0.09327
		14.9	1,790,000	0.022	24000	1.05	0.0910	0.07471	0.07471
		10.5	1,055,000	0.024	12200	2.63	0.0908	0.08890	0.08890
		10.5	1,990,000	0.044	12200	2.25	0.0866	0.08305	0.08305
		10.4	4,470,000	0.044	12000	1.6	0.0864	0.07694	0.07694
		11.0	1,490,000	0.040	13400	1.87	0.0804	0.08022	0.08022
		10.3	5,130,000	0.043	13000	1.65	0.0878	0.08404	0.08404
		9.7	7,105,000	0.051	10500	0.90	0.0891	0.07575	0.07575
		10.6	7,780,000	0.043	13000	0.95	0.0870	0.07301	0.07301
		10.6	3,190,000	0.043	3000	1.73	0.0853	0.07821	0.07821
		10.2	3,030,000	0.046	11500	0.85	0.0799	0.07707	0.07707
		10.3	3,380,000	0.045	11750	2.73	0.0849	0.08093	0.08093
		10.3	3,300,000	0.045	11750	3.52	0.0887	0.08914	1.08914
		14.9	6,280,000	0.022	24000	1.55	0.0798	0.06323	0.06323
		7.8	5,640,000	0.050	19700	1.73	0.0828	0.08118	0.08118
		15.1	3,935,000	0.032	24700	1.73	0.0759	0.07176	0.07176
15.4	5,050,000	0.021	25700	1.73	0.0750	0.07050	0.07050		
10.3	2,700,000	0.045	11750	2.84	0.0842	0.08451	1.08451		
15.1	2,850,000	0.022	24700	2.0	0.0764	0.07449	0.07449		
8.0	0.035	12.96	1,355,000	0.029	18300	1.55	0.1010	0.06802	0.06802
		12.92	1,304,000	0.029	18200	3.1	0.0831	0.07490	0.07490
		13.24	303,000	0.028	19100	10.3	0.205	0.18743	0.18743
		11.9	778,000	0.034	15500	14.5	0.301	0.26194	0.26194
		12.27	833,000	0.032	16450	12.4	0.222	0.21081	0.21081
		12.39	291,000	0.032	16700	16.4	0.358	0.33561	0.33561
		13.07	848,000	0.028	18600	4.36	0.1016	0.08831	0.08831
		12.90	1,094,000	0.029	18200	3.14	0.087	0.07498	0.07498
		13.06	287,000	0.029	18600	5.2	0.116	0.11329	1.11329
		13.13	328,000	0.029	18900	11.5	0.234	0.20952	0.20952

NO. 3082
4-53

16 COLUMN COMPUTING SHEET

PROBLEM

AND RATIOS

AIAA JOURNAL VOL 2, No. 11; AIAA PAPER No. 65-127, 1K5

CD	CD EXP.	(CD) LAM.	CD RATIO	(CD) LAM.	CDP	CD _B	CD _Z	Z MIN.	
LAM CD CD _B	EXPERIMENTAL DRAG COEFFICIENT	PREDICTED LAMINAR DRAG COEFFICIENT	LAMINAR CD PRED LAMINAR COEFFICIENT	PREDICTED LAMINAR SKIN FRICTION DRAG COEFFICIENT	PREDICTED PRESSURE DRAG COEFFICIENT	PREDICTED BASE DRAG COEFFICIENT	PREDICTED LAMINAR INDUCED DRAG COEFFICIENT	MINIMUM END 3" AT ALTITUDE	
0.0	0.0794	0.07538	0.950	0.0112	0.05704	0.00499	0.00223	97,000	
0.0	0.1194	0.11092	0.929	0.01956	0.08154	0.00499	0.00482	116,500	
0.0	0.0813	0.06848	0.842	0.00370	0.05804	0.00606	0.00067	56,500	
0.0	0.0870	0.06644	0.764	0.00376	0.05584	0.00617	0.00066	56,000	
0.0	0.1003	0.09327	0.930	0.01903	0.06489	0.00507	0.00428	117,000	
0.0	0.0910	0.07471	0.822	0.01123	0.05591	0.00540	0.00217	97,500	
0.0	0.0908	0.08890	0.979	0.01278	0.06200	0.01226	0.00186	100,500	
0.0	0.0866	0.08305	0.959	0.00920	0.06030	0.01226	0.00129	89,000	
0.0	0.0864	0.07694	0.890	0.00569	0.05797	0.01252	0.00076	70,000	
0.0	0.0504	0.08022	0.994	0.00914	0.05871	0.01105	0.00132	88,500	
0.0	0.0878	0.08404	0.957	0.01224	0.05807	0.01200	0.00173	100,000	
0.0	0.0891	0.07575	0.850	0.00426	0.05642	0.01457	0.00052	59,000	
0.0	0.0870	0.07301	0.839	0.00421	0.05673	0.01200	0.00056	60,000	
0.0	0.0853	0.07821	0.916	0.00693	0.05833	0.01200	0.00095	78,000	
0.0	0.0799	0.07707	0.964	0.00697	0.05615	0.01307	0.00089	78,500	
0.0	0.0848	0.08093	0.978	0.00667	0.06255	0.01279	0.00092	77,000	
1.0	0.0887	0.08914	1.005	0.00820	0.06697	0.01279	0.00119	84,000	
0.0	0.0798	0.06323	0.839	0.00564	0.05720	0.00540	0.00107	71,000	
0.0	0.0828	0.08118	0.980	0.00741	0.05858	0.01425	0.00094	81,000	
0.0	0.0759	0.07176	0.945	0.00735	0.05776	0.00523	0.00143	81,000	
0.0	0.0750	0.07050	0.940	0.00648	0.05775	0.00499	0.00128	75,500	
1.0	0.0842	0.08451	1.004	0.00756	0.06310	0.01279	0.00105	81,000	
0.0	0.0764	0.07449	0.975	0.00881	0.05871	0.00523	0.00174	87,500	
0.0	0.1010	0.06802	0.673	0.01265	0.04582	0.00743	0.00212	100,000	
0.0	0.0831	0.07490	0.902	0.01280	0.05233	0.00749	0.00227	100,000	
0.0	0.205	0.18743	0.914	0.03523	0.13517	0.00706	0.00996	132,500	
0.0	0.301	0.26194	0.870	0.02239	0.22419	0.00908	0.00628	109,500	
0.0	0.222	0.21081	0.950	0.02078	0.17601	0.00846	0.00556	109,000	
0.0	0.359	0.33561	0.937	0.04080	0.27365	0.00827	0.01289	132,000	
0.0	0.1016	0.08831	0.870	0.01705	0.06057	0.00729	0.00341	109,000	
0.0	0.087	0.07498	0.862	0.01266	0.05256	0.00752	0.00225	99,000	
1.0	0.116	0.11329	1.029	0.03113	0.06754	0.00730	0.00731	133,000	
0.0	0.234	0.20952	0.912	0.03480	0.15744	0.00721	0.01008	130,000	

16 COLUMN COMPUTING SHEET

COMPUTER

-74-

2

TABLE II (Cont'd)

θ	λ	M	R_{0L}	T_w/T_f	T_T	α	$C_D \text{ EXP.}$	$(C_D)_{\text{LAM}}$	C
CONE ANGLE (DEGREES)	BLUNTNES RATIO	MACH NUMBER	REYNOLDS NUMBER	WALL TEMPERATURE RATIO	TOTAL TEMPERATURE (°R)	ANGLE OF ATTACK (DEGREES)	EXPERIMENTAL DRAG COEFFICIENT	PREDICTED DRAG COEFFICIENT	
8.0	0.035	12.74	350,000	0.024	17700	6.1	0.134	0.11883	
		12.50	2,026,000	0.031	17500	2.7	0.0733	0.07021	
		12.55	3,021,000	0.030	17500	0.78	0.0638	0.06054	
		10.96	5,000,000	0.041	17400	2.43	0.0900	0.07539	
		15.05	74,000	0.022	24500	10.92	0.262	0.26562	
		14.84	5,000,000	0.022	24000	9.90	0.223	0.23301	
		15.19	11,000	0.021	24900	17.35	0.436	0.42955	
		15.07	91,000	0.022	24500	16.6	0.400	0.40463	
		15.40	84,000	0.021	25500	12.9	0.311	0.30649	
		15.32	84,000	0.021	25300	6.45	0.404	0.40720	
		14.57	3,090,000	0.023	24000	5.16	0.0228	0.02294	
		16.30	91,000	0.019	24000	7.8	0.204	0.19754	
		16.19	87,000	0.019	28100	16.45	0.414	0.40989	
		13.04	73,000	0.029	18300	17.0	0.536	0.48844	
		16.14	84,000	0.019	24000	19.3	0.540	0.50883	
		11.89	4,204,000	0.034	15500	3.5	0.0792	0.07193	
		11.73	4,540,000	0.035	15500	2.45	0.0774	0.06613	
		12.90	5,028,000	0.029	15000	0.45	0.0754	0.05852	
		15.21	77,000	0.021	24000	7.15	0.311	0.19207	

NAD 6-002
4-80

16 COLUMN COMPUTING SHEET

PROBLEM

1

TABLE II (Cont'd)

AIAA JOURNAL Vol 2, No 11; AIAA PAPER No. 65-127

α	C _D EXP.	(C _D) LAM.	C _D RATIO	(C _{Df}) LAM.	C _{Dp}	C _{DB}	C _{DI}	Z MIN.	
ANGLE OF ATTACK (DEGREES)	EXPERIMENTAL DRAG COEFFICIENT	PREDICTED LAMINAR DRAG COEFFICIENT	LAMINAR DRAG COEFFICIENT RATIO	PREDICTED LAMINAR DRAG COEFFICIENT	PREDICTED DRAG COEFFICIENT	PREDICTED BASE DRAG COEFFICIENT	PREDICTED LAMINAR INDUCED DRAG COEFFICIENT	MINIMUM EQUIVALENT ALTITUDE	
6.1	0.134	0.11883	0.886	0.02818	0.07637	0.00774	0.00654	127,500	
7.7	0.0733	0.07021	0.958	0.01015	0.05031	0.00810	0.00166	90,000	
9.78	0.0638	0.06054	0.948	0.00747	0.04411	0.00787	0.00110	78,000	
12.42	0.0900	0.07539	0.838	0.01323	0.04926	0.01097	0.00193	101,000	
10.92	0.262	0.26562	1.014	0.08224	0.14606	0.00519	0.03213	170,000	
14.90	0.223	0.23301	1.045	0.07269	0.12805	0.00533	0.02694	165,000	
17.35	0.436	0.42955	0.985	0.08799	0.29964	0.00508	0.03684	164,000	
16.6	0.400	0.40463	1.012	0.08597	0.27819	0.00518	0.03529	164,000	
13.9	0.316	0.30649	0.967	0.08245	0.18597	0.00492	0.03316	167,000	
16.45	0.404	0.40720	1.009	0.09031	0.27397	0.00498	0.03795	167,000	
15.16	0.1028	0.08394	0.816	0.00929	0.06705	0.00562	0.00198	95,000	
7.8	0.204	0.19754	0.968	0.06980	0.09632	0.00429	0.02714	166,000	
16.45	0.414	0.40989	0.989	0.09158	0.27385	0.00436	0.04010	167,500	
19.0	0.536	0.48844	0.912	0.09388	0.35105	0.00733	0.03619	166,500	
19.3	0.503	0.50883	1.011	0.09967	0.35766	0.00839	0.04510	168,500	
3.5	0.0792	0.07193	0.908	0.00696	0.05480	0.00910	0.00106	73,000	
2.45	0.05734	0.06613	0.901	0.00656	0.04926	0.00929	0.00093	73,000	
0.45	0.05604	0.05852	1.027	0.00642	0.04365	0.00752	0.00093	72,500	
7.15	0.111	0.19207	1.73	0.07207	0.08807	0.00506	0.02687	168,500	

16 COLUMN COMPUTING SHEET

COMPUTER

2

TABLE II (Cont. d)

TABULATED DRAG DATA AND RATIOS

θ	L	M	Re _{00L}	T _w /T _f	T _T	α	C _{D,EXP.}	(C _D) _{LAM.}	C
CONE ANGLE (DEGREES)	BLUNTHNESS RATIO	MACH NUMBER	REYNOLDS NUMBER	WALL TEMPERATURE RATIO	TOTAL TEMPERATURE (°R)	ANGLE OF ATTACK (DEGREES)	EXPERIMENTAL DRAG COEFFICIENT	PREDICTED LAMINAR DRAG COEFFICIENT	L C C
9	0.03	14.96	148,000	0.0221	58914	0.0	0.1228	0.11272	
		14.72	138,000	0.0226	51814	5.0	0.1437	0.14200	
		14.70	140,000	0.0226	62876	10.0	0.2012	0.21646	
		14.67	132,000	0.0227	62083	15.0	0.2122	0.33713	
		14.65	131,000	0.0228	63421	15.0	0.3151	0.33733	
		13.63	17,000	0.0262	62175	0.0	0.2195	0.24796	
		13.70	19,000	0.0260	60884	10.0	0.3099	0.37014	
		13.75	18,000	0.0258	59379	20.0	0.5496	0.68221	
		13.64	18,000	0.0262	61832	0.0	0.2364	0.24279	
		14.36	52,000	0.0237	59198	0.0	0.1482	0.15657	
Y		14.30	50,000	0.0239	60292	15.0	0.3625	0.39661	
6.5		14.66	145,000	0.0227	63612	0.0	0.0989	0.09465	
		14.65	144,000	0.0228	63421	5.0	0.1318	0.12044	
		14.66	143,000	0.0228	63729	10.0	0.2039	0.19253	
		14.61	141,000	0.0229	64366	15.0	0.3394	0.30391	
		14.64	142,000	0.0228	63947	0.0	0.1030	0.09547	
		14.63	142,000	0.0229	64254	15.0	0.3281	0.30367	
		13.79	20,000	0.0256	59203	0.0	0.2325	0.23962	
		13.72	19,000	0.0256	60351	10.0	0.3277	0.37811	
		13.65	18,600	0.0261	61340	20.0	0.7311	0.69777	
		14.36	56,800	0.0237	58734	0.0	0.1412	0.14178	
		13.65	18,600	0.0261	61111	0.0	0.2220	0.25035	
	Y	13.77	20,300	0.0256	59023	20.0	0.5832	0.68153	
	0.145	14.59	122,000	0.0230	64521	0.0	0.1007	0.10849	
		14.59	125,000	0.0230	64956	5.0	0.1370	0.12880	
		14.60	128,000	0.0229	65152	10.0	0.2074	0.18564	
		14.61	125,000	0.0229	64366	20.0	0.4936	0.40203	
		13.63	17,400	0.0262	62633	0.0	0.2217	0.25558	
		13.72	18,100	0.0260	60269	5.0	0.2584	0.28167	
		13.67	18,100	0.0260	62076	10.0	0.3525	0.36088	
Y	Y	13.67	17,400	0.0260	61384	20.0	0.6948	0.63360	

PROBLEM

TABLE II (Cont'd)

AND RATIOS

AEDC-TDR-63-177

$C_{D EXP.}$	$(C_D)_{LAM}$	C_D RATIO	$(C_D)_{LAM}$	C_{DP}	C_{DB}	C_{DI}	Z MIN.
EXPERIMENTAL DRAG COEFFICIENT	PREDICTED LAMINAR DRAG COEFFICIENT	LAMINAR C_D PRED. LAMINAR C_D EXPERIMENTAL	PREDICTED LAMINAR SKIN FRICTION DRAG COEFFICIENT	PREDICTED PRESSURE DRAG COEFFICIENT	PREDICTED BASE DRAG COEFFICIENT	PREDICTED LAMINAR INDUCED DRAG COEFFICIENT	MINIMUM EQUIVALENT ALTITUDE
0.1229	0.11272	0.919	0.04287	0.05325	0.00544	0.01117	152,500
0.1437	0.14200	0.998	0.04663	0.07629	0.00556	0.01351	153,000
0.2012	0.21646	1.076	0.05248	0.14107	0.00558	0.01734	153,000
0.3122	0.33713	1.080	0.06143	0.24741	0.00561	0.02268	154,000
0.3151	0.33733	1.071	0.06157	0.24741	0.00563	0.02272	154,000
0.2195	0.24796	1.130	0.13059	0.05331	0.00669	0.05737	GREATER THAN 200,000 FEET
0.3099	0.37014	1.194	0.15204	0.14121	0.00661	0.07038	
0.5496	0.68221	1.241	0.18833	0.39566	0.00655	0.09167	
0.2364	0.24279	1.027	0.12759	0.05331	0.00668	0.05521	↓
0.1482	0.15657	1.056	0.07352	0.05327	0.00590	0.02389	177,500
0.3625	0.39661	1.094	0.10175	0.24749	0.00596	0.04140	179,000
0.0789	0.09465	0.957	0.04689	0.02831	0.00541	0.01404	152,000
0.1318	0.13044	0.914	0.05140	0.04727	0.00542	0.01635	152,000
0.2039	0.19253	0.944	0.06186	0.10409	0.00542	0.02116	152,000
0.3394	0.30391	0.895	0.07329	0.19827	0.00545	0.02680	152,000
0.1030	0.09547	0.927	0.04746	0.02831	0.00542	0.01428	152,000
0.3281	0.30367	0.925	0.07322	0.19827	0.00543	0.02675	152,000
0.2225	0.23962	1.031	0.13065	0.02834	0.00626	0.07436	GREATER THAN 200,000 FEET
0.3277	0.37811	1.154	0.17380	0.10420	0.00634	0.09378	
0.7311	0.69777	0.954	0.23786	0.33021	0.00642	0.12329	↓
0.1412	0.14178	1.004	0.07690	0.02832	0.00568	0.03088	176,000
0.2220	0.25035	1.129	0.13626	0.02835	0.00642	0.07932	GREATER THAN 200,000 FEET
0.6832	0.68153	0.999	0.22828	0.33015	0.00628	0.11681	↓
0.1007	0.10849	1.077	0.05243	0.03569	0.00547	0.01490	157,500
0.1372	0.12880	0.940	0.05652	0.05067	0.00547	0.01614	157,500
0.2079	0.18564	0.895	0.06693	0.09426	0.00546	0.01899	155,000
0.4936	0.45203	0.914	0.09136	0.27802	0.00545	0.02720	157,500
0.2217	0.25558	1.153	0.13971	0.03586	0.00644	0.07357	GREATER THAN 200,000 FEET
0.2584	0.28167	1.090	0.14951	0.05089	0.00634	0.07493	
0.3525	0.36089	1.024	0.17837	0.09470	0.00640	0.08142	
0.6948	0.69360	0.999	0.24424	0.27932	0.00640	0.10364	↓

16 COLUMN COMPUTING SHEET

COMPUTER

2

TABLE II (Cont'd)

θ	λ	M	R_{00L}	T_w/T_f	T_T	α	C_D EXP.	(C_D) LAM.
CONE ANGLE (DEGREES)	BLUNTNES RATIO	MACH NUMBER	REYNOLDS NUMBER	WALL TEMPERATURE RATIO	TOTAL TEMPERATURE (°R)	ANGLE OF ATTACK (DEGREES)	EXPERIMENTAL DRAG COEFFICIENT	PREDICTED LAMINAR DRAG COEFFICIENT
6.5	.145	14.31	49,800	0.0239	60462	0	0.1361	0.15736
		14.29	49,100	0.0239	60794	0	0.1440	0.15831
		14.62	125,000	0.0229	63842	5	0.1406	0.12917
		14.74	21,900	0.0230	51700	0	0.1911	0.23659
		20.90	6,040	0.0117	73333	0	0.4295	0.73589
		21.72	12,800	0.0108	69260	0	0.3487	0.45694
		21.80	30,200	0.0108	71850	0	0.2326	0.26986
		15.03	223,000	0.0222	51130	0	0.0854	0.08098
		15.01	219,000	0.0222	50960	10	0.1977	0.17511
		21.83	35,400	0.0108	71480	0	0.2336	0.24772
		21.72	14,300	0.0108	69810	0	0.3349	0.45247
		20.93	6,750	0.0117	73250	0	0.4370	0.75876
		21.05	6,750	0.0115	72170	10	0.5995	0.98268
		20.87	6,750	0.0116	74310	20	1.0979	1.4113
		15.06	241,000	0.0220	50500	20	0.4480	0.42203
9.0		14.73	100,000	0.0225	62000	5	0.1997	0.19563
		14.72	100,000	0.0226	62040	0	0.1694	0.17773
		14.71	101,600	0.0226	62570	10	0.2577	0.24374
		14.77	100,000	0.0224	61030	20	0.4866	0.42198
	Y	14.75	96,300	0.0224	61650	0	0.1745	0.17882

PROBLEM

TABLE II (Cont'd)

AEDC TDR-63-177

C_D EXP.	(C_D) LAM.	C_D RATIO	(C_D) LAM.	C_{DP}	C_{DB}	C_{DI}	Z MIN	
EXPERIMENTAL DRAG COEFFICIENT	PREDICTED LAMINAR DRAG COEFFICIENT	LAMINAR C_D PREDICTED EXPERIMENTAL	PREDICTED LAMINAR DRAG COEFFICIENT	PREDICTED PRESSURE DRAG COEFFICIENT	PREDICTED BASE DRAG COEFFICIENT	PREDICTED LAMINAR INDUCED DRAG COEFFICIENT	MINIMUM EQUALLY ALTITUDE	
0.1361	0.15736	1.156	0.08421	0.03573	0.0057	0.03169	179,000	
0.1440	0.15831	1.099	0.08480	0.03574	0.00575	0.03203	180,000	
0.1406	0.12917	0.919	0.05677	0.05066	0.00544	0.01629	156,000	
0.1911	0.23659	1.239	0.12810	0.03569	0.00547	0.06733	GREATER THAN 200,000 FEET	
0.4295	0.73589	1.713	0.28737	0.03526	0.00249	0.41077		
0.3487	0.45694	1.310	0.20109	0.03524	0.00230	0.21930		
0.2326	0.26986	1.160	0.13134	0.03524	0.00229	0.10099		
0.0854	0.08098	0.949	0.03742	0.02831	0.00524	0.01001	142,500	
0.1977	0.17511	0.886	0.04978	0.10407	0.00523	0.01603	143,500	
0.2336	0.24772	1.060	0.11957	0.02829	0.00229	0.09757	199,000	
0.3349	0.45247	1.351	0.19308	0.02829	0.00231	0.22879	GREATER THAN 200,000 FEET	
0.4370	0.75876	1.736	0.28282	0.02828	0.00249	0.44517		
0.5995	0.98268	1.639	0.38291	0.10399	0.00246	0.49332		
1.0879	1.4113	1.297	0.52257	0.32948	0.00249	0.55675		
0.4490	0.42203	0.942	0.06369	0.32974	0.00521	0.02339	141,000	
0.1987	0.19563	0.984	0.04596	0.13218	0.00555	0.01194	161,000	
0.1674	0.17723	1.046	0.04361	0.11657	0.00556	0.01149	161,000	
0.2577	0.24374	0.946	0.05166	0.17389	0.00557	0.01263	161,000	
0.4866	0.42198	0.867	0.06613	0.33478	0.00552	0.01555	161,000	
0.1745	0.17882	1.025	0.04478	0.11657	0.00553	0.01193	162,500	

16 COLUMN COMPUTING SHEET

COMPUTER

TABLE II (Concl'd)

DATA AND RATIOS

AEDC-TDR-62-43

CD	CD EXP.	(CD) LAM	CD RATIO	(CDf) LAM	CDP	CD B	CD E	Z MIN.
LAMINAR DRAG COEFFICIENT	PREDICTED LAMINAR DRAG COEFFICIENT	LAMINAR DRAG COEFFICIENT	PREDICTED LAMINAR SKIN FRICTION DRAG COEFFICIENT	PREDICTED PRESSURE DRAG COEFFICIENT	PREDICTED BASE DRAG COEFFICIENT	PREDICTED LAMINAR INDUCED DRAG COEFFICIENT	MINIMUM EQUIVALENT ALTITUDE	
0.14	0.10605	0.757	0.03099	0.06400	0.00238	0.00822	144,000	
0.20	0.13806	0.6903	0.05217	0.06408	0.00238	0.019511	167,500	
0.205	0.15668	0.764	0.06364	0.06401	0.00251	0.02653	176,000	
0.2	0.15776	0.873	0.08194	0.06482	0.00256	0.03924	182,000	
0.14	0.11669	0.788	0.03830	0.06399	0.00220	0.01221	152,500	
0.275	0.11758	0.591	0.03064	0.07789	0.00235	0.02760	140,000	
0.275	0.11773	0.638	0.02525	0.07787	0.00278	0.025538	133,000	
0.20	0.17416	0.871	0.03749	0.12452	0.00301	0.03914	141,000	
0.338	0.24856	0.735	0.03927	0.20369	0.00264	0.06796	137,500	
0.338	0.25646	0.759	0.04017	0.20378	0.00285	0.00367	131,000	
0.47	0.37290	0.771	0.04718	0.3532	0.00285	0.01205	139,000	

16 COLUMN COMPUTING SHEET

COMPUTER

2

E. Applications to Flight Conditions

In an attempt to evaluate the accuracy of the analytical drag equations derived in this report, the equations should also be compared to flight test data. Applying the theory to flight conditions is necessary for the following reasons:

- 1) The primary employment of the equations will be for predicting drag coefficients in reentry flight.
- 2) Some portions of the analytical expressions were based on flight environments; i. e., base drag, real gas curve-fits to the reference enthalpy method, and boundary layer transition.
- 3) The ground test data does not adequately cover the Mach number Reynolds number regime encountered in this study.
- 4) The ground test data does not consist of sufficient turbulent flow data to compare with theory; also it is not known how much of the boundary layer is turbulent.
- 5) Flight test data is presently the primary means of evaluating the effects of ablation on vehicle drag.

At the present time, there is a very small amount of reliable flight test data that can be used for this purpose. The reasons for this scarcity are as follows:

- 1) To investigate the viscous effects, the flight vehicle should be a slender body so that the skin-friction and induced drag will be a significant part of the total drag.
- 2) The vehicle should be instrumented with sensitive accelerometers. The results of integrating the accelerometer measurements should yield a trajectory that agrees with the tracking data.
- 3) It is also desirable to have a vehicle that is instrumented with pressure taps so that the pressure drag portion of the total drag may be determined. However, on slender sharp cones, this is generally not necessary since the pressure drag at high Mach numbers can be calculated quite accurately.

At the present time, Avco RAD has reliable flight test drag data from three conical vehicles which are very nearly pointed ($RN/RB = 0.013$). The data from two of these flights is presently being reduced; the results of one of the flights have already been documented (reference 42). The total drag data from this flight is presented in figure 32, together with the results of the theory which has been developed in this report. The estimate of the altitude range of transition was obtained from the results presented in Section VI.

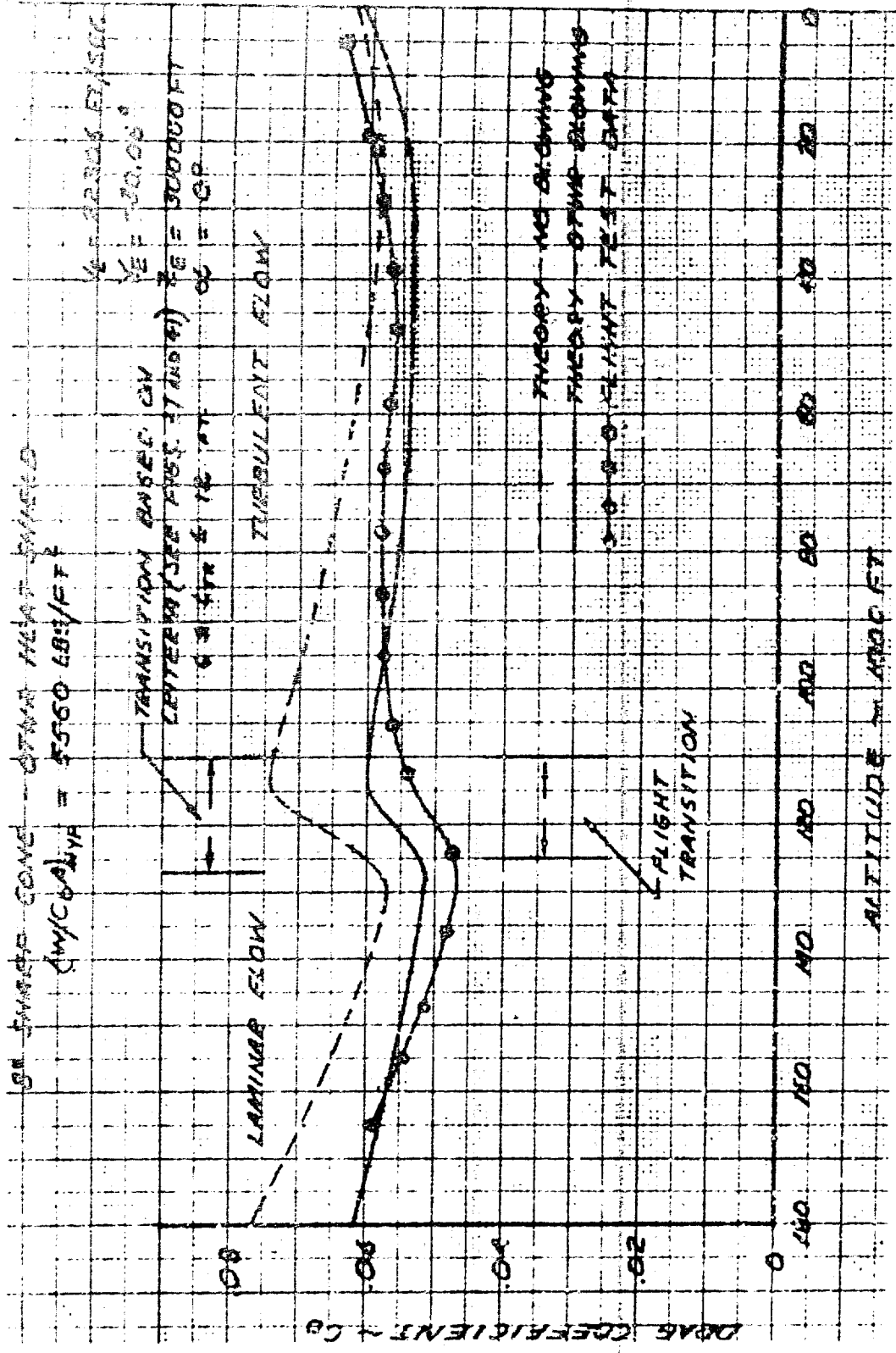


Figure 32 TOTAL DRAG COEFFICIENT

Included in this comparison are the theoretical results obtained when the effects of mass addition are neglected. The actual vehicle was covered with a phenolic refrasil heat shield (except for Teflon in the tip region); outgassing began at about 200,000 feet, and surface ablation commenced at about 100,000 feet. The skin-friction drag coefficient was reduced for blowing by the approximate method, employing figure 18.

This comparison indicates good agreement between the flight test data, and the analytical methods presented in this report; the differences are within the limits of the accuracy requirements.

Until the discrepancies between theory and test data can be more thoroughly evaluated, it is recommended that the equations derived in this report be employed to predict the drag of conical flight vehicles to an accuracy that is within the specified requirement. One of the reasons for the differences between theory and flight test data might be the method used to account for mass addition effects. If this is the case, then it would be necessary to employ the more rigorous methods of analysis mentioned in sections III-5 and IV-6.

VI. BOUNDARY LAYER TRANSITION ON CONES

The objective of this transition study was to develop a method of estimating the altitude at which a conical reentry vehicle (sharp or blunt) would begin to undergo boundary layer transition. In order to show how such a method has been developed, the following paragraphs deal with a discussion of the transition criterion, how the criterion is employed, and how the results have been correlated.

A. Discussion of Transition Criterion

The criterion presently employed has been obtained from the flight test results of various reentry vehicle programs. Reference 43 provides a discussion of the flight test data, how it was interpreted, and how it was correlated to yield a reasonable criterion.

This investigation of flight data indicated that the transition Reynolds number was most influenced by the local Mach number at the edge of the boundary layer. More specifically, correlation was achieved when the computed values of local Reynolds number at the observed transition altitudes for each flight were plotted versus the corresponding computed values of local Mach number. These results are represented by the curve in figure 33 which is a "best estimate" of the band of data.

The data actually includes large variations of the other parameters which influence transition: nose blunting, angle of attack, pressure gradients, body forces, surface roughness, wall temperature, and mass injection rates. Although the effect of each of these parameters is known to be significant, the net effect did not alter the observed transition altitudes very much (less than 15,000 feet). This is qualitatively attributed to the fact that several of these effects tend to oppose each other. For example, the low wall temperatures resulting from a low temperature ablator tends to stabilize the boundary layer; however, the high mass injection rates associated with low temperature ablators tend to destabilize the boundary layer (reference 44). Furthermore, a cool wall thins the boundary layer, magnifying the destabilizing effect of surface roughness. This opposing effect has been experimentally demonstrated. (Reference 45 and others).

The angle of attack effect is generally quite significant, and it is an effect which is most difficult to evaluate. However, based on the flight test results shown in reference 43, significant differences in angle of attack did not alter the transition altitude by more than 10,000 feet.

The effect of nose blunting is partially accounted for in the present criterion since the actual nose bluntness strongly influences the local Reynolds number - Mach number distribution along the body. The consequence of nose

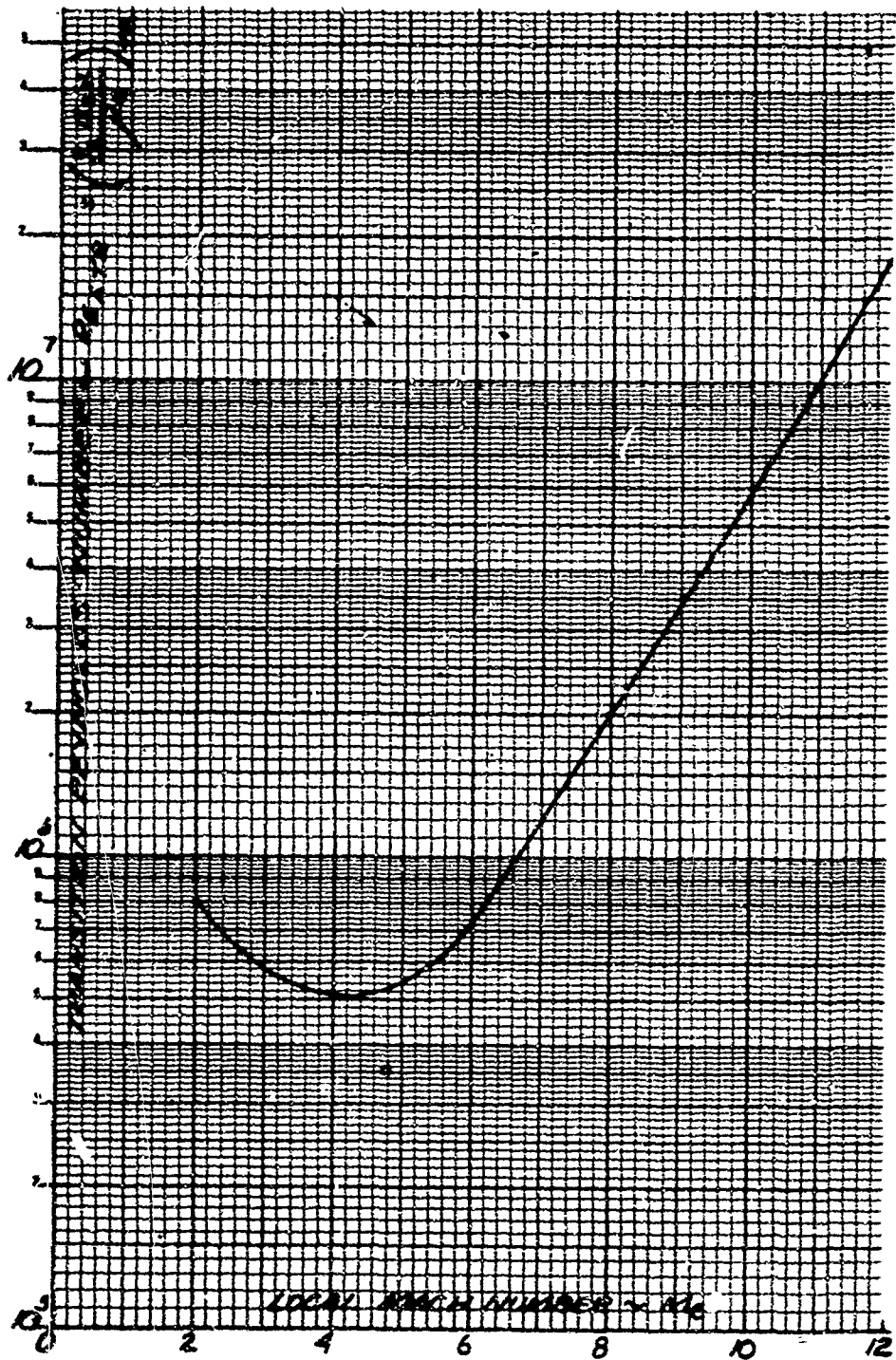


Figure 33 TRANSITION REYNOLDS NUMBER VERSUS LOCAL MACH NUMBER

blunting that is not accounted for is the destabilizing effect of the adverse pressure gradient which generally follows the overexpansion at the sphere-cone tangent point. For low bluntness configurations, this effect is not very critical since the adverse gradient occurs in the forward region of the cone where the Reynolds number is low compared to the rear portion.

The present criterion shown in figure 33 illustrates how significant the local Mach number effect is, covering about two orders-of-magnitude of $(Re_x)_{TR}$ or about 100,000 feet in altitude. Although this graph was constructed from flight test results with numerous other influencing parameters inherent in the data, the trend is quite typical of most of the wind tunnel data where the test conditions were carefully controlled (reference 46 and others).

The "bucket" in the curve at $M_e = 4$ is also characteristic of wind tunnel results.

B. Employment of Criterion

In employing the criterion of figure 33 to predict the altitudes where boundary layer transition occurs, it is necessary to evaluate the Reynolds number - Mach number ($Re_x - M_e$) distributions along the edge of the boundary layer. For this task, the following methods of analysis are employed:

a. Sharp Cone

For this case, M_e and the local unit Reynolds number, Re , are constant with respect to surface distance, x . The values of these quantities as a function of free-stream conditions and cone angle are then easily obtained from conical flow theory; i. e., reference 1.

b. Blunt Cone

For this case, the $Re_x - M_e$ distribution along the edge of the boundary layer is determined from the blunt body viscid-inviscid method of analysis (references 24 & 25) (Computer Program 1115B). This procedure employs method of characteristics solutions (reference 3) (Computer Program 596) for the pressure distribution and shock shape. The blunt body viscid-inviscid method of analysis is an iterative procedure as outlined below for a particular body station:

- 1) Employing the known pressure (from the method of characteristics), assume a value of entropy for the external flow. These two properties are then used in Mollier charts to obtain all other required properties external to the boundary layer.
- 2) Employing these external properties in conjunction with the known wall conditions, compute the mass flow in the laminar boundary layer.

3) By performing a mass balance between the boundary layer flow and the free stream flow which is entrained in the boundary layer, compute the stream-tube radius of the free-stream mass flow.

4) Employing the known shock shape (from the method of characteristics), determine the shock angle at the location where the bounding streamline intersects the shock.

5) From this shock angle and free-stream Mach number, the entropy behind the shock is determined. This is compared to the assumed entropy, and iterations are made until the solution converges.

Some typical $Re_x - M_e$ distributions resulting from the blunt cone method of analysis are presented in figures 34 to 36 for cone angles of 8, 10, and 15 degrees with varying lengths. The lines of constant length, x , represent the slant length of the equivalent sharp cone (i. e., surface distance from theoretical sharp tip to end of cone). For each value of x , the corresponding body radius is given, so that the bluntness ratio may easily be calculated for a specific configuration. The actual nose radii selected correspond to a bluntness ratio of 0.05, for $x = 12$ feet. Additional $Re_x - M_e$ distributions for other nose radii are reported in reference 47.

The above investigation was conducted for a free-stream velocity of 25,000 ft/sec at several altitudes encompassing the expected range of transition. The effect of decreasing the velocity is to reduce both Re_x and M_e , thus shifting the maps down and to the left.

The distributions presented in figures 34 through 36 show how Re_x and M_e increase along the body approaching the sharp cone value. At high altitudes, conical flow is reached sooner on the body because of the thick boundary layer which is capable of entraining a large mass flow. At lower altitudes, the body length required to reach conical flow increases, and for $L \lesssim 12$ feet, the results show that in many cases conical flow will not be attained. The results also show that the more slender the cone the greater the distance required to reach conical flow. A closed form solution for the distance required to attain conical flow on a blunt cone has been derived in reference 25.

In using these $Re_x - M_e$ maps to determine the transition altitude and the mode of transition, the criterion shown in figure 33 is superimposed on the maps.

This procedure yields the altitude at which a particular body station (x) will undergo transition. A station is considered to become turbulent when its $Re_x - M_e$ value is such that it falls just above the criterion curve. By

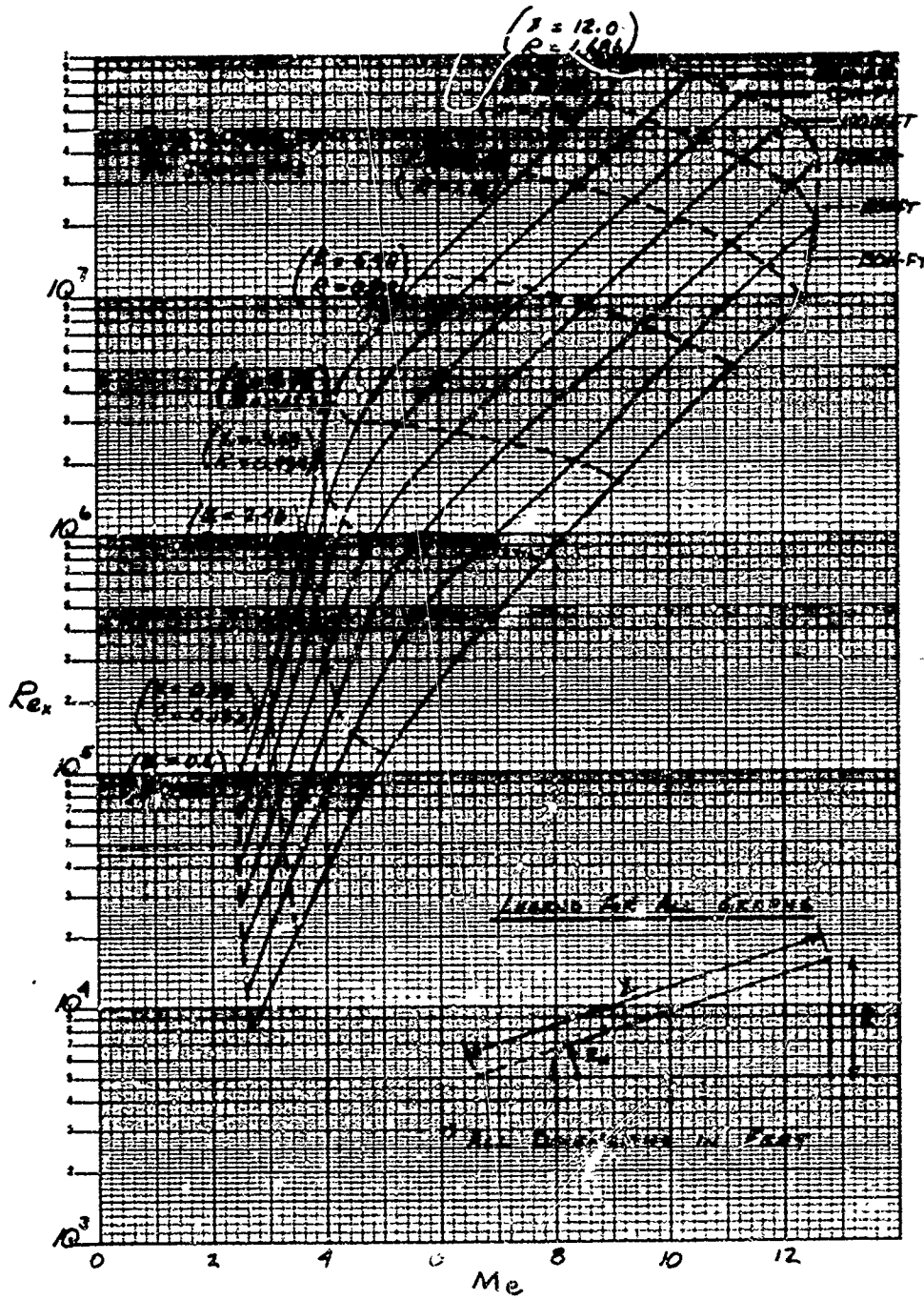


Figure 34 REYNOLDS NUMBER VARIATION 8° BLUNT CONE

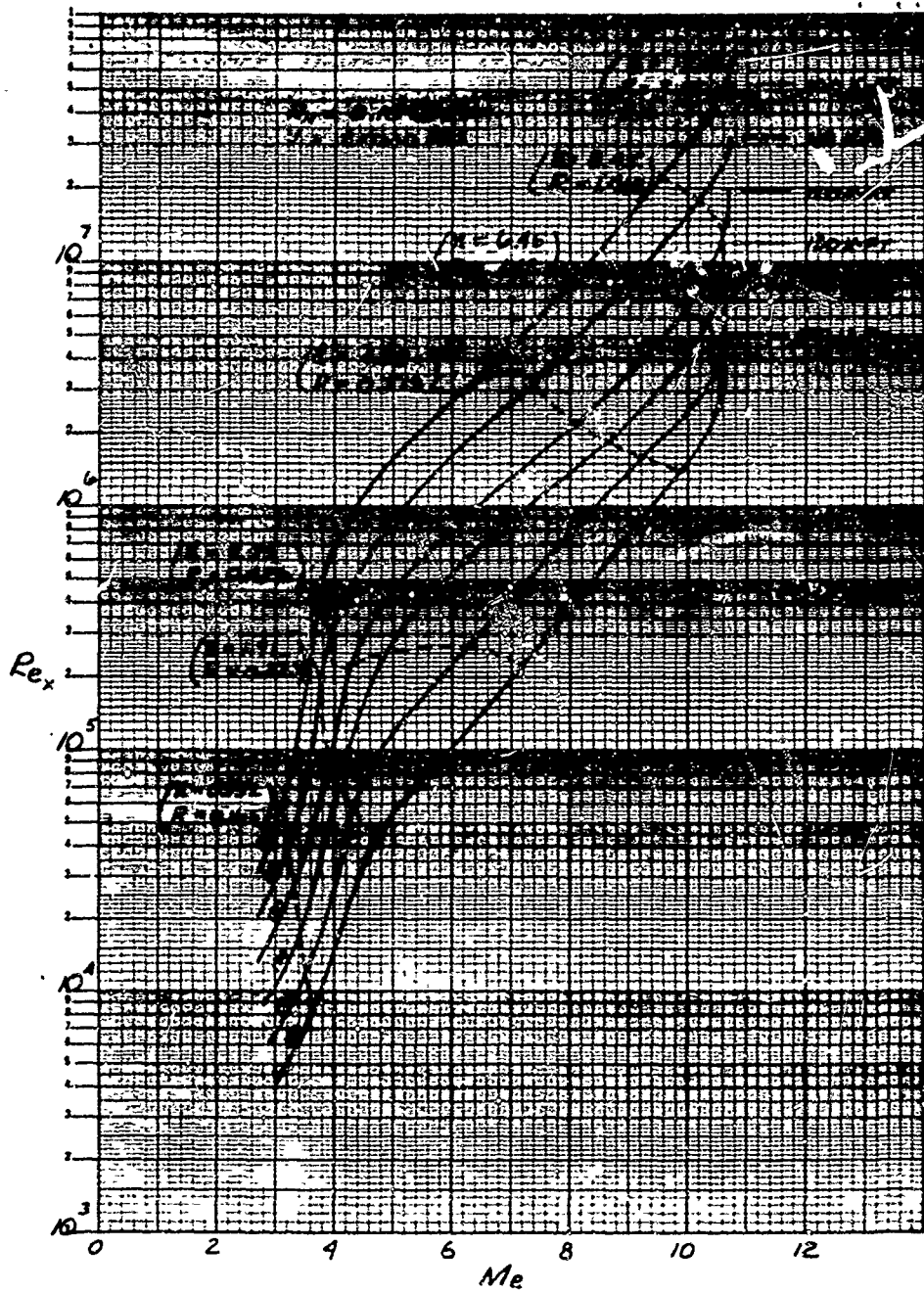


Figure 35 REYNOLDS NUMBER VARIATION 10° BLUNT CONE

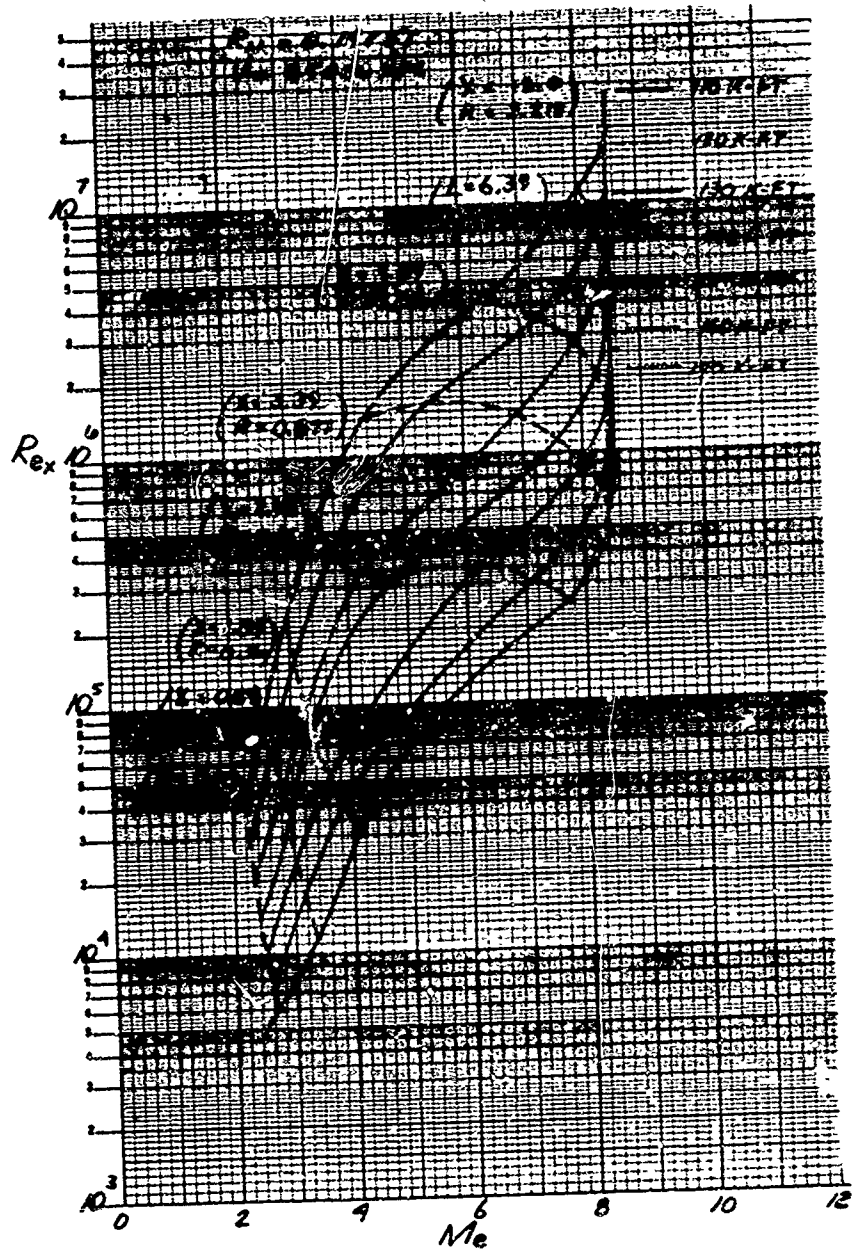


Figure 36 REYNOLDS NUMBER VARIATION 15° BLUNT CONE

determining the transition altitude for several values of x , the mode of transition for a particular vehicle may be evaluated.

C. Correlation of Results

The transition criterion (figure 33 and the $(Re_x - M_e)$ maps (figures 34 to 36, plus those presented in reference 47) have been employed in a generalized study in order to correlate the transition altitude as a function of cone angle, body length, bluntness ratio, and free-stream velocity.

Based on the ranges of variables considered, and the validity of the transition criterion employed, the investigation should yield reasonable results for the following conditions:

cone angle: $8^\circ \leq \theta \leq 15^\circ$

body length: $1' \leq L \leq 12'$

bluntness ratio: $0 \leq R_N/R_B \leq 0.3$

free-stream velocity: $18,000 \leq u_\infty \leq 25,000$ ft/sec (this range covers the normal corridor of reentry velocities)

wall temperature: $1,000 \leq T_w \leq 5,000^\circ R$

angle of attack: $0^\circ \leq \alpha \leq \theta$

wall material: ablating or outgassing

The degree of accuracy of the transition altitudes presented is expected to be within 15,000 feet of altitude.

Non-ablating vehicles with a smooth surface finish (i.e., beryllium) are expected to undergo transition 15,000 to 20,000 feet below the transition altitude for the corresponding ablating vehicle.

The generalized study was performed for a velocity of 25,000 ft/sec using the methods described in the previous section. The results obtained for specific cases of body length and nose radius were replotted as a function of bluntness ratio. These plots were then cross-plotted at bluntness ratios of 0, 0.1, 0.2, and 0.3; the final results are shown in figures 37 to 40.

These results show the altitudes where transition is initially expected to occur on the body. For all the configurations investigated, the initial station to undergo transition was always at the rear of the body ($x = L$); then as the altitude decreases, the transition location proceeds upstream. In

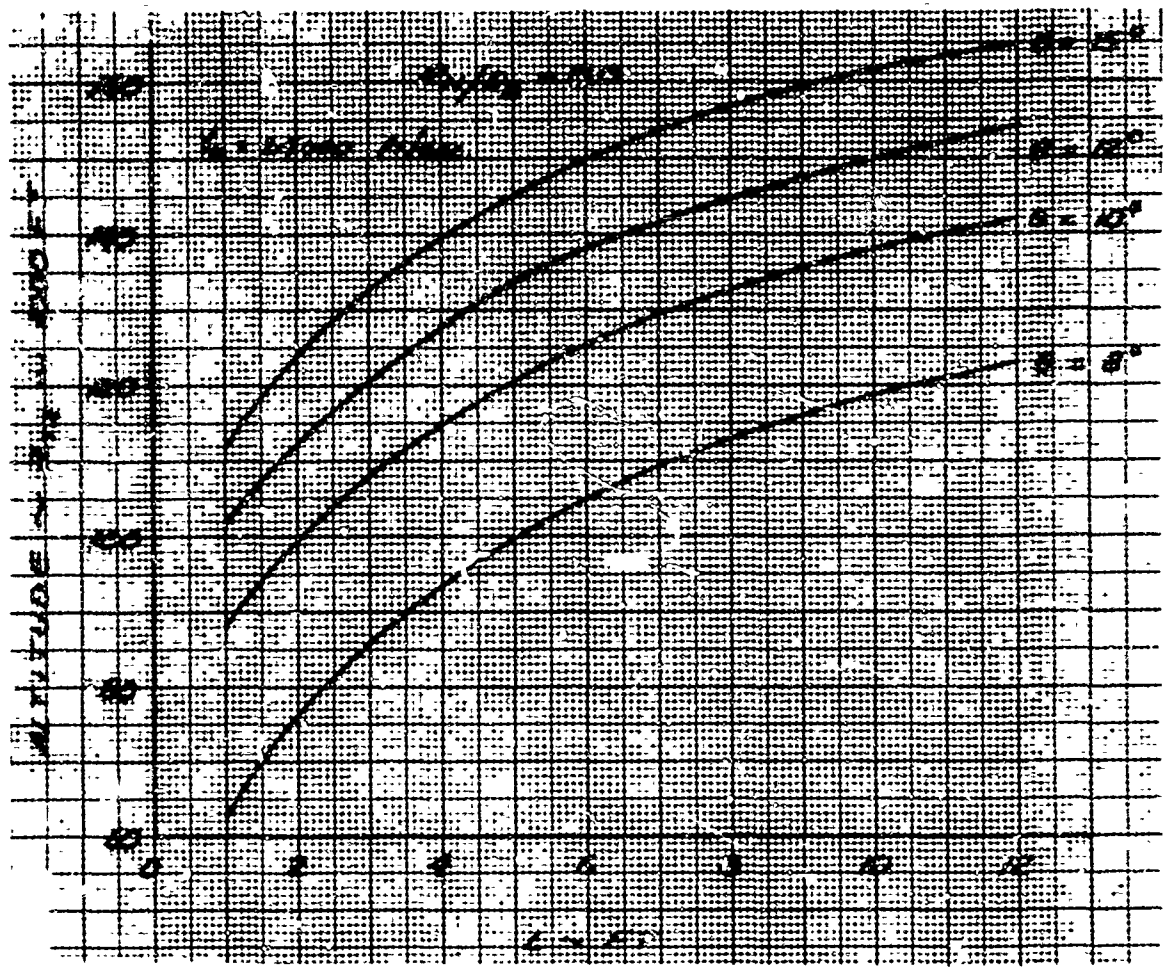


Figure 37 ALTITUDE OF INITIAL TRANSITION FOR VARYING CONE ANGLES

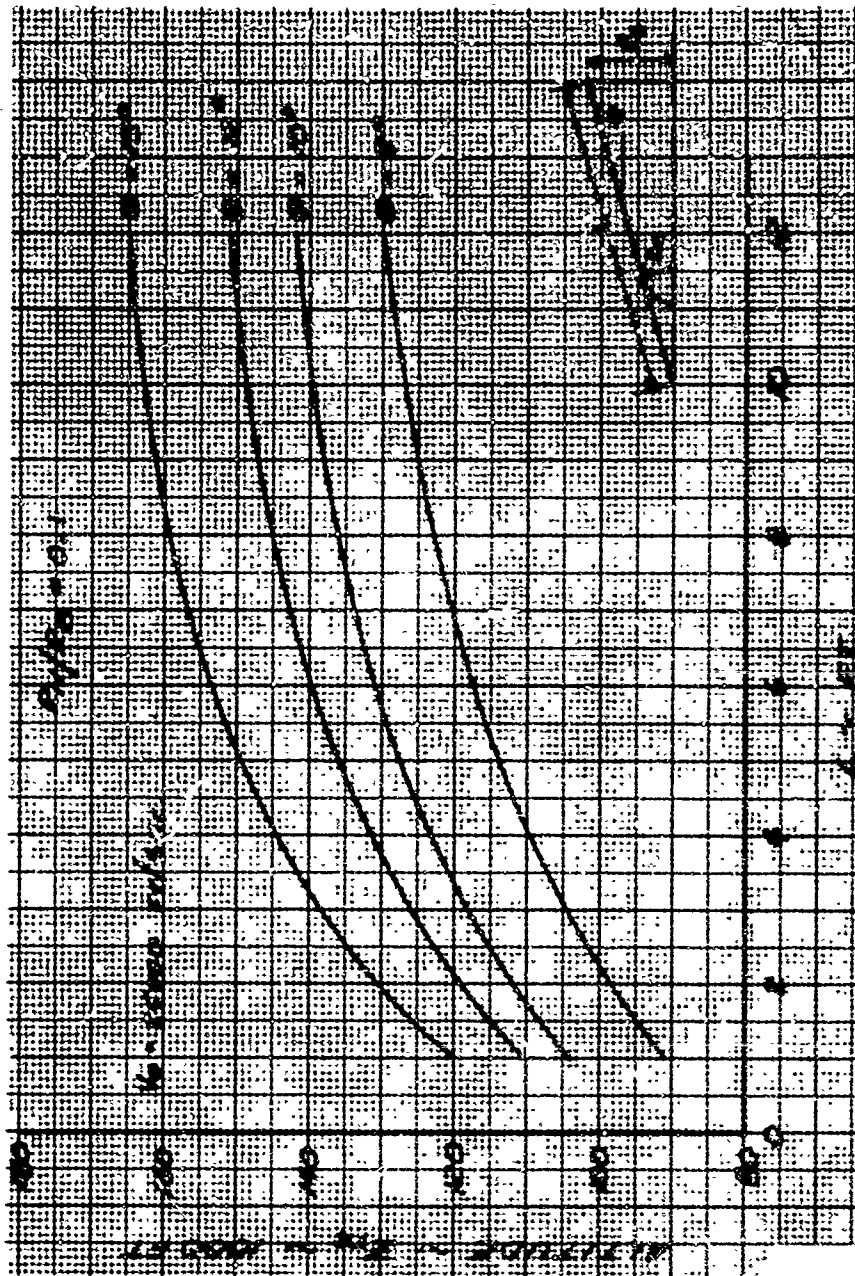


Figure 38 ALTITUDE OF INITIAL TRANSITION FOR VARYING CONE ANGLES

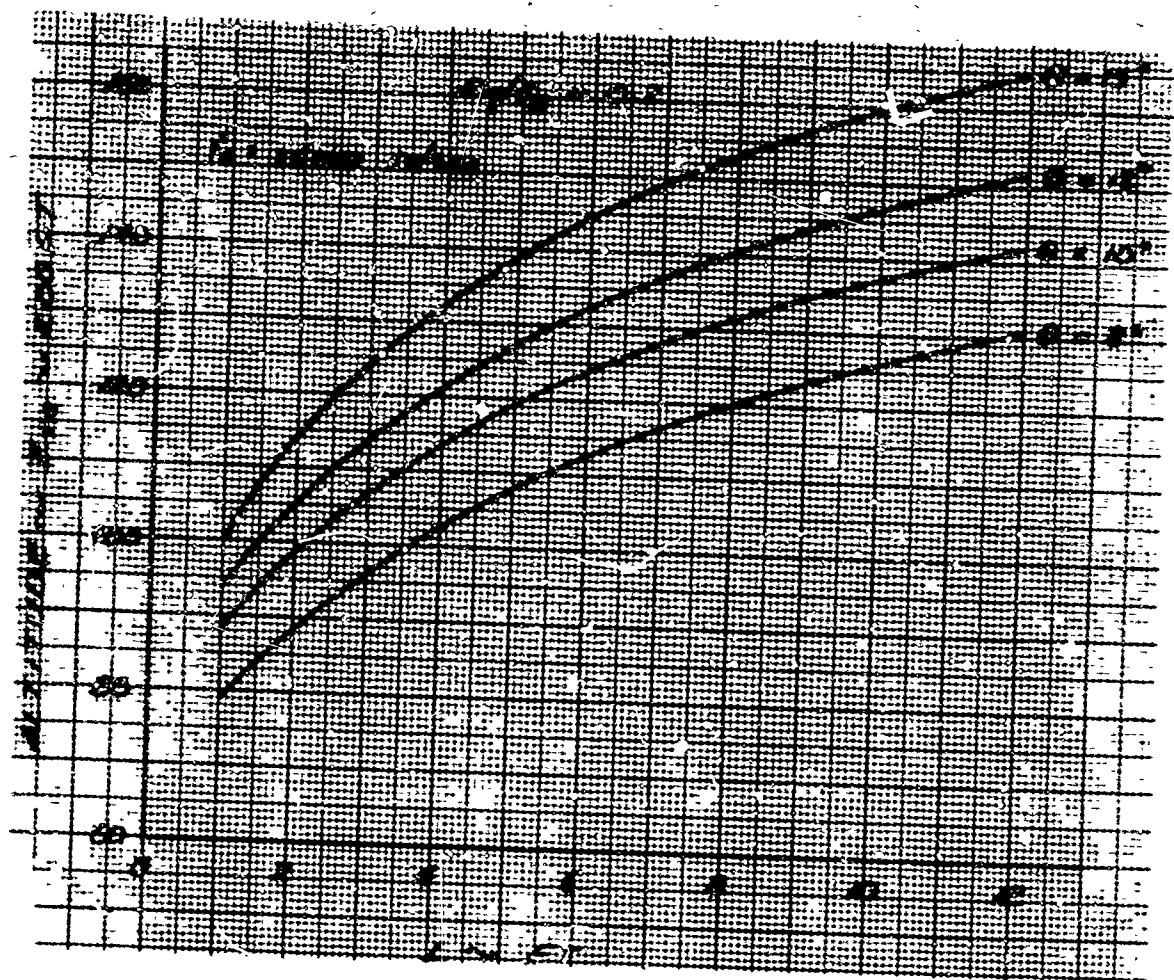


Figure 39 ALTITUDE OF INITIAL TRANSITION FOR VARYING CONE ANGLES

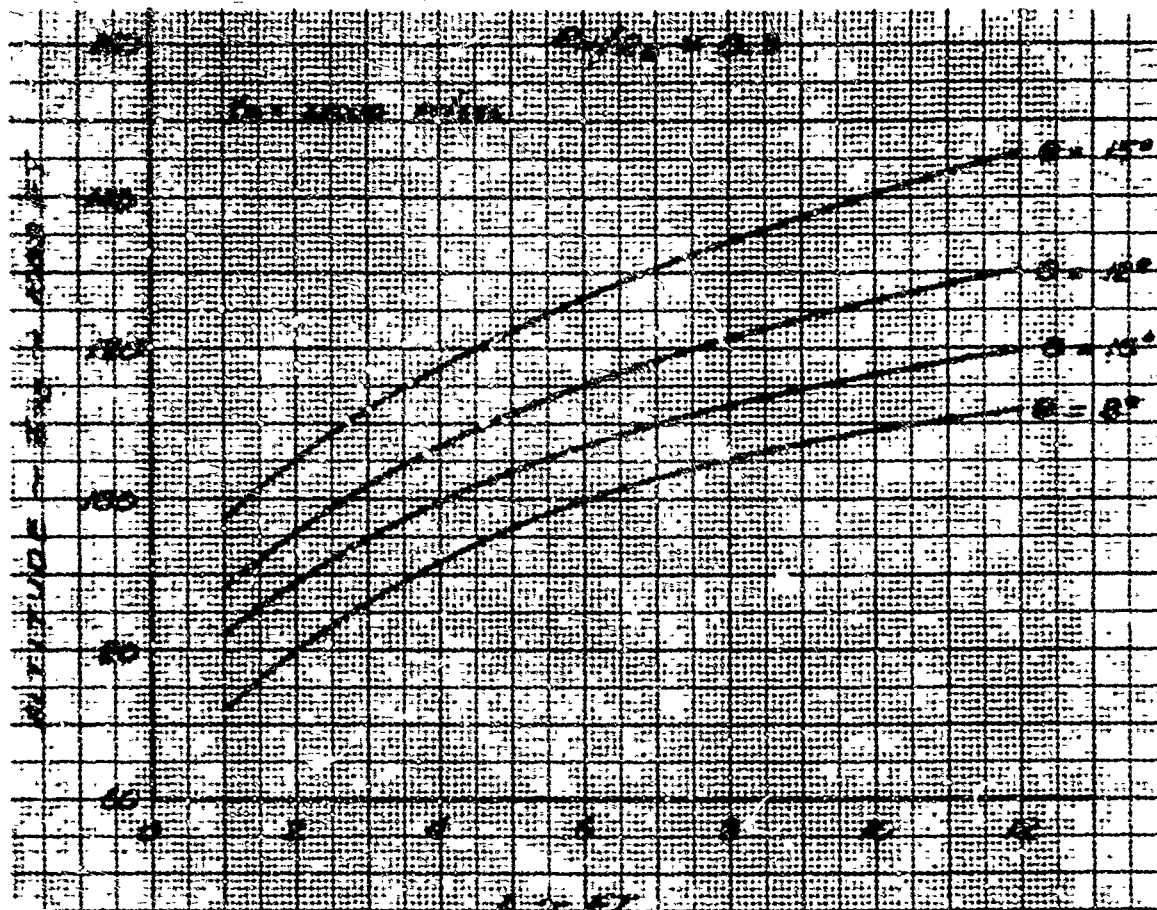


Figure 40 ALTITUDE OF INITIAL TRANSITION FOR VARYING CONE ANGLES

the case of low bluntness cones with $\theta < 8^\circ$, the $Re_x - M_\infty$ distribution may show that transition will occur first in the forward region of the cone, thus triggering transition over the major portion of the body.

For the cases shown in figures 37 to 40, where transition occurs first in the rear portion, there are two types of information that can be obtained from the graphs: 1) the altitude of initial transition may be obtained as a function of θ , R_N/R_B , and L , and 2) for a particular vehicle in which these three parameters are known, the altitude range of transition may be determined; i. e., for an 8-degree cone, 12 feet long and a 0.10 bluntness ratio at a velocity of 25,000 ft/sec, figure 38 shows that transition will commence at 130,000 feet and the one foot station will become turbulent at 90,000 feet.

To account for the effects of free-stream velocity in the range of $18,000 \leq u_\infty \leq 25,000$ ft/sec, the results shown in figures 37 to 40 may be used in conjunction with a velocity correction factor; i. e.,

$$Z_{TR} = (Z_{TR})_{u_\infty = 25000} + \Delta Z$$

The quantity ΔZ represents the increase in transition altitude as the velocity is decreased below 25,000 ft/sec. This increase in altitude is most significant in the case of sharp and slightly blunted cones having high values of M_∞ at $x = L$. The reason is as follows: as the velocity is decreased, M_∞ and Re_x are both decreased. However, according to figure 33, the reduction in M_∞ causes $(Re_x)_{TR}$ to decrease at a faster rate than Re_x . Therefore, transition occurs earlier when the velocity is decreased.

In the case of highly blunted cones, M_∞ is relatively low ($2 < M_\infty < 4$) and as shown in figure 33 $(Re_x)_{TR}$ is not very sensitive to M_∞ in this range. Therefore, with blunted cones the transition altitude is not very sensitive to free stream velocity.

A parametric evaluation of this velocity effect is shown in figure 41. These results represent the approximate increase in transition altitude as a function of velocity and bluntness ratio for an average cone angle and body length.

The results shown in figures 37 to 41 represents a first attempt to correlate transition altitude as a function of the influencing parameters. The main weakness of this method is that it fails to include all the factors which tend to destabilize the boundary layer. The argument presented here is that the local Mach-number influence on the transition Reynolds number is the dominating effect, while the net effect of all the other parameters is relatively small. This argument stems from the analysis of flight test data provided in reference 43.

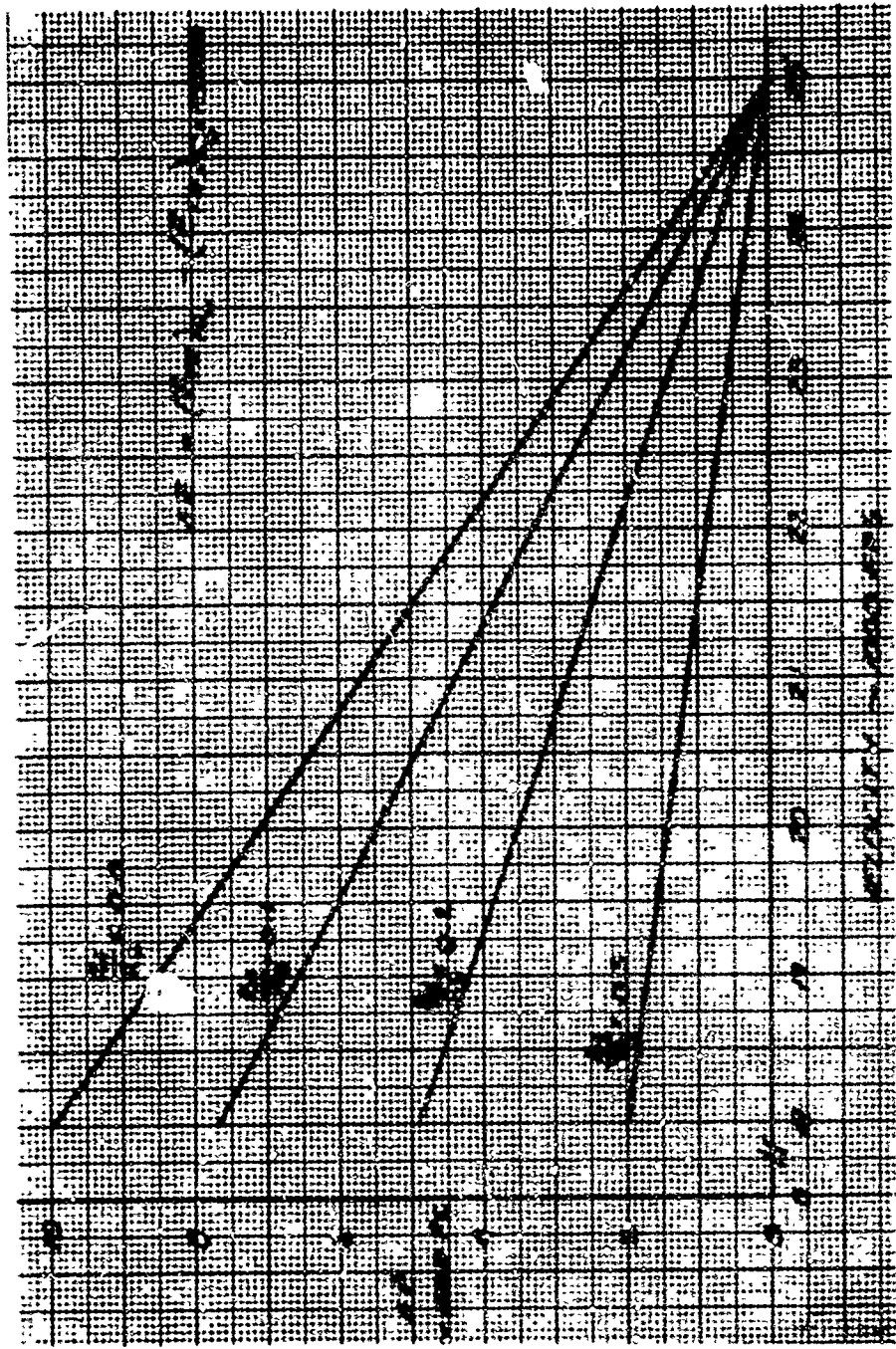


Figure 41 VELOCITY EFFECT ON TRANSITION ALTITUDE

To check the accuracy of the correlation curves presented, they have been used to re-estimate the transition altitudes for the various flight tests in which reliable transition data was available. In all cases, agreement was achieved within 10,000 feet of altitude. In predicting the transition altitudes for future vehicles, it is expected that these results will be valid within 15,000 feet if the flight conditions are within the specified range of variables.

As more test data becomes available, the present transition criterion will be improved to include more of the influencing parameters. The new criterion can then be used in conjunction with the $(Re_x - M_\infty)$ maps shown in this report and in reference 47 in order to develop new graphs for predicting the transition altitudes.

VII. SPHERE DRAG AND TRANSITION

A. Drag Coefficient

The drag coefficient of a sphere, like that of a cone, is the sum of the contributions of pressure drag, base drag, skin friction drag, and induced drag. For spheres, however, the pressure and skin friction drag are the dominant factors. The induced drag for spheres is negligible for all cases of practical interest. Base drag, although not negligible, is a small percentage of the total drag at Mach numbers between 5 and 25.

The pressure drag is usually considered to be a function of Mach number only, while the skin friction drag is a function of Reynolds number. Therefore, the sphere drag coefficient prediction would be expected to have the form $C_D = f(M) + g(R_{xL})$. Data which confirm this expression from references 48 through 54 are presented. No data on wall temperature effects were found.

A plot of drag coefficient versus Mach number is shown in figure 42. These data correspond to flight below 150,000 feet, based on the sphere size and flight conditions called for in this study. The predicted constant value of $C_D = 0.92$ fits the data well within a ± 10 percent band for $M > 3$. It is assumed that C_D remains constant through $M=25$ although the highest Mach number tested was approximately 16. Test results from other blunt bodies substantiate this assumption.

Drag coefficient versus Reynolds number is plotted in figure 43. Values in the region $10^4 \leq Re \leq 10^5$ represent Mach numbers as low as 2.5. Here, too, the constant value of $C_D = 0.92$ fits the test data within a ± 10 percent band for a simulated flight altitude of almost 200,000 feet, described by a 3.75-inch diameter sphere at Mach 5. At $R_{xL} 5 \times 10^4$ or an altitude greater than 150,000 feet, C_D increases with decreasing Re . A curve fit of this trend yields

$$C_D = 0.92 + \frac{500}{R_{xL}}$$

This equation is applicable throughout the range of interest.

B. Boundary Layer Transition

For spherical configurations, a limited parametric study has been made to correlate transition altitude as a function of sphere radius, R_s , and free-stream velocity.

For this investigation, a constant value of transition Reynolds number $(Re_x)_{TR} = 300,000$ was assumed. To determine the local Reynolds number distribution along the sphere, the fluid properties were computed using a Newtonian pressure distribution and the entropy behind a normal shock. The maximum unit

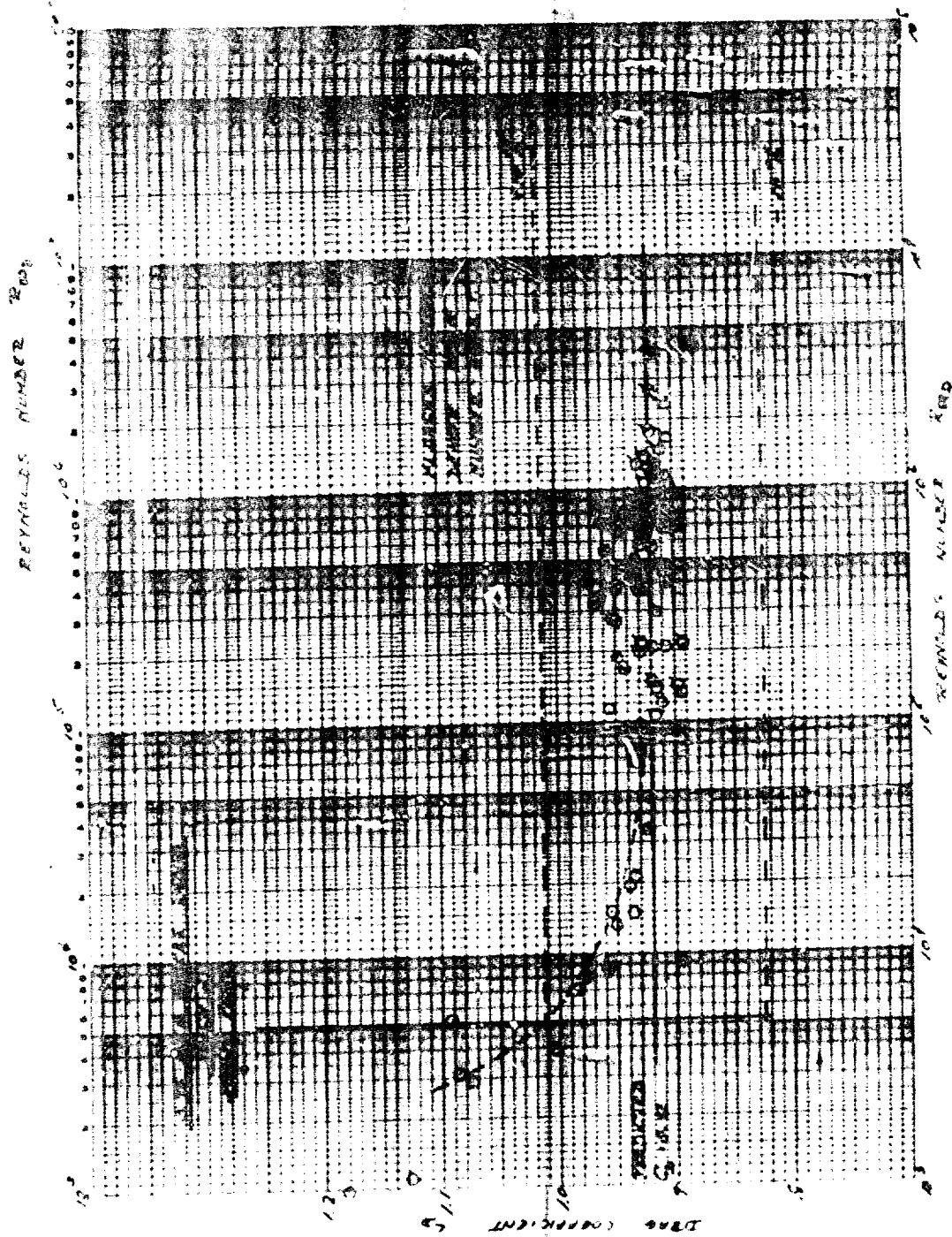


Figure 43 SPHERE DRAG COEFFICIENT AS A FUNCTION OF REYNOLDS NUMBER

Best Available Copy

Reynolds number occurs at the sonic point where the mass flow is maximum. Employing the computed unit Reynolds number distribution in conjunction with the surface distance from the stagnation point and the assumed value of $(Re_x)_{TR}$, the transition altitudes have been determined. The results are presented in figure 44 for velocities of 5,000, 15,000, and 25,000 ft/sec. These graphs show that the greater the velocity, the higher the transition altitude. This occurs because the local Reynolds number increases with velocity while the local Mach number is essentially constant.

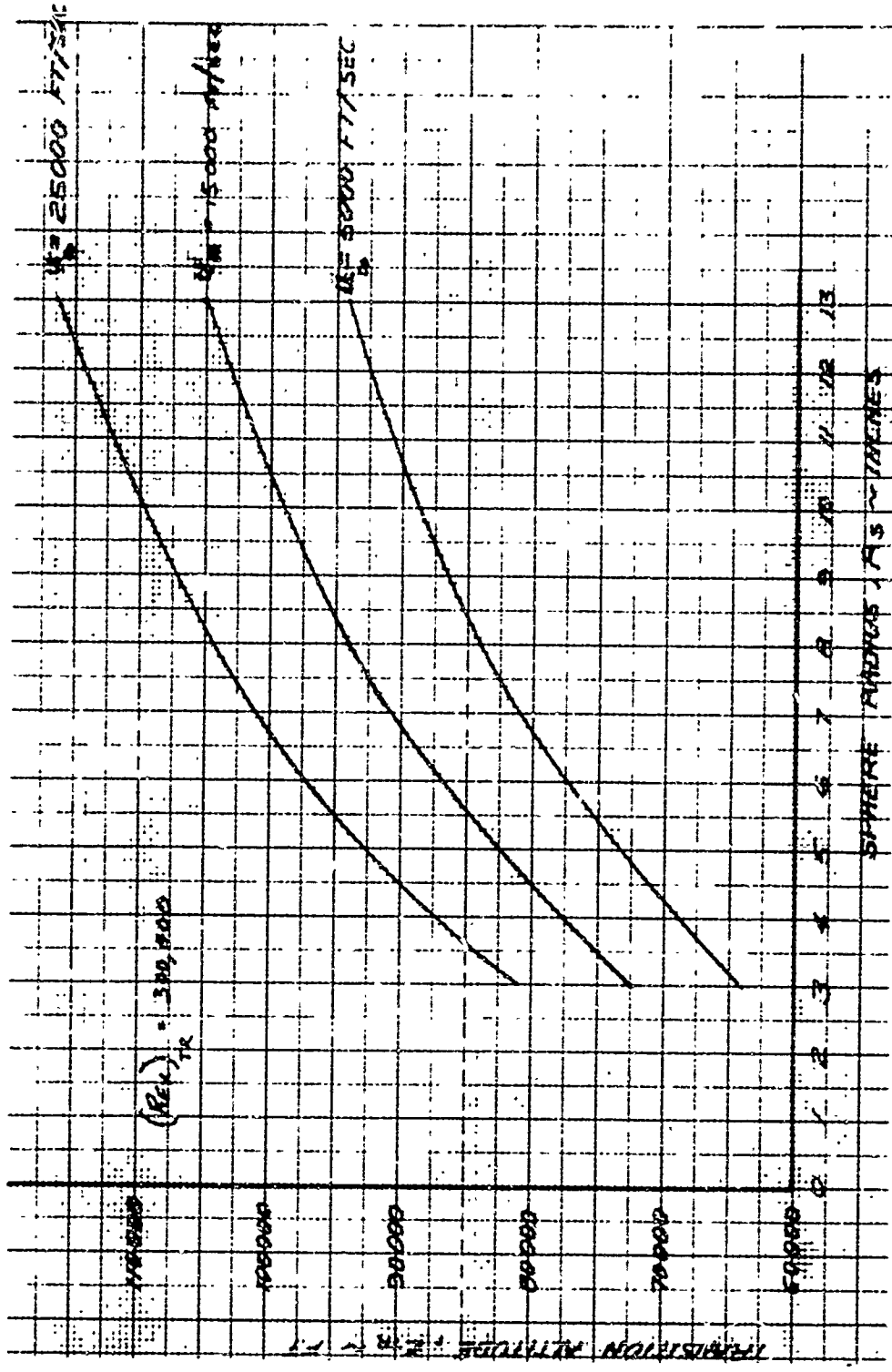


Figure 44 ALTITUDE OF INITIAL TRANSITION FOR SPHERES

VIII CONCLUSIONS

The analytical expressions presented in this report satisfy the basic requirements of the study:

- 1) All equations are in terms of free stream properties, body geometry, and surface material.
- 2) The accuracy requirements have been met based on comparison with extensive wind-tunnel and ballistic range data, and one set of flight test data.
- 3) The specified ranges of variables have been covered.

The additional requirement that has been satisfied is the determination of the transition altitude range as a function of the several influencing parameters

The equations that are presented in this report for cones have been programmed for digital computer solution (Program 1954) (Reference 55). The results of this program have been compared to more rigorous solutions and there has been excellent agreement. The program is, however, limited to the ranges of variables covered in this report.

In order to improve and expand the drag solutions presented herein, it is suggested that the following additional tasks be performed:

- 1) Employ more rigorous solutions in order to determine the effects of blowing on skin friction drag and induced drag.
- 2) Extend the Mach number and cone angle range to include the transonic region and cone angles as shallow as 4° .
- 3) Develop drag equations for the triconic shape as the general configuration, noting that cones, bi-conics, and cone-cylinder-flares are special cases of the triconic.

These three tasks can be performed employing existing capabilities. The additional tasks that require highly advanced state-of-the-art techniques would be involved with the determination of all the drag components at angles of attack greater than the cone half-angle. The approximations employed in this investigation for viscous effects at $\alpha \neq 0$ should be valid only at small angles of attack.

IX. REFERENCES

1. Kopal, Z., Tables of Supersonic Flow Around Cones, MIT Center of Analysis, TR No. 1 (1947).
2. Springfield, J., and J. L'Hommedieu, Machine Computation of Conical Flow Fields and Oblique Shocks, Avco RAD-TR-510-63-6.
3. Wood, A., Machine Programming of Method of Characteristics RAD-TR-58-47 (November 1958).
4. Springfield, J., Steady, Inviscid Flow of a Relaxing Gas About a Blunt Body with Supersonic Velocity, Proceedings of the 1964 Heat Transfer and Fluid Mechanics Institute.
5. Chushkin, P. I. and N. P. Shushlina, Tables of Supersonic Flow About Blunted Cones (Translated and Edited by J. F. Springfield) RAD-TM-62-63 (14 September 1962).
6. Belotserkovskii, O., Symmetric Flow of Perfect and Real Gases Past Blunted Bodies, Vychislitel'noi Mat. i Mat. Fiziki, 2, No. 6 (November 1962).
7. Pannabecker, C., Inviscid Pressure Drag Coefficients for Sharp and Blunt Cones, RAD-S210-TR-65-71 (June 1965).
8. Waldman, Katz, L'Hommedieu, and Moskowitz, Real-Gas Yawed Cone Flow, Avco RAD-TR-510-3-4.
9. Waldman, G., Integral Approach to the Yawed Blunt Body Flow Problem, AIAA Technical Paper (January 1965).
10. Waldman, G., Newtonian Program for Bodies of Revolution, RAD-TM-60-36.
11. Esterman, D., Digital Computer Program 1413A for General Least Squared Data Fit of a Dependent Variable as a Function of up to Three Independent Variables, Avco RAD-TRK-322 64 16 (April 1964).
12. Julius, J. D., Measurements of Pressure and Local Heat Transfer on a 20° Cone at Angles of Attack up to 20 degrees for Mach Number of 4.95 NASA TND-79 December 1959 (U).
13. Amic, J. L., Pressure Measurements on Sharp and Blunt 5 and 15 degree Half Angle Cones at Mach Number 3.86 and Angles of Attack to 100 degrees. NASA TND-753, February 1961.

14. Shaperio Asher, The Dynamics and Thermodynamics of Compressible Fluid Flow, the Ronald Press (1954).
15. Quint, P. B., Unpublished Data, Dept. G-370 (November 1963).
16. Whitfield, J. D., and J. C. Potter, On Base Pressures at High Reynolds Numbers and Hypersonic Mach Numbers AEDC TN-60-61 (March 1960).
17. [REDACTED]
18. Mangler, W., Compressible Boundary Layers on Bodies of Revolution, ATI No. 28063, MAP-VG 83-4 (June 1946).
19. Eckert, E., Engineering Relations for Heat Transfer and Friction in High Velocity Laminar and Turbulent Boundary Layer Flow Over Surfaces with Constant Pressure and Temperature, ASME Paper No. 55-A-31.
20. Munson, T., Wall Temperature Effects on Cold Wall Heating, Avco RAD-TR-63-326.
21. Romig, M., Conical Flow Parameters for Air in Dissociated Equilibrium Convair Report 7 (May 1960).
22. Linnell and Bailey, Similarity Rule Estimation Methods for Cones and Parabolic Noses, J.A.S., (August 1956).
23. Rose, P., R. Probstein and M. Adams, Turbulent Heat Transfer Through a Highly Cooled Partially Dissociated Boundary Layer, Avco Everett Report No. 14 (1958).
24. Schurmann, E.E.H., Engineering Methods for the Analysis of Aerodynamic Heating, RAD-TM-63-68 (November 1963).
25. Grabow, R., Calculation of Bluntness Effects on Conical Configurations RAD-TR-63-57 (November 1963).
26. Tracy, R., Hypersonic Flow Over a Yawed Circular Cone, Cal Tech. Aero Labs, August 1963.
27. Klugerman, J. and C. Shipman, A Numerical Method of Solving the Thermochemical Equilibrium Problem RAD-TM-62-11 (April 1962).
28. Yos, J., Transport Properties of Nitrogen, Hydrogen, Oxygen and Air to 30,000 Degrees Kelvin RAD-TM-63-7.

29. Thyson, N., Program 1475, Similar Solutions of the Laminar Boundary Layer Equations RAD-TR-64-12.
30. Lavin, M., Mass Injection Into a Turbulent Boundary Layer, Avco RAD-TM-64-28.
31. Van Tassell, W., Estimation of Reduction in Skin-Friction Due to Transpiration, Avco RAD-TR-61-163.
32. Probst, R., Interacting Hypersonic Boundary Layer Flow Over a Cone, TR 2798/1, Brown University (March 1955).
33. Whitfield, J., and B. Griffith, Hypersonic Viscous Drag Effects on Blunt Slender Cones, AIAA Pre-print 63-434.
34. Thyson, N., Blowing Effects on Pressure Interaction Associated With Cones, RAD-TR-63-81.
35. Schurmann, E. E. H., Effective Displacement Thickness on an Ablating Surface, RAD-TR-63-5.
36. Lyons, W. C., J. J. Brady, and Z. J. Levensteins, Hypersonic Drag, Stability and Wake Data for Cones and Spheres, AIAA Journal, 2, No. 11, (1948).
37. Wolnz, W., Blunt Cone Force Tests at $M = 20$, AEDC TDR-62-43.
38. Sheetz, N. W. Jr., Free-Flight Boundary Layer Transition Investigations at Hypersonic Speeds, AIAA Paper No. 65-127 (January 1965).
39. Chadwick, G. A. and J. A. Greco, Static Force, Pressure, and Heat Transfer Data of LORV Configurations, 6.5LM 17.2, Avco RAD-SR-63-109. Secret
40. Whitfield, J. D. and B. J. Griffith, Viscous Effects on Zero - Lift Drag of Slender Blunt Cones, AEDC-TDR-63-35.
41. Wilkinson, D. B. and S. A. Harrington, Hypersonic Force, Pressure, and Heat Transfer Investigations of Sharp and Blunt Slender Cones, AEDC - TDR-63-177.
42. "Deleted for Security Reasons"
43. Grabow, R., Boundary Layer Transition Data from Various Flight Tests RAD-TR (to be published).

44. Scott, C., and G. Anderson, Boundary Layer Transition with Gas Injection
ASTIA Doc. AD 262112 (July 1958).
45. Van Driest, E., and J. Boison, Experiments on Boundary Layers at
Supersonic Speeds, JAS, 24, (1957).
46. Low, G., Boundary Layer Transition at Supersonic Speeds, NACA RM
E56E10 (August 1956).
47. Grabow, R., and D. Wells, An Estimation of Boundary Layer Transition
Altitudes for Families of Cones and Spheres, RAD-TR-65-70.
48. May, A. and W. R. Witt, Jr., Free-Flight Determinations of the Drag
Coefficients of Spheres, Journal of the Aeronautical Sciences (September
1953).
49. May, A., Supersonic Drag of Spheres at Low Reynolds Numbers in Free
Flight, NAVORD Report 4392, U. S. Naval Ordnance Laboratory
(11 December 1956).
50. Charters, A. C. and R. N. Thomas, The Aerodynamic Performance of
Small Spheres from Subsonic to High Supersonic Velocities, Journal of
the Aeronautical Sciences (October 1945).
51. Hodges, A. J., The Drag Coefficient of Very High Velocity Spheres,
Journal of the Aeronautical Sciences (October 1957).
52. Clark, A. B. J. and F. T. Harris, Free-Flight Air-Drag Measurement
Techniques. Journal of the Aeronautical Sciences (June 1952).
53. Research Summary No. 36-12, Volume I, Jet Propulsion Laboratory,
2 January 1952.
54. Brady, J., Unpublished Data, Naval Ordnance Laboratory (March 1965).
55. Grabow, R. and Wells, D., "Programming of Cone Drag Equations,"
RAD TR- (To be published)

BIBLIOGRAPHY

[REDACTED]

[REDACTED]

[REDACTED]

Experimental Investigation of the Aerodynamic Characteristics of 9 Degree Half-Angle Cones with Varying Degrees of Bluntness at Mach Number 9,² Aeronutronic Publication No. U-1638. Unclassified

[REDACTED]

[REDACTED]

[REDACTED]

[REDACTED]

[REDACTED]

[REDACTED]

[REDACTED]

Fuller, D. E. and C. D. Babb, Static Stability Investigation of Proposed Project Fire Space Vehicle and Reentry Package Configurations,³ NASA TND-1497. Unclassified.

Schippell, H. R., Trailblazer I Reentry Body Wind Tunnel Tests with Theoretical Aerodynamics and Limited Dynamic Analysis,³ NASA TND-1936. Unclassified.

Penland, J. A., A Study of the Stability and Location of the Center of Pressure on Sharp Right Circular Cones at Hypersonic Speeds,² NASA TND-2783. Unclassified

Amick, J. L., Pressure Measurements on Sharp and Blunt 5° and 15° Half-Angle Cones at Mach Number 3.86 and Angles of Attack to 100°,² NASA TND-753. Unclassified

Penland, J. A., Aerodynamic Force Characteristics of a Series of Lifting Cone and Cone-Cylinder Configurations at a Mach Number of 6.83 and Angles of Attack up to 130°,² NASA TND-846. Unclassified

Wehrend, Jr., W. R., Wind-Tunnel Investigation of the Static and Dynamic Stability Characteristics of a 10° Semi Vertex Angle Blunted Cone,⁴ NASA TN D-1202. Unclassified

Intrieri, P. F., Free-Flight Measurement of the Static and Dynamic Stability and Drag of a 10° Blunted Cone at Mach 3.5 and 8.5, NACA D-1299. Unclassified.

Treon, S. L., Static Aerodynamic Characteristics of Short Blunt Cones with Nose and Base Cone Angles at Mach 0.6 to 5.5 and Angles of Attack to 180°.¹ NASA TN D-1327. Unclassified

Ladson, C. L. and T. A. Blackstock, Air-Helium Simulation of the Aero Force Coefficient of Cones at Hypersonic Speeds,² NASA TN D-1473. Unclassified

Harrison, E. F., Static Stability Tests in the Langley 24-inch Hypersonic Arc Tunnel of a Blunted Cone at a Mach Number of 20,¹ NASA TN D-1508. Unclassified

Neal, Jr., L., Aerodynamic Characteristics at a Mach Number of 6.77 of a 9° Cone Configuration with and without Spherical Afterbodies at Angles of Attack up to 180° with Various Degrees of Nose Blunting,² NASA TN D-1606. Unclassified

Shaw, D. S., D. E. Onlier, and C. D. Bebb. Effects of Nose Bluntness, L/D, Cone Angle, and Model Based on Static Aerodynamic Characteristics of Blunt Bodies,¹ NASA TND-1781. Unclassified

Brooks, Jr., C. W., and C. D. Trescot Jr., Transonic Investigation of the Effects of Nose Bluntness Fineness Ratio, Cone Angle, and Base Shape on the Static Aerodynamic Characteristics of Short, Blunt Nosed Cones at Angles of Attack to 180°,¹ NASA TND-1926.

7

Keyes, J. W., Longitudinal Aerodynamic Characteristics of Blunted Cones at Mach 3.5, 4.2, and 6.0,⁴ NASA TND-2201. Unclassified

Spencer Jr., B., W. P. Phillips, A. H. Fournier, Supersonic Aerodynamic Characteristics of Bodies Having Variations in Fineness Ratio and Cross-Section Ellipticity,³ NASA TN D-2389. Unclassified



Coltrane, L. C., Stability Investigation of a Blunt Cone and a Blunt Ogive with Flared Cylinder Afterbody,¹ NASA TMX-199. Unclassified



Perkins, E. W., and L. H. Jorgenson, Investigation of Drag of Various Axially Symmetric Nose Shapes $L/D = 3$,¹ NACA RMA52 H28. Unclassified

Neice, S. E., and T. J. Wong, An Experimental Investigation of the Applicability of the Hypersonic Similarity Law to Bodies of Revolution,² NACA RMA52 K07. Unclassified

Dennis, D. H. and B. E. Cunningham, Forces and Moments on Inclined Bodies of Revolution at Mach Numbers from 3.0 to 6.3,¹ NASA RMA54E03. Unclassified.

Canning, T. N., Investigation of Lift, Center of Pressure, and Drag of a Projectile,¹ NACA RMA54H23a. Unclassified

Cohen, A. J., Aerodynamic Characteristics of Four Bodies of Revolutions Showing Some Effect of Afterbody Shape and L/D ,³ NACA RME51C06. Unclassified

Thompson, J. R., Measurement of the Drag and Pressure Distribution on a Body of Revolution throughout Transfer from Sub to Supersonic Speeds,³ NACA RML9J27. Unclassified

Ulmann, E. F., and R. W. Dunning, Normal Force, Center of Pressure, and Zero Lift Drag of Several Ballistic-Type Missiles at Mach Number 4.05,³ NACA RML54D30a. Unclassified

Coltrane, L. C., Stability Investigation of a Blunt Cone and a Blunt Cylinder with a Square Base and Mach 0.64 to 2.14,⁴ NACA RML58G24. Unclassified

[REDACTED]

[REDACTED]

[REDACTED]

Hermann, R., K. O. Thomson, and W. L. Melnick, Aerodynamic and Heat Transfer Characteristics of Basic Bodies in Hypersonic Flow of Air and of Combustion Gas Mixtures,⁴ AEDC TDR-62-89 AD 274 792. Unclassified

[REDACTED]

Whitfield, J., and W. Wolny, Hypersonic Static Stability of Blunt Slender Cones,⁴ AEDC TDR-62-166. Unclassified

[REDACTED]

Sylverter, M. A., Wind Tunnel Tests of the Redstone "B" Nose Cone at Mach Numbers from 1.75 to 5.0,³ Aberdeen Proving Grounds BRL 1522. Unclassified

[REDACTED]

Potter, J. L., New Experimental Investigation of Friction Drag and Boundary Layer Transition on Bodies of Revolution at Supersonic Speeds,³ Naval Ordnance Laboratory NOVORD REP 2371. Unclassified

[REDACTED]

Whitfield, J. D., and W. Wolney, Correlation of Hypersonic Static Stability Data from Blunt Slender Cones,⁴ AIAA Journal, Vol. 1, No. 2, p. 486. Unclassified

[REDACTED]